High Resolution X-ray Imaging and Quantitative Microanalysis in Electron Microscopy

Chaoyi Teng

Department of Mining and Materials Engineering,
McGill University, Montreal

A thesis submitted to McGill University in partial fulfilment of the requirements of the degree of Doctor of Philosophy

Acknowledgements

I would like to express my sincere appreciation to my supervisor, Prof. Raynald Gauvin, for his patience, motivation and immense knowledge throughout this research, without which this thesis would not have been possible.

My sincere thanks go to Dr. Hendrix Demers from Hydro-Québec, for his valuable discussion and evaluation of my research. I am grateful to Mr. Nicolas Brodusch for this technical assistance. I would like to thank Mr. Frédéric Voisard for assistance in writing the French abstract.

I am deeply grateful to all my colleagues in McGill Electron Microscopy Research Group. I would like to thank all the professors, staffs and students in Mining and Materials Engineering Department.

I would like to thank the financial support from Natural Science and Engineering Research Council (NSERC) and McGill Engineering Doctoral Award (MEDA).

Finally, I would like to express the deepest gratitude to my parents, Mr. Qingliang Teng and Mrs. Xiaohui Li, for their unconditional love and unfailing support. I would also like to thank Mr. Xin Chu, for his warm company.

Abstract

Scanning electron microscope/energy dispersive spectroscopy (SEM/EDS) systems are popular for X-ray microanalysis due to its simple and fast operation. Recent years, which use cold field emission sources and silicon drift detectors, are highly capable X-ray imaging and quantitative microanalysis tools. However, the analytical efficiency and accuracy of SEM/EDS still have room for improvement. Regarding X-ray elemental mapping in particular, the top concern is to collect sufficient X-ray counts. Unfortunately, high count rates are usually achieved with sacrificing acquisition efficiency or spatial resolution. Regarding the quantitative X-ray microanalysis, the accuracy of EDS is constantly being questioned. Thus, the objective of this study is to optimize the SEM/EDS, making it a more efficient and accurate analytical instrument.

In this study, X-ray mapping was performed on rare earth minerals (REMs), which contain various phases and complicated elemental constituents. The data was collected using a cold field emission SEM (CFE-SEM) equipped with an annular SDD (aSDD). The traditional elemental maps usually have excessive noise and limited phase information, so phase map analysis was performed instead. Compared with the conventional SDD, the aSDD has a larger solid angle, which produces high count rate and allows for efficient analysis at a low beam energy. The enhanced spatial resolution enables the accurate identification of REM phases down to one micron. In addition, the multivariate statistical analysis (MSA), i.e. the principal components analysis (PCA) and the blind source separation (BSS), was performed on the phase maps of REMs. This

analysis reduces the noise and improves the phase identification accuracy, shortening the necessary acquisition time

The *f*-ratio method, which is a recently developed quantitative analysis method for binary systems based on a CFE-SEM/EDS, is used. This method incorporates traditional EDS experiments and Monte Carlo simulations. Standards with known compositions are needed to calibrate the differences between experiments and simulations. In this study, the *f*-ratio method was applied to multi-element systems, including two Mg-Al-Zn alloys, and three standard minerals [kyanite (Al_2SiO_5), albite ($NaAlSi_3O_8$) and orthoclase ($KAlSi_3O_8$)]. The requirement of standard option was extended to any standard containing one or more target elements. The influences of the beam current, beam energy, and the standard composition were investigated. It is shown that the beam current does not have obvious impacts on the quantification results, so the *f*-ratio method is suitable for long acquisition, even when suffering from current instabilities. In addition, using beam-energy-dependent calibration factors, the *f*-ratio method can achieve a satisfactory accuracy.

Résumé

Les systèmes de microscopie électronique à balayage couplé à la spectroscopie à dispersion d'énergie (MEB/EDS) sont couramment utilisés pour la microanalyse par rayons X en raison de leur fonctionnement simple et rapide. Les systèmes récents, qui utilisent des sources d'émission de champ à froid et des détecteurs à dérive au silicium (SDD), sont des outils d'imagerie par rayons X et de microanalyses quantitatives extrêmement performantes. Cependant, l'efficacité analytique et la précision du MEB/EDS peuvent encore être améliorées. Lors d'une acquisition d'une cartographie d'éléments par rayons X, la principale préoccupation est de récolter un nombre suffisant de rayons X. Malheureusement, des comptes élevés sont généralement obtenus en sacrifiant l'efficacité de l'acquisition ou la résolution spatiale. En ce qui concerne la microanalyse quantitative par rayons X, la précision de l'EDS est souvent remise en question. Ainsi, l'objectif de cette étude est d'optimiser le MEB/EDS afin d'en faire un instrument d'analyse plus efficace et précis.

Au cours de cette étude, des cartes de rayons X ont été réalisées sur des minéraux de terres rares (REM), qui contiennent divers constituants élémentaires ainsi que des phases complexes. Les données ont été recueillies à l'aide d'un MEB à émission de champ à froid (CFE-MEB) équipé d'un SDD annulaire (aSDD). Les cartes élémentaires traditionnelles montrent généralement un bruit excessif et des informations de phase limitées. Par conséquent, l'analyse d'une carte de phase a été réalisée à la place d'une carte élémentaire traditionnelle. Comparé au SDD conventionnel, l'aSDD possède une zone de couverture angulaire plus large (grand angle solide) ce qui produit

des taux de comptage élevés. Ceci permet donc une analyse efficace à une énergie de faisceau réduite. La résolution spatiale améliorée permet l'identification précise des phases REM jusqu'à un micron. En outre, l'analyse statistique multivariée (MSA), c'est-à-dire l'analyse en composantes principales (PCA) et la séparation aveugle des sources (BSS), a été réalisée sur les cartes de phase des REM. Cette analyse réduit le bruit et améliore la précision de l'identification de la phase, réduisant ainsi le temps d'acquisition nécessaire.

La méthode du *f*-ratio est une méthode d'analyse quantitative récemment mise au point pour les systèmes CFE-MEB/EDS. Jusqu'à présent, cette méthode n'a été utilisée que pour les systèmes élémentaires binaires. Le *f*-ratio intègre les expériences traditionnelles EDS et les simulations Monte Carlo. Des standards avec des compositions connues sont nécessaires pour calibrer les différences entre les expériences et les simulations. Dans cette étude, la méthode du *f*-ratio a été appliquée à des systèmes multiéléments, comprenant deux alliages Mg-Al-Zn et trois minéraux standard [cyanite (Al_2SiO_5), albite ($NaAlSi_3O_8$) et orthoclase ($KAlSi_3O_8$)]. Les critères de sélection des standards ont été étendus à tous les standards contenant un ou plusieurs éléments cibles. Les influences du courant de faisceau, de l'énergie du faisceau et de la composition standard ont été étudiées. Il est démontré que le courant de faisceau n'a pas d'impact évident sur les résultats de la quantification. La méthode du *f*-ratio convient donc aux longues acquisitions, même en cas d'instabilité du flux d'électrons. De plus, en utilisant des facteurs de calibration dépendant de l'énergie du faisceau, la méthode du *f*-ratio peut atteindre une précision satisfaisante.

Contribution of Authors

This thesis was prepared according to the guidelines for a manuscript-based thesis. These guidelines are published by the Graduate and Postdoctoral Studies office of McGill University (http://www.mcgill.ca/gps/thesis/guidelines). The present thesis consists of the following four manuscripts which have been published or submitted for publications:

1. Teng, C., Demers, H., Brodusch, N., Waters, K. & Gauvin, R. (2018). Use of an annular silicon drift detector (SDD) versus a conventional SDD makes phase mapping a practical solution for rare earth mineral characterization. *Microscopy and Microanalysis* 24(3), 238-248. (Chapter 3).

2. Teng, C. & Gauvin, R. Multivariate statistical analysis on an SEM/EDS phase map of rare earth minerals. *Scanning* (in press). (Chapter 4).

3. Teng, C., Demers, H., Chu, X. & Gauvin, R. (2019). The *f*-ratio quantification method for X-ray microanalysis applied to Mg-Al-Zn alloys. *Microscopy and Microanalysis* 25(1), 58-69. (Chapter 5).

4. Teng, C., Yuan, Y. & Gauvin, R. (2019). The *f*-ratio quantification method applied to standard minerals with a cold field emission SEM/EDS. *Talanta* 204, 213-223. (Chapter 6)

Author contributions: Ms. Chaoyi Teng designed the experiment plans, conducted most of the experiments, analyzed the results and wrote the manuscripts, for all the four articles. Prof. Raynald Gauvin, actively supervised the research projects, provided guidance and edited the

manuscripts. Dr. Hendrix Demers wrote the main scripts for the simulations, and was involved in the experimental design, the result discussion and the revisions for Chapter 3 and Chapter 5. Prof. Kristian Waters provided the insights of the mineral processing on rare earth minerals for Chapter 3. Mr. Nicolas Brodusch provided assistance in conducting the EDS mapping in Chapter 3. Mr. Xin Chu was involved in the revisions for Chapter 3. Ms. Yu Yuan assisted to computing the fluorescence effects in Chapter 6.

Table of Contents

List of Figures

List of Tables

Chapter 1

Introduction

A scanning electron microscope (SEM) was initially designed as an imaging tool. Its application in the field of quantitative X-ray microanalysis did not commence until the development of a lithium drifted silicon [Si(Li)] detector designed for an energy dispersive spectroscopy (EDS) (Reed & Ware, 1973). In recent decades, the EDS detector was developed from the [Si(Li)] to the silicon drift detector (SDD), which greatly enhances the acquisition efficiency and energy resolution (Fiorini et al., 1997; Newbury & Ritchie, 2013a). Besides, the electron source in an SEM was developed from a thermionic emitter to a field emitter, which significantly improves its imaging capacity (Barkshire et al., 2000; Goldstein et al., 1981). These developments enable the SEM/EDS system to become a powerful tool for X-ray imaging and

quantitative microanalysis. However, its analytical efficiency and accuracy still have room for improvement, and it is the ultimate objective of this study.

In this work, the X-ray mapping analyses were performed on rare earth minerals (REMs). The industrial demands for rare earth elements (REEs) keep rising as a result of their increasing applications in high-technology electronic devices. As sources of these elements, the rare earth minerals (REMs) and their bearing ores are required to be characterized with more efficient and accurate techniques to weigh the REEs concentrations. However, an accurate mapping analysis on these samples is still a big challenge due to the small fraction of REMs in the raw ores and the low concentration of REEs in the REMs. Furthermore, the serious overlaps of REE L-lines and M-lines in an EDS spectrum limit the applications of EDS on the element analysis.

Taking the REMs as the research subject, which has various phases and complicated elemental constituents, the methods to improve the analytical efficiency of X-ray mapping were investigated. A cold field emission SEM (CFE-SEM) equipped with an annular SDD (aSDD) was used for the data acquisitions. The high brightness, small beam size, and low energy spread of the CFE contribute to an improved imaging resolution (Goldstein et al., 1981). Besides, the aSDD has an enhanced collecting count rate resulting from its special geometry without compromising the energy resolution and spatial resolution (Demers et al., 2013). In this study, the performances of the annular and the conventional SDDs were compared, and the optimal experimental conditions for aSDD were investigated.

The data processing methods for improving analytical efficiency were also studied. The recent studies show that the multivariate statistical analysis (MSA) performed on the map dataset can contribute to the noise reduction and phase identification (Kotula et al., 2003; 2006; 2012). In

this study, the principal components analysis (PCA) and the blind source separation (BSS), the two most popular MSA methods for X-ray microanalysis, were performed on the map datasets acquired on the REMs. In addition, the traditional elemental maps usually have issues of excessive noise and limited phase information, so phase map analysis was performed instead.

An *f*-ratio is calculated in the phase map analysis. The *f*-ratio of each element (f_i) at every pixel is calculated using the following equation:

$$f_i = \frac{I_i^{exp}}{\sum I_i^{exp}} \tag{1.1}$$

where I_i^{exp} is the net X-ray intensity of element *i* in a N-element system from one experimentally acquired spectrum (Horny, 2006). The *f*-ratios do not represent the real composition, but they are proportional to the concentrations of the corresponding elements. The phase identification relies on manually setting the thresholds of each phase with the constituent elemental *f*-ratios. The adjustable *f*-ratio range is important to analyze minerals as their chemical compositions are usually not constant. Equation (1.1) is also the theoretical basis of the recently developed *f*-ratio quantification method.

The quantitative X-ray microanalysis started with the Castaing equation (*k*-ratio method) (Castaing, 1951), which was originally designed for an electron probe microanalyzer/wavelength dispersive spectroscopy (EPMA/WDS) system. The development of the quantitative analysis based on an SEM/EDS system occurred several decades later, but it was rapidly applied across commercial and academic fields. The recent studies show that the EDS quantification performed with the standard-based *k*-ratio method is capable to reach the comparable accuracy and precision with the WDS (Ritchie et al., 2012). In order to eliminate the need of real standards and electron

dose measurements to simplify the experimental procedures, the EDS standardless analysis emerged, but the trade-off is the quantification accuracy (Newbury et al., 1995; Newbury & Ritchie, 2013b). Under these circumstances, the *f*-ratio method was developed as an alternative (Horny et al., 2010).

One distinctive feature of the *f*-ratio method is that it combines the conventional EDS acquisition and the Monte Carlo simulation. As shown in equation (1.2), the experimental characteristic X-ray intensities (I_i^{exp}) and the theoretically simulated intensities (I_i^{th}) are connected with the calibration factors between any two elements (Λ_{i-j}) in the unknown specimen, which are calculated with standards having known compositions.

$$f_i = \frac{I_i^{exp}}{\sum I_i^{exp}} = \frac{I_i^{th}}{I_i^{th} + \sum_{j \neq i} \Lambda_{i-j} I_i^{th}} \tag{1.2}$$

All the existing studies on the *f*-ratio method are in binary systems and the standards are limited to compound standards which contain all the target elements (Horny 2006; Horny et al., 2010). As a new quantification method, the *f*-ratio method still requires extensive validations to be performed in more complex systems. Furthermore, the option of standards requires to be extended since a proper compound standard is more difficult to find when the number of constituent elements increases. In this study, the *f*-ratio method was applied to multi-element systems, including two Mg-Al-Zn alloys and three standard minerals [kyanite (Al_2SiO_5), albite ($NaAlSi_3O_8$) and orthoclase ($KAlSi_3O_8$)]. The option of standards was extended to any standard having one or more target elements.

This thesis includes 7 chapters. Chapter 2 presents a review of the X-ray mapping and quantitative microanalysis theories. Chapter 3 compares the X-ray maps of REMs acquired with a

conventional and the annular SDDs, and investigates the optimal experimental conditions for the aSDD. Chapter 4 describes the performances of MSA on the REMs phase maps. Chapter 5 and Chapter 6 present the applications of the *f*-ratio quantification method in the multi-element systems: in Chapter 5, the use of pure-element (PE) standards is investigated in Mg-Al-Zn systems; in Chapter 6, the *f*-ratio method is applied to three certified minerals with up to 5 constituent elements, and the option of standards is extended to any standard specimen containing the target element. This thesis is completed with the conclusions, contributions to original knowledge and suggestions for future work in Chapter 7.

Chapter 2

Literature Review

In this chapter, a review of the theories of X-ray mapping and quantitative microanalysis based on a scanning electron microscope/energy dispersive spectroscopy (SEM/EDS) system is presented. Regarding the X-ray mapping, the key factors and the data processing methods are described. Regarding the quantitative X-ray microanalysis, the X-ray emission theories and current quantification methods are reviewed.

2.1 SEM/EDS Image Analysis

SEM is the most popular imaging tool for microstructure characterization, and its imaging formation relies on collecting signals generated from interactions between an incident electron beam and a solid specimen. Figure 2.1 illustrates the main signals generated inside a bulk specimen. The imaging modes based on secondary electrons (SE), backscattered electrons (BSE), and X-ray photons are most popular in an SEM/EDS system.

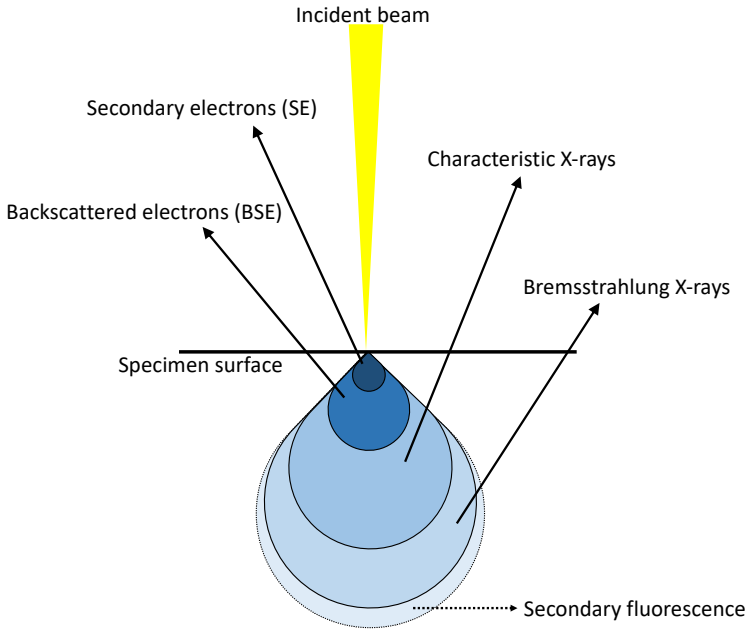

Figure 2.1 Signals generated during the beam-sample interaction.

An SE image mainly illustrates the topographic contrast since the SE yield is strongly dependent on the surface tilt angle (Kanter, 1961). A BSE image is mostly used to illustrate the compositional contrast due to the dependency of the backscattering coefficient on the atomic number (Goldstein et al., 1983; 2017). The BSE emission is also dependent on the surface tilt, but its larger interaction volume compared to the SE emission results in a worse spatial resolution for imaging the surface topography (Kohl & Reimer, 2008). Additionally, the X-ray mapping is the

most popular and convenient method to directly illustrate elemental distributions (Friel & Lyman, 2006).

2.1.1. X-ray mapping

X-ray mapping is performed by preselecting the energy window in a multichannel analyzer for certain characteristic X-ray lines to produce distribution maps of the corresponding elements. Due to the peak broadening effect of EDS, the window width is preferred to be set as 1.2* FWHM (full-width at half-maximum) of the peak (Fiori et al., 1988). However, an elemental X-ray map always has a noisy background resulting from the bremsstrahlung X-ray photons. In a routine X-ray mapping analysis, the short dwell time at each pixel usually leads to a higher elemental detection limit compared to a point analysis (Friel & Lyman, 2006). Recently, the multivariate statistical analysis (MSA) started to be applied to EDS map datasets to reduce the noise and improve the detection limit (Kotula et al., 2003; 2006; 2012).

Based on qualitative X-ray maps, the quantitative maps can be processed by applying the atomic number/absorption/fluorescence (ZAF) matrix corrections at each pixel to calculate the corresponding composition. However, the standard-based quantitative mapping on heterogeneous samples is still a challenge as the correction factors vary with the phase compositions (Newbury & Ritchie, 2013b). Additionally, a long acquisition time is usually required since a collection of statistically enough X-ray counts is a prerequisite to accurate spectrum background subtraction and composition calculation. However, for a cold field emission SEM (CFE-SEM), its unstable

beam current during the long-time acquisition makes the quantitative mapping more problematic (Teng et al., 2018).

As an alternative to the traditional elemental map, a phase map is more informative, which can directly illustrate the phase distribution and does not have the issue of excessive noise. More and more commercial software associated with the EDS acquisition has the function of phase analysis, e.g., the AZtec Energy from Oxford Instrument, which can automatically find the phases with similar composition (Teng et al., 2015). Additionally, the open source Python script, pyPhaseMap (available on GitHub as pyphasemap repository) can also convert the elemental maps into a phase map by manually defining each phase (Teng et al., 2018; Teng & Gauvin, 2019a). A concentration-concentration histogram is helpful to determine the associations between any two elements, and further assists to identifying phases (Bright & Newbury, 1991).

2.1.2. Key factors for X-ray mapping

An accurate element identification is the primary task in an X-ray mapping analysis. To achieve this goal, it is important to collect sufficient characteristic X-ray counts to overwhelm the spectrum background. Also, a good energy resolution is required to avoid severe peak overlaps. Regarding the elemental distribution in X-ray maps, the spatial resolution determines how much detail can be observed. Hence, the X-ray count rate, the energy resolution, and the spatial resolution are considered as the three key factors for X-ray mapping.

2.1.2.1. Count rate

In the past, the use of lithium drifted silicon [Si(Li)] detector limited the EDS collecting count rate, producing poor mapping statistics for minor and trace elements. The development of the silicon drift detector (SDD) (Strüder et al., 1998) enhanced the X-ray throughput by a factor of 25 to 70, which greatly improved the mapping capability (Newbury & Ritchie, 2013a). The SDD enables ten million counts accumulated in 100 s while keeping the dead time around 10% (Newbury & Ritchie, 2013a). Additionally, the window optimization, such as the ultra-thin window or the windowless detector, can also improve the collecting efficiency by reducing the absorption from the detector window, especially for the light elements (Burgess et al, 2016).

For a certain type of EDS detector, the count rate is decided by the real detector size and the specimen-detector distance, which is described using the solid angle Ω (Zaluzec, 2014):

$$\Omega = \frac{A}{{d_{SD}}^2} \tag{2.1}$$

where A (mm^2) refers to the collecting area of the detector; and d_{SD} (m) refers to the specimen-detector distance from the detector face to the beam impact point. Enlarging sensor size is a common choice to improve the sensitivity of the detector to the X-ray photons, but the energy resolution will be compromised since the electronic noise is generated while the X-rays travelling inside the sensor (Bell & Erdman, 2012). The alternative is to shorten the distance between the detector and the sample, and the recently designed annular SDD (aSDD) has the minimum d_{SD}, which results in an improved collecting efficiency without sacrificing the energy resolution (Kotula et al., 2008; Demers et al., 2013; Teng et al., 2018).

However, the count rate [usually in the unit of kilocounts per second (kcps)] for generating X-ray maps does not keep increasing with the input count rate collected by the detector due to the existence of the dead time, which means the period when the detector is busy with processing the previous X-ray photons and cannot deal with the coming ones (Goldstein et al., 1981). The relation between the output count rate used for generating maps (R_{out}) and the input count rate collected into the pulse processor (R_{in}) can be described as (Knoll, 2010):

$$R_{out} = R_{in} e^{-R_{in}\tau} \tag{2.2}$$

where τ (s) describes the dead time, which is also considered as the real processing time for each photon. However, for most commercial software, the dead time fraction (T_{DT}) is used to describe the relation between R_{out} and R_{in}:

$$T_{DT} = \frac{R_{in} - R_{out}}{R_{in}} \tag{2.3}$$

As shown in equation (2.2), R_{out} increases with the decrease of τ. Whereas, the decrease of τ will deteriorate the energy resolution, which has direct influences on the element identification.

2.1.2.2. Energy resolution

The energy resolution of an EDS spectrum is usually described using the FWHM of Mn Kα peak and Ti Lα peak for the high and low energy ranges, respectively (Statham, 1998). Theoretically, FWHM depends on X-ray counts energy and electronic noise, which can be described as (Goldstein et al., 1981):

$$FWHM \propto (C^2 E + N^2)^{1/2} \tag{2.4}$$

where C is the uncertainty in the formation of charge carriers; E is the X-ray energy; and N is the FWHM of electronic noise generated during the amplification process, which is decided by the real processing time τ. The elongated processing time per count can significantly decreases the electronic noise and improves the energy resolution, but it may also cause a high dead time, which is the main reason for pulse pile-up distortions (Wielopolski & Gardner, 1976).

An SDD (Mn Kα ~ 125 eV FWHM) realizes an improvement compared to a [Si(Li)] detector (Mn Kα ~ 132 eV FWHM) (Fiorini et al., 1997), but the energy resolution of the EDS is still inferior to that of the wavelength dispersive spectroscopy (WDS), which has the peak width between 2 eV to 20 eV depending on the photon energy (Wollman et al., 1997). However, a recent study shows that the microcalorimeter EDS can achieve the energy resolution of 2 - 5 eV over the energy range between 200 eV to 10 keV by measuring the temperature rise in a metal absorber (Newbury, 2006). In addition, the spectral fitting and relative simulations can further process the peak deconvolution and improve the accuracy of X-ray intensity extraction (Duncumb et al., 2001; Ritchie et al., 2012).

2.1.2.3. Spatial resolution

An accelerating voltage over 10 keV is usually applied for routine X-ray microanalyses, aiming to excite statistically enough counts (Barkshire et al., 2000). Compared to the conventional tungsten or LaB6 thermionic emitters, the field emitter has much higher brightness, which enables the SEM to be operated at a lower accelerating voltage still with sufficient beam current (Barkshire et al., 2000). The low beam energy benefits a reduced volume of X-ray generation beneath a sample surface, which deadens to an improved spatial resolution of X-ray microanalysis.

The Monte Carlo simulation is popular for studying the X-ray depth and the lateral distribution beneath the specimen surface (Murata et al., 1971; Reed, 1997), which are usually described with the $\varphi(\rho z)$ curves (Packwood & Brown, 1981; Pouchou & Pichoir, 1984). More detailed descriptions of the Monte Carlo simulation performed on SEM imaging and X-ray microanalysis can be found in previous works of Murata et al.(1971) and Gauvin (2005). Figure 2.2 illustrates the simulation results of the interactions between the electron beam and a Mg-Al-Zn alloy (its chemical formula was assumed as MgAlZn) at 30 kV and 5 kV computed by the CASINO2 program (Drouin et al., 2007). The electron trajectories inside the specimen (black trajectories) and the $\varphi(\rho z)$ curves of Al-Kα along the mass-depth (blue for the generated X-ray photons and red for the emitted photons) at each beam energy are displayed. The characteristic X-ray generation range is always smaller than the electron range, as only the electrons with energies exceeding the critical ionization energy of a specific electronic shell or subshell can produce the characteristic X-ray photons (Goldstein, et al., 1981).

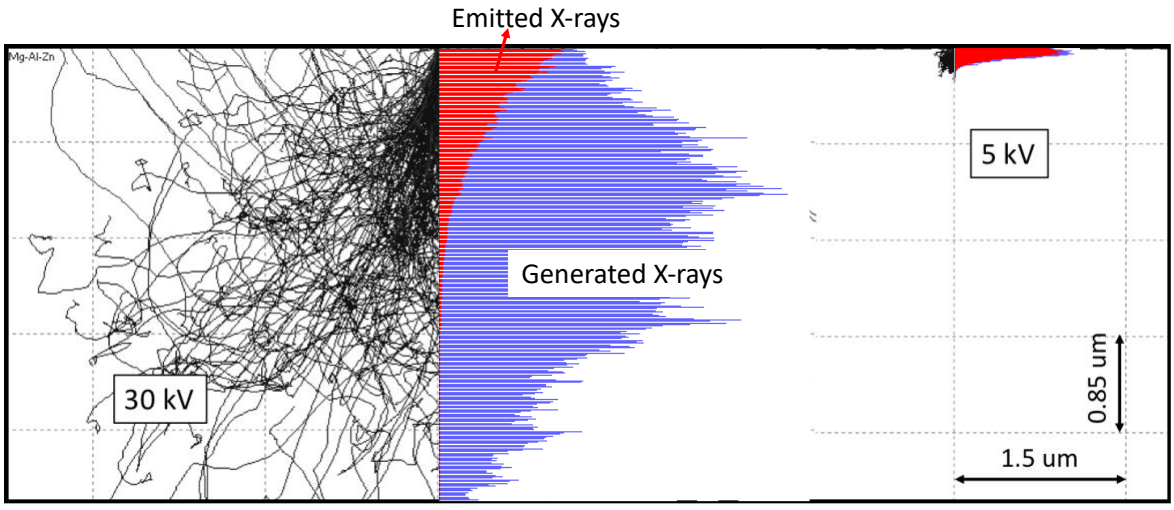

Figure 2.2 Electron trajectories and $\varphi(\rho z)$ curves of the generated and emitted Al-Kα X-ray photons within a Mg-Al-Zn alloy at 30 kV and 5 kV. For the $\varphi(\rho z)$ curves, the horizontal axis is X-ray intensity and the vertical axis is the mass-depth, which is defined as ρz.

The first method for calculating the X-ray generation range X_G was developed by Anderson and Hasler (1966):

$$X_G = \frac{0.064}{\rho_{Spec}} (E_0^{1.68} - E_C^{1.68}) \quad (2.5)$$

where ρ_{Spec} is the specimen density (g/cm3); E_0 is the incident electron energy (keV); and E_C is the critical ionization energy of the electronic subshell of the characteristic lines (keV). However, as shown in Figure 2.2, the X-ray emission depth is significantly reduced by the absorption effect, so the calculation for the real X-ray emission range X_E with the consideration of absorption effect was modified as (Gauvin, 2007):

$$X_E = ln\,(\frac{1}{1-\alpha})\lambda\, sin\,\psi\,(1 - e^{-\frac{X_G}{ln(\frac{1}{1-\alpha})\lambda sin\,\psi}}) \quad (2.6)$$

where $ln\,(\frac{1}{1-\alpha})$ is the prefactor for $\lambda \sin \psi$; ψ is the take-off angle of the X-ray detector; and λ is the mean free path for the absorption of the characteristic X-ray photons:

$$\lambda = \frac{1}{\rho_{Spec} \sum_{i=1}^{n} C_i \frac{\mu}{\rho}\Big|_i} \quad (2.7)$$

where C_i is the weight fraction of element *i*; and $\frac{\mu}{\rho}\Big|_i$ is the mass-absorption of the characteristic X-ray line of element *i*.

2.1.3. Multivariate statistical analysis (MSA) for X-ray mapping

One premise for an accurate X-ray mapping analysis is collecting sufficient characteristic X-ray counts to overwhelm the bremsstrahlung counts. To achieve that, the simplest way is to extend the acquisition time, but the analytical efficiency will be sacrificed. An alternative method is to apply the MSA on the map dataset to extract useful information (Kotula et al., 2003). The MSA algorithms treat the map dataset as a set of spectrum images (SIs), and compare the spectra at each pixel, looking for similarities and differences without any prior assumptions. Figure 2.3 schematically illustrates the SI data cubes in a 2D compositional map [Figure 2.3(a)] (Kotula et al., 2003) and a 3D map with tomographic information [Figure 2.3(b)] (Kotula et al., 2006).

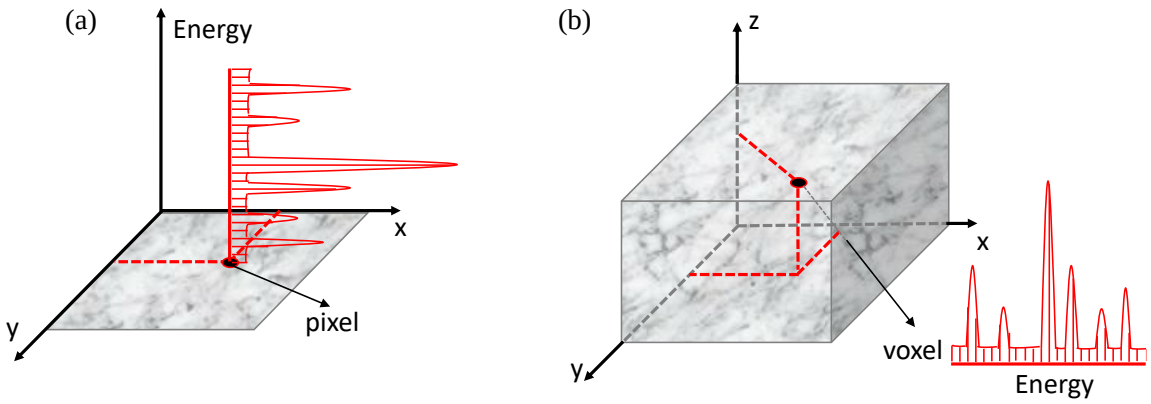

Figure 2.3 Schematic of the 2D (a) and the 3D (b) spectral image data cube.

During the MSA computation, the original spectrum at each pixel or voxel is considered as a linear combination of a set of MSA-determined component and their respective amplitudes, which can be described as (Kotula et al., 2003):

$$s_i = C_{(i,1)}S_1 + C_{(i,2)}S_2 + C_{(i,3)}S_3 + \cdots + C_{(i,n)}S_n + E_i \quad (2.8)$$

where s_i represents the *i*th raw spectrum in the original dataset; *n* describes the number of non-noise components; $C_{(i,n)}$ represents the amplitude or weighting of the component spectrum S_n; and E_i is the residual. Thus, the original SIs dataset can be described as a matrix $\boldsymbol{D}$, which is composed of two matrixes:

$$\boldsymbol{D} = \boldsymbol{C} \cdot \boldsymbol{S^T} \tag{2.9}$$

where $\boldsymbol{C}$ represents the matrix of components; $\boldsymbol{S}$ represents the matrix of components spectral shapes; $\boldsymbol{T}$ denotes the matrix transpose (Kotula et al., 2003; 2006). In this manner, the original dataset is decomposed into a limited number of components, and the variation of each component can be used to differentiate the phases and noise (Parish & Brewer, 2010; Titchmarsh, 1998). Taking advantage of this feature, the MSA can be used to exploit the redundancy of original dataset and determine the chemical constituents before the quantitative analysis (Kotula et al., 2012).

2.1.3.1. Principal component analysis (PCA)

Among the various MSA methods, the principal component analysis (PCA) is the most popular one, which performs the orthogonal factorization on the original dataset, and creates a set of orthogonal principal variables (Wold et al., 1987). There are several algorithms available to perform PCA, such as the singular value decomposition (SVD) (Malinowski, 2002) and the maximum likelihood PCA (MLPCA) (Wentzell et al., 1997). The common applications of the PCA on X-ray microanalysis are dimensionality reduction and noise subtraction, via ordering the decomposed components as decreasing variations without physical considerations, maintaining the leading components with higher variances which are assumed to contain all the useful information, and discarding the rest as noise (Trebbia & Bonnet, 1990).

Additionally, the PCA algorithms can be applied to EDS spectra to remove the bremsstrahlung X-ray counts and extract the characteristic X-ray intensities through noise filtering and peak fitting, which can shorten the required acquisition time and improve the reliability of background subtraction (Saghi et al., 2016; Titchmarsh, 1999). Thus, a more accurate quantitation can be achieved with the improved net X-ray intensity extraction. Furthermore, the PCA can be directly applied to EDS maps to differentiate particles according to the chemical compositions and the morphologies (Genga et al., 2012). However, the orthogonal constraint followed by the PCA algorithms may result in difficulties in physically interpreting the decomposed components.

2.1.3.2. Blind source separation (BSS)

The blind source separation (BSS), by contrast, is an alternative to unmix the original dataset into a limited number of statistically independent components, aiming to capture the essential data structure (Cardoso, 1998). It assumes that the observation is a mixture $[x_1(t), \dots, x_n(t)]$, which is composed of a limited number of independent signals $[s_1(t), \dots, s_n(t)]$, and their relations can be described with matrix as:

$$\boldsymbol{x}(t) = A\boldsymbol{s}(t) \tag{2.10}$$

where $\boldsymbol{s}(t)$ represents the source signals; $\boldsymbol{x}(t)$ represents the observed signals; and A is the mixture coefficient. Thus, the goal of the BSS analysis is to recover the source signals using the observed mixture, and the estimation of the sources can be described as:

$$\boldsymbol{y}(t) = B\boldsymbol{x}(t) \tag{2.11}$$

with a separating matrix B.

The independent component analysis (ICA) (Hyvärinen & Oja, 2000) and the non-negative matrix factorization (NMF) (Lee & Seung, 1999) are the two most popular methods to perform the BSS analysis. When the BSS is applied on the X-ray signals, each generated component is considered as a typical event occurring between the electron beam and the sample (de la Pena et al., 2011). Regarding the BSS applications on EDS analysis, the ICA has been used to directly separate the phases with different compositions instead of the traditional elemental identification method (Rossouw et al., 2015a; 2015b; 2016). However, negative values are inevitably generated as both combinations and subtractions are allowed during the ICA calculations, which may result in the physically uninterpretable components (Wu et al., 2010; Zhang, 2017). In this case, the NMF algorithm, which only allows additive combinations and prevents subtractions to force all components to be strictly non-negative, has more realistic applications in X-ray microanalysis (Jany et al., 2017; Wu et al., 2010). However, it is not proper for quantitative analyses as the non-negative constraint may introduce bias into the component separation (Kotula et al., 2012).

2.2. Quantitative X-ray Microanalysis

Quantitative X-ray microanalysis is developed based on the principle that the generated characteristic X-ray intensity of an element is dependent on its concentration. The SEM/EDS system, which has the advantages of quick analysis and easy operability, becomes one of the most popular quantification techniques. In this section, the generation and emission of characteristic X-

ray photons are thoroughly studied, and the current quantitative X-ray microanalysis methods are reviewed.

2.2.1. Characteristic X-ray generation and emission

From generation to emission, and to final detection, the X-ray photons go through a complicated process, which involves multiply physical interactions with the bulk specimen and the detector window layers. In this section, the fundamental parameters for X-ray generation, emission, and detection are introduced, and their experimental and theoretical determination methods are reviewed.

2.2.1.1 Fundamental X-ray generation parameters

X-ray photons are generated in the interactions between an electron beam and a solid specimen. A characteristic X-ray has an energy specific to the element, and the dependence of the characteristic X-ray intensity on its elemental concentration is the theoretical basis for the quantitative X-ray microanalysis. The study of X-ray generation started from thin foils, where the electrons can pass through the specimen without significant deflection and energy loss. In such an ideal case, the number of X-ray photons generated per incident electron in a thin film with thickness of *t* for the element *i* can be calculated as (Horny, 2006):

$$n_i = \frac{N_A C_i}{A_i} Q_i \omega_i \alpha_i (1 + T_{CK,i}) \rho t \tag{2.12}$$

where N_A is the Avogadro number; C_i the weight fraction of element i; A_i the atomic weight ; Q_i the ionization cross-section; ω_i the fluorescence yield; α_i the line fraction; $T_{CK,i}$ the Coster-Kronig transition coefficient; and ρ is the material weight density.

Equation (2.12) incorporates the fundamental parameters for X-ray generation, which can be determined with empirical, or semi-empirical, or totally theoretical formulations. However, the theoretical determinations usually show wide discrepancy with the experimental measurements. Among all these theoretical parameters shown in equation (2.12), the most important one is the ionization cross section (Q), which describes the probability of inner shell ionization, and was originally established by Bethe (Powell, 1976; Goldstein et al.,1981):

$$Q = 6.51 \times 10^{-20} \frac{n_s b_s}{E E_c} ln\left(\frac{c_s E}{E_c}\right) \tag{2.13}$$

where E is the incident electron energy (keV); E_c is the critical ionization energy for a given electron bound (keV); n_s is the number of electrons in the shell or subshell (e.g., n_K = 2), b_s and c_s are the constants for a given shell. Powell (1976) validated the above equation with experimental data for K-lines in the overvoltage ($U = E/E_c$) range of 4 to 25. Another formula which incorporates the relativistic effects was developed by Zaluzec (1984):

$$Q = 6.51 \times 10^{-20} \frac{n_s b_s}{E_r E_c} [ln\left(\frac{c_s E_r}{E_c}\right) - \ln(1-\beta^2) - \beta^2] \tag{2.14}$$

where β is the ratio of the speed of the electron to that of light; $E_r = \frac{m_0 v^2}{2}$, where m_0 is the election mass at rest. In this equation, the upper limit of the incident beam energy was defined at 30 keV. However, in the above two models, there are still parameters requiring to be experimentally determined, so any inaccurate measurements may introduce uncertainties into the

whole calculation. Thus, Casnati (1982) developed a semiempirical model for K-lines within the overvoltage range from 1 to 20 for the elements with atomic number ranging from 6 to 79:

$$\mathrm{Q} = n_s a_0^2 R \left(\frac{I_0}{I_K}\right)^2 \psi \phi \frac{lnU}{U} \tag{2.15}$$

$$\psi = \left(\frac{I_K}{I_0}\right)^{d_0 + \frac{d_1}{U} + \frac{d_2}{U^2}} \tag{2.16}$$

$$\phi = b_0 e^{\frac{b_1}{U} + \frac{b_2}{U^2}} \tag{2.17}$$

where $a_o = 5.29 \times 10^{-11} m$, which is the Bohr radius; R is relativistic factor of Gryziński (1965); I_K is the minimum energy required for the transition of a K electron to the continuum; $I_0 = 13.606$ eV, which is called the Rydberg energy; and $d_0, d_1, d_2, b_0, b_1, b_2$ are the constants for K-lines. The Casnati model was the most used one for computing the ionization cross section until Bote and Salvat (2008) developed a new model with their own Monte Carlo program, Penelope (Salvat et al., 2006). They succeeded in computing the ionization cross section for all elements (atomic number between 1 to 99) and most subshells (Bote & Salvat, 2008; Bote et al., 2009).

The fluorescence yield ωi determines the probability of generating a characteristic X-ray photon or an Auger electron. A large number of researchers made efforts to theoretically calculate this parameter with semi-empirical formulae (Krause, 1979) or Dirac-Hartree-Slater model (Chen et al., 1981; Puri et al., 1993). Most recently, Joy (2001) and Campbell (2003) compared the theoretical calculations with the experimental data, and Campbell (2003) summarised the database which is widely used at present. However, most of the existing studies focus on the calculations for K and L subshells, so more studies on M subshells are still needed. In addition, the fluorescence yield is intimately related to the Coster-Kronig transition ($1+T_{CK,i}$), which accounts for the

nondirect ionization for vacancies produced by nonradiative transitions between subshells in L and M shells. Thus, in the above cited studies, such as Chen et al. (1981) and Campbell (2003), the computations of the Coster-Kronig transition are also presented.

The line fraction α_i represents the probability of exciting a specific line when the corresponding subshell is ionized. Schreiber et al. (1982) and Scofield (1974) established the lists of theoretical line fractions for K-lines and L-lines, respectively, and their accuracy was evaluated by Pia et al. (2009). Regarding M-lines, Chen et al. (1984) calculated the values for the elements ranging from Cd (atomic number 48) to U (atomic number 92).

2.2.1.2 X-ray emission in a bulk solid

The $\varphi(\rho z)$ curve was proposed to calculate the X-ray emission in a bulk solid by Castaing (1951). He sliced the bulk into multiple thin layers with thickness of Δz along the mass depth, and summarized the X-ray emission from each layer with the consideration of absorption and fluorescence effects. The $\varphi(\rho z)$ theory is schematically illustrated in Figure 2.4, and equation (2.12) is modified to calculate the emitted X-ray intensity in a bulk as:

$$I_{i,e} = \frac{i_p \tau}{e} \frac{N_A c_i}{A_i} Q_i \omega_i \alpha_i \left(1 + T_{CK,i}\right)(1 + \delta_i) \int_0^\infty \varphi_i(\rho z) e^{-\chi_i \rho z} d(\rho z) \qquad (2.18)$$

The term $\frac{i_p \tau}{e}$ is to calculate the number of electrons with the electron beam current i_p, the acquisition time τ, and the electron charge e. The term $(1 + \delta_i)$ describes the fluorescence effects, including the contributions from the characteristic X-ray photons with higher energy, the bremsstrahlung X-rays, the stray electrons, the backscattered electrons, and the Auger electrons. The term $\int_0^\infty \varphi_i(\rho z) e^{-\chi_i \rho z} d(\rho z)$ describes the emitted X-ray intensity with the absorption effect,

where $\varphi_i(\rho z)$ describes the generated X-ray intensity with mass depth and χ_i refers to the absorption parameter, which is defined as:

$$\chi_i = csc\,\psi \sum_{j=1}^{n} c_i \frac{\mu}{\rho}\Big|_j^i \tag{2.19}$$

where ψ is the take-off angle of the detector; $\frac{\mu}{\rho}\Big|_j^i$ is the mass-absorption of the characteristic line of element *i* into the absorbing element *j*. To calculate χ_i, the summation is taken for all constituent elements in the specimen (Gauvin, 2012).

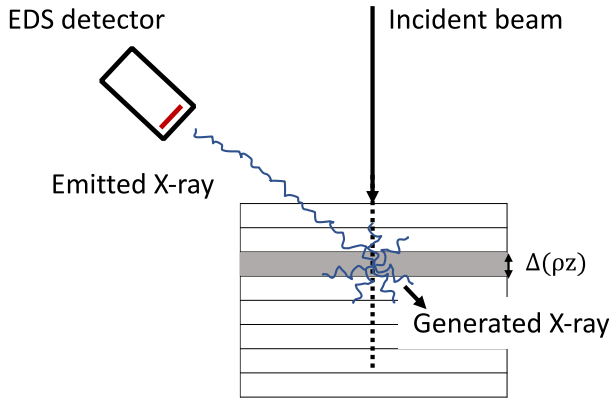

Figure 2.4 Schematic diagram of the X-ray generation and emission per $\Delta(\rho z)$ layer.

2.2.1.3 X-ray detection

Furthermore, the effects of detector efficiency and solid angle should be considered in the calculation of the detected X-ray intensity, which can be described with the universal equation:

$$I_i = \left(\frac{\Omega}{4\pi}\right)\varepsilon_i I_{i,e} \tag{2.20}$$

where Ω refers to the solid angle; and ε_i refers to the detector efficiency to the element i. In order to determine the detector efficiency, the thickness of each layer in the window should be known, and the absorption factor of each layer should be calculated. Alvisi et al. (2006) introduced a new method to measure the detector efficiency for most SEM/EDS systems. In this method, the efficiency of a reference spectrometer is determined firstly, and an efficiency transfer procedure is performed to get the efficiency of an unknown spectrometer. In addition, Goldstein et al. (2017) summarized the detector efficiency as a function of X-ray photon energy for different window types. Regarding the solid angle, equation (2.1) gives a simplified estimation, but a more precise calculation should be performed as:

$$\Omega = 2\pi\left(1 - \frac{D}{\sqrt{D^2+d^2}}\right) \tag{2.21}$$

where D is the distance from the incident point on the specimen surface to the detector crystal surface; and d is the detector crystal diameter (Zaluzec, 2014).

2.2.2. Current quantification methods

The most used quantification method for either an SEM/EDS system or an electron probe microanalyzer/WDS (EPMA/WDS) system is the Castaing equation (Castaing, 1951). For a thin foil in a transmission electron microscopy (TEM), a Cliff-Lorimer equation is usually applied, which neglects the absorption and fluorescence effects (Cliff & Lorimer, 1975). With the increasing applications of scanning transmission electron microscopy (STEM), the ζ-factor method becomes more widely used as it enables the measurements of chemical composition and specimen thickness at the same time (Watanabe et al., 1996). In this section, the current

quantitative X-ray microanalysis methods are reviewed, and a new quantification method, the *f*-ratio method (Horny, 2006), which was developed based on the Cliff-Lorimer equation but designed for an SEM/EDS system, is also introduced.

2.2.2.1 Castaing equation

Castaing (1951) was the first one who built the relation between the specimen chemical composition and its emitted X-ray intensities. Since most of the X-ray generation parameters were not accurately known at that time, a standard specimen was analyzed to calculate the ratio of the characteristic X-ray intensities of the same element in the unknown specimen to that in the standard to eliminate the need of computing absolute X-ray intensities. The Castaing equation is also well known as the *k*-ratio method, which is calculated as:

$$\frac{C_i}{C_i^0} = \frac{I_i}{I_i^0} = k_i \tag{2.22}$$

where C_i and C_i^0 are the concentrations of the element *i* in the specimen and the standard; I_i and I_i^0 are the intensities of the same peak of the same element in the specimen and the standard.

In the equation (2.22), a few assumptions are made: the absorption and fluorescence effects are assumed to be very small, and the standard and the unknown specimen are assumed to have similar chemical constituents. However, this is far from the real analytical cases, so a matrix correction should be applied. Through combining equation (2.22) with equation (2.18) which describes the emitted characteristic X-ray intensity, the complete Castaing equation for a real bulk can be described as:

$$k_i = \frac{I_i}{I_i^0} = \frac{(1+\delta_i)\int_0^\infty \varphi_i(\rho z)e^{-\chi_i \rho z}d(\rho z)}{(1+\delta_i^0)\int_0^\infty \varphi_i^0(\rho z)e^{-\chi_i^0 \rho z}d(\rho z)}\frac{C_i}{C_i^0} \tag{2.23}$$

with the cancellation of the ionization cross-section Q_i, the fluorescence yield ω_i, the line fraction α_i, and the Coster-Kronig transition coefficient $T_{CK,i}$, all of which are only dependent on the specific element. Additionally, this method requires the unknown specimen and the standard to be analyzed at the same beam condition, so the beam current i_p is also cancelled out.

The matrix correction shown in equation (2.23) is also well known as the ZAF correction, which is widely implemented in any EDS or WDS analytical software, and it has a universal description as:

$$\frac{C_i}{C_i^0} = [ZAF]_i \frac{I_i}{I_i^0} = [ZAF]_i k_i \tag{2.24}$$

The matrix effects are divided into three: the atomic number Z_i, the absorption A_i, and the fluorescence F_i effects. The atomic number and the absorption corrections are usually calculated as a whole with the $\varphi_i(\rho z)$ models (Bastin et al., 1998; Merlet, 1994; Pouchou & Pichoir, 1984):

$$[ZA]_i = \frac{\int_0^\infty \varphi_i(\rho z)e^{-\chi_i \rho z}d(\rho z)}{\int_0^\infty \varphi_i^0(\rho z)e^{-\chi_i^0 \rho z}d(\rho z)} \tag{2.25}$$

They also can be calculated separately. Duncumb and Reed (1968) proposed the calculation of the atomic number effect Z_i as:

$$Z_i = \frac{R_i^0 \int_{E_{c,i}}^{E_0} \frac{Q_i}{S_i^0} dE}{R_i \int_{E_{c,i}}^{E_0} \frac{Q_i}{S_i} dE} \tag{2.26}$$

where R_i^0 and R_i are the backscattering correction factors for element *i* in the standard and the specimen respectively; S_i^0 and S_i are the stopping power for element *i* in the standard and the specimen. The individual absorption effect A_i can be calculated with the absorption terms $f^0(\chi_i)$ and $f(\chi_i)$ in the standard and the specimen (Goldstein & Williams, 1977):

$$A_i = \frac{f^0(\chi_i)}{f(\chi_i)} \tag{2.27}$$

$$f(\chi_i) = \frac{\int_0^\infty \varphi_i(\rho z) e^{-\chi_i \rho z} d(\rho z)}{\int_0^\infty \varphi_i(\rho z) d(\rho z)} \tag{2.28}$$

The fluorescence effect is usually calculated with the Reed's method (Reed, 1965):

$$F_i = \frac{(1+\sum_j \frac{I_{ij}^f}{I_i})^0}{(1+\sum_j \frac{I_{ij}^f}{I_i})} \tag{2.29}$$

where $\frac{I_{ij}^f}{I_i}$ is the ratio of emitted X-rays intensity of element *i* by fluorescence effect from element *j* to the its actually produced primary X-ray intensity.

2.2.2.2 Quantification method for a thin film

The Cliff-Lorimer method was firstly proposed for a TEM with the assumption that the specimen is thin enough for neglecting the absorption and fluorescence effects (Cliff & Lorimer, 1975). In this method, the ratio of characteristic X-ray intensities of two elemental in one spectrum is calculated and converted into the ratio of their concentrations with a Cliff-Lorimer factor, K_{A-B}:

$$\frac{C_A}{C_B} = K_{A-B}\frac{I_A}{I_B} \tag{2.30}$$

Through combining equation (2.30) with equation (2.12) which describes the X-ray generation in a thin film and equation (2.20) which calculates the detector effects, the Cliff-Lorimer factor is deduced as:

$$K_{A-B} = \frac{Q_B\omega_B\alpha_B\varepsilon_B A_A}{Q_A\omega_A\alpha_A\varepsilon_A A_B} \tag{2.31}$$

with the cancellation of the same items for the two elements since they are from one spectrum. Additionally, the Coster-Kroning transition usually does not need to be considered, as K-lines can be used in most cases due to the high beam energy in a TEM.

As shown in equation (2.31), the Cliff-Lorimer factor is compositionally independent and can be determined theoretically or experimentally. Even though the locally experimental determination has a better accuracy (Sheridan, 1989; Wood et al., 1984; Watanabe & Williams, 2006), a database of therotically determined Cliff-Lorimer factors is applied in most commercial software packages (Parisini et al., 2018), as the standard thin films with known compositions are not always available.

With the increasing applications of an STEM, the demand for an accurate quantitative analysis on a thin film keeps rising. However, in most real cases, the specimen is not thin enough for neglecting the absorption and fluorescence effects, so a more accurate Cliff-Lorimer equation should be descried as:

$$\frac{C_A}{C_B} = K_{A-B}A_{A-B}F_{A-B}\frac{I_A}{I_B} \tag{2.32}$$

with the considerations of absorption A_{A-B} and fluorescence F_{A-B} corrections. However, the calculations of A_{A-B} and F_{A-B} require the knowledge of the specimen thickness, which is difficult to be accurately measured and may introduce uncertainties into the final quantification results (Anderson et al., 1995; Goldstein & Williams, 1977; Parisini et al., 2018).

Under this circumstance, Watanabe et al (1996) developed the ζ-factor method which is able to determine the specimen composition and thickness at the same time. In the ζ-factor method, the characteristic X-ray intensity I_A is connected to the specimen mass-thickness ρt and its elemental concentration C_A with a proportional factor ζ_A:

$$\rho t = \zeta_A \frac{I_A}{C_A D_e} \tag{2.33}$$

where D_e is the total electron dose during the acquisition (Watanabe & Williams, 2006). Combining equation (2.33) with equations (2.12) and (2.20), ζ_A can be theoretically described as:

$$\zeta_A = \frac{A_A}{N_A Q_A \omega_A \alpha_A (\frac{\Omega}{4\pi}) \varepsilon_A} \tag{2.34}$$

As shown in equation (2.34), the ζ-factor is independent of the electron dose, the specimen composition and thickness, but this method requires the electron dose during the acquisition to be accurately measured, causing this method not suitable for the system with unstable beam current.

2.2.2.3 The *f*-ratio method

By contrast, the *f*-ratio method is a quantification method specifically designed for the system with unstable beam current, e.g. a CEF-EM (Horny, 2006). The significant small source size (< 5 nm) and low energy spread (~ 0.3 eV) contribute the cold field emitter as one of the

most popular source types for an EM, but its fluctuant current limits its use in the quantitative X-ray microanalysis, either using the Castaing method for a bulk specimen or using the ζ-factor method for a thin film (Goldstein et al., 1981). Thus, the emerge of the *f*-ratio method overcomes this limitation.

Inspired by the Cliff-Lormier equation, the *f*-ratio method also uses the ratio of X-ray intensities from the same spectrum to eliminate the beam current effects, but the difference is that the *f*-ratio method sums the X-ray intensities of all the constituents in the denominator. One distinctive feature of the *f*-ratio method is that it combines the conventional EDS acquisition and the Monte Carlo simulation. Equation (2.35) shows the definition of the *f*-ratio with the experimental X-ray intensities (I_i^{exp}) and the theoretically simulated intensities (I_i^{th}) in a multi-element system (Teng & Gauvin, 2019b):

$$f_i = \frac{I_i^{exp}}{\sum I_i^{exp}} = \frac{I_i^{th}}{I_i^{th} + \sum_{j \neq i} \Lambda_{i-j} I_i^{th}} \tag{2.35}$$

where Λ_{i-j} represents the calibration factor between any two elements, which is calculated with a standard having the known composition. The calibration factor is used to calibrate the differences between the experiments and simulations, as there are still uncertainties remaining in the theoretical calculations of the detected X-ray intensity.

This method was firstly applied to a set of binary Cu-Au alloys using a 60 wt.% Cu - 40 wt.% Au alloy as the standard (Horny et al., 2010). The use of a compound standard containing all the target elements enables the whole quantification process to be independent of the beam current, but such a proper standard becomes more difficult to find when the number of constituent elements increases. Thus, the use of pure-element (PE) standards was investigated in the ternary Mg-Al-Zn

systems, and a good consistency was obtained between the PE-standard-based quantification results and the compound-standard-based results (Teng et al., 2019). And then, the option of standards was extended to any standard specimen containing the target elements, and the certified minerals with up to 5 constituent elements were quantified with a satisfactory accuracy (Teng & Gauvin, 2019b). So far, the limited applications of the *f*-ratio method all give an accuracy better than 5 % with the beam-energy-dependent calibration factors.

2.2.3. Monte Carlo simulations for X-ray microanalysis

There are various Monte Carlo simulation programs developed for X-ray microanalysis. Specifically, for the EDS, the most popular programs are CASINO (Hovington et al., 1997), CASINO2 (Drouin et al., 2007), Win X-ray (Gauvin et al., 2006), MC X-ray (Gauvin & Michaud, 2009), Penelope (Salvat et al., 2006), and DTSA-II (Ritchie, 2011b; 2012).

CASINO was developed to quickly calculate and display electron-solid interactions for a variety of beam conditions and sample geometries. The first version of CASINO (Hovington et al., 1997) was designed for expert users and has some limitations on data handling capabilities, so Drouin et al. (2007) developed a much simpler version, CASINO2. Furthermore, one feature of CASINO2 is to model the beam interactions in bulk samples and thin foils at a low beam energy. Win X-ray (Gauvin et al., 2006) is an extension to CASINO, which can be used to compute the trajectories of BSE and trapped electrons, and to calculate the X-ray $\varphi(\rho z)$ curves and complete spectra. Also, Win X-ray can be used to simulate the charging effect for an insulating specimen. MC X-ray (Gauvin & Michaud, 2009) is an extension to CASINO and Win

X-ray, which was designed to simulate the electron scattering in solids with various geometries, including spheres, cylinders and combinations of horizontal and vertical planes. Penelope (Salvat et al., 2006) can also be used to perform the simulations of samples with an arbitrary geometry and complex structure. In addition, DTSA-II (Ritchie, 2011b; 2012) is a comprehensive software for quantifying and simulating X-ray spectra, and it is programmable on all computer platforms supporting Java.

2.2.4. EDS versus WDS

Quantitative X-ray microanalysis was initially developed based on an EPMA/WDS system, which was specifically designed for a compositional analysis (Castaing, 1951). Decades later, the development of a lithium drifted silicon [Si(Li)] detector enabled the SEM/EDS system to be used for a quantitative analysis, since then the SEM was not limited as an imaging tool (Reed & Ware, 1973). Nowadays, EDS and WDS are the most popular techniques for quantitative X-ray microanalysis.

A significant advance of the EDS over the WDS is that all the X-ray photons within the energy range from the offset to the beam energy can be collected in one measurement. The optimized design for the EDS detector window extended the detectable characteristic X-ray photon to Be Kα, which has the energy as low as 108 eV (Statham, 1984). The most recent study found that a windowless EDS detector could acquire a clear Li Kα peak (55 eV), which was considered as the detection challenge of an X-ray spectroscopy for a long time (Burgess et al., 2013; Hovington et al., 2016).

There is always one statement: EDS is inferior to WDS regarding the quantitative analytical accuracy, and one of the reasons is the poorer EDS energy resolution (Fiori et al. 1976; Newbury, 2005b; 2006; Newbury & Ritchie, 2015). The peak overlaps in the spectrum and the automatic peak identification during the acquisition limit the credibility of EDS quantification (Newbury, 2005a; 2007; 2009). However, the recent study of using the multiple linear least squares (MLLS) spectral filtering method to extract the characteristic X-ray from an SDD-collected spectrum shows that the intensity extraction accuracy of the EDS can be comparable with that of the WDS (Ritchie et al., 2012).

The condition of the specimen surface is also a critical impact factor for the quantification accuracy (Yakowitz, 1968). Since the SEM is most used as an imaging tool, the SEM specimen usually does not have a perfect flat surface. For the specimen with a complex topography, the uncontrolled geometric factors have strong impacts on X-ray emissions (as illustrated in Figure 2.5), which will further influence the quantification accuracy. The geometry of the specimen surface may cause an extra or a reduced absorption path, and those cannot be accurately recovered in the ZAF matrix correction (Newbury & Ritchie, 2013b).

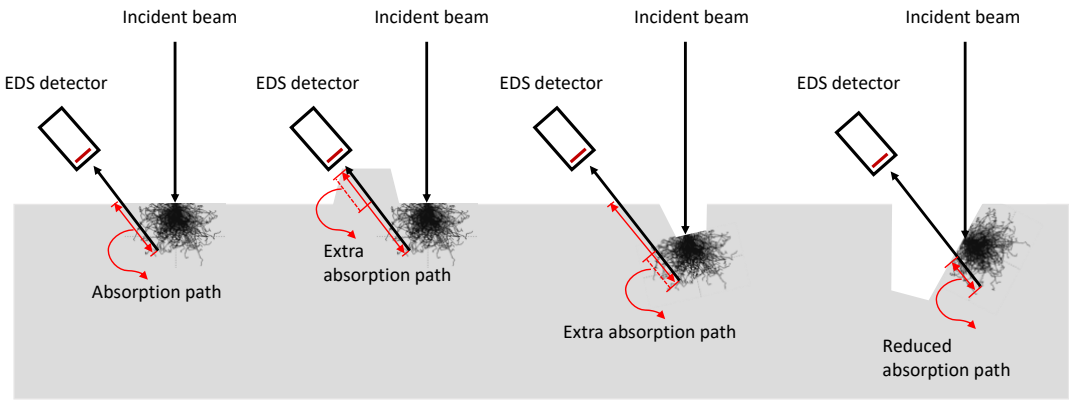

Figure 2.5 Schematic illustration of the topography effects on the X-ray absorption path length inside a specimen.

Another factor for deteriorating the EDS quantification accuracy is the extensive applications of the standardless analysis. The development of the stanardless analysis aimed to eliminate the needs of real standards and electron dose measurements. However, the quantification procedures are simplified, but the quantification accuracy is compromised (Çubukçu et al., 2008; Horny et al., 2010; Newbury et al., 1995). There are two distinct classes of standardless analysis: (1) the “first principles”, which uses theoretical calculations with physical models; and (2) the “remote standards”, which uses a library of experimental data, and now is implemented in most EDS commercial software packages (Goldstein et al., 1981). The studies of Newbury and Ritchie (2013b; 2015) show that approximately 95 % of the WDS quantification results fall within the span of ± 5 % relative error, whereas those of the “first principles" and the “remote standards” standardless quantifications are in the ranges of ± 50 % and ± 25~30 %, respectively.

However, a large number of studies show that the EDS standard-based analysis using the *k*-ratio method is able to achieve a satisfactory accuracy for both major and minor elements (Lifshin et al., 1975; Reed & Ware, 1973; Newbury & Ritchie, 2013b; 2015). Via the means of MLLS fitting and the “NIST ZAF” matrix correction (Myklebust et al., 1979) performed with the DTSA software, the accuracy and precision of the EDS quantification can be equivalent to those of the WDS (Newbury & Ritchie, 2013b; Ritchie et al., 2012).

Chapter 3

Use of an Annular Silicon Drift Detector (SDD) Versus a Conventional SDD Makes Phase Mapping a Practical Solution for Rare Earth Mineral Characterization

This chapter focuses on the X-ray mapping performed on rare earth minerals using an annular silicon drift detector (aSDD) attached to a cold field emission SEM/EDS system. The performances of the conventional and the annular SDDs are compared, and the optimal conditions for the aSDD are investigated. In order to avoid the issues of excessive noise and limited phase information occurred in the traditional elemental X-ray maps, the phase map analyses were performed.

- This chapter has been published as: Teng, C.*, Demers, H., Brodusch, N., Waters, K. & Gauvin, R. (2018). Use of an Annular Silicon Drift Detector (SDD) Versus a Conventional SDD Makes Phase Mapping a Practical Solution for Rare Earth Mineral Characterization. *Microscopy and Microanalysis* **24**(3), 238-248. doi:10.1017/S1431927618000417.

3.1 Abstract

A number of techniques for the characterization of rare earth minerals (REM) have been developed and are widely applied in the mining industry. However, most of them are limited to a global analysis due to their low spatial resolution. In this work, phase map analyses were performed on REM with an annular silicon drift detector (aSDD) attached to a field emission scanning electron microscope. The optimal conditions for the aSDD were explored, and the high-resolution phase maps generated at a low accelerating voltage identify phases at the micron scale. In comparison between an annular and a conventional SDD, the aSDD performed at optimized conditions, making the phase map a practical solution for choosing an appropriate grinding size, judging the efficiency of different separation processes, and optimizing a REM beneficiation flowsheet.

3.2 Introduction

Rare earth elements (REE), which include yttrium, scandium, and the 15 lanthanide elements, have been found in more than 250 different minerals (Jordens et al., 2013). The industrial demands for these elements keep rising due to their large-scale applications in renewable energy devices and high-technology electronic applications. Even though there is a proven global reserve of approximate one hundred million tons of rare earth oxide, only a few reserves have sufficient concentrations to constitute economic deposits (Gschneidner, 2011). The Nechalacho deposit, which is located at Thor Lake in Northwest Territories, Canada, has become one of the most important resources for rare earth minerals (REM) (Sheard et al., 2012). However, the complex mineralogy of this deposit makes the REM beneficiation flowsheet difficult to develop (Sheard et al., 2012).

In order to extract REM from the deposits, the ores first should be crushed into particles, and the grinding size is a key factor for liberation degree of the target mineral and the recovery efficiency of the following beneficiation processes. The beneficiation of REM, which includes the various separation stages and froth flotation, aims to concentrate REM from the commercially worthless minerals (Jordens et al., 2016). However, the collectors for the REM employed in the froth flotation are also selective for the iron oxide minerals, which should be removed in the separation stages before the froth flotation. The efficiency of each separation stage is significant for designing the whole beneficiation flowsheet, and a practical technique for analyzing the product from each stage is needed to provide timely information about the collection efficiency.

A number of techniques for qualitatively describing the mineralogy and quantitatively measuring minerals' chemical composition have been developed, and scanning electron

microscopy coupled with X-ray energy dispersive spectrometry (SEM/EDS) has been widely applied in the mining industry. With an SEM/EDS system and suitable software for acquiring and analyzing data, the fully automated Quantitative Evaluation of Minerals by SCANning electron microscopy (QEMSCAN) has become the most commonly used technique for mineral characterization. A full QEMSCAN system usually contains four (but up to six is possible) X-ray detectors to ensure a high collecting count rate, but its analytical spatial resolution is limited by the large probe size (Pirrie et al., 2009). Furthermore, short pulse processing time for the X-ray counts are usually applied to optimize collection efficiency, but this will result in deterioration of the energy resolution, which in turn results in difficulties in recognition on REMs.

The question then becomes, how to achieve a high analytical efficiency but still keep the spatial resolution and energy resolution at a high level? A cold field emission SEM equipped with an annular silicon drift detector (aSDD) can achieve a high count rate due to its special geometry. Contrasting with the conventional SDD (cSDD) located on the side of the chamber, the aSDD is inserted below the objective lens (Figure 3.1). This shortens the specimen-detector distance (d_{SD}) and provides a large solid angle. The solid angle is used to describe the size of the detector, which determines the count collection rate, defined by the following equation:

$$\Omega = \frac{A}{d_{SD}} \tag{3.1}$$

where Ω is to the solid angle in steradian (sr); A the collecting area of the detector (mm^2); d_{SD} the specimen-detector distance from the detector face to the beam impact point (mm) (Goldstein et al., 1981; Zaluzec, 2014). Either increasing the detector collection area or decreasing the specimen-detector distance can enlarge the solid angle, thus increasing the count rate. Figure 3.1 illustrates that the two detectors can work at the same working distance, but the d_{SD} of the cSDD is much

larger than the aSDD. Figure 3.2 shows the variations of the solid angle with the specimen-detector distance of the conventional and the annular SDDs (Demers et al., 2013). For the cSDD used in this work (detector area of 60 mm2), the minimum d_{SD} limited by the chamber geometry is 26.2 mm, giving a solid angle of 0.086 sr. However, for the aSDD, the minimized d_{SD} results in a solid angle as high as 1.35 sr at the specimen-detector distance of 1.5 mm. The large solid angle is extremely useful for the low X-ray emission specimen, enhancing the count rate and shortening the acquisition time (Kotula et al., 2008). Thus, the aSDD could improve the analytical efficiency without compromising the spatial resolution and the energy resolution.

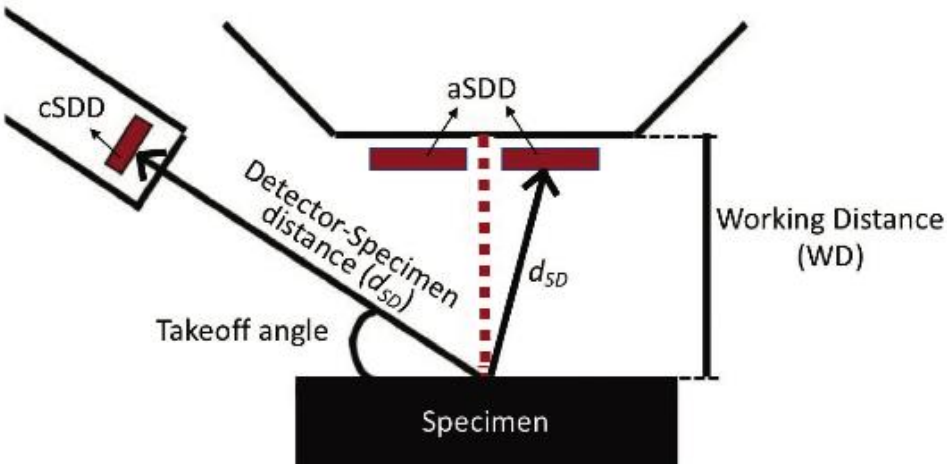

Figure 3.1 Geometrical arrangement of a conventional and an annular silicon drift detectors (SDDs).

In this work, the REM from Nechalocho deposit were characterized with the conventional and annular SDDs. Instead of the traditional elemental maps, which always have the issues of excessive noise and limited phase information, the phase map analyses were performed with the *f*-ratio method, illustrating the phase distribution directly (Horny, 2006). The optimal conditions for map acquisition on REM with the annular detector were also discussed.

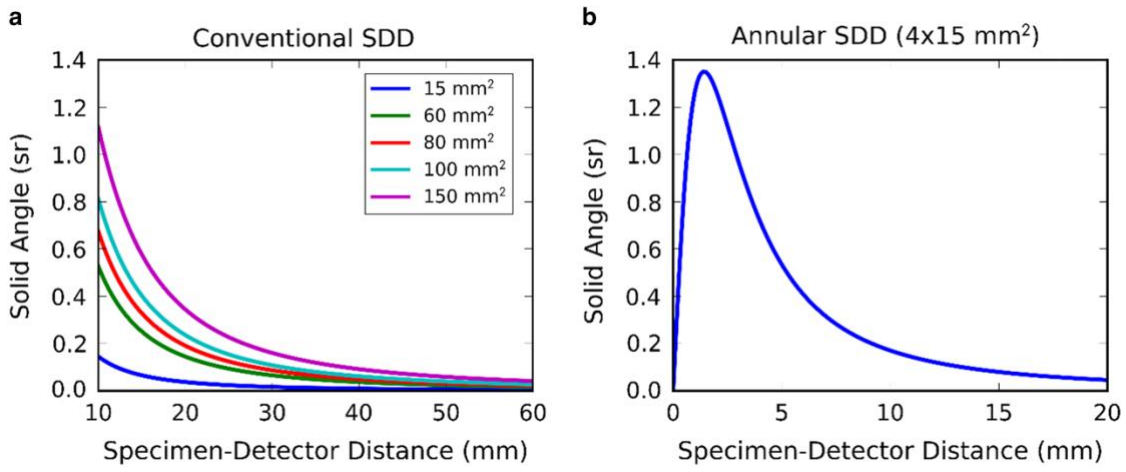

Figure 3.2 Variations of the solid angle with the specimen-detector distance for the conventional silicon drift detector (SDD) (a) and the annular SDD (b).

3.3 Materials and Experimental Methods

3.3.1 Sample preparation

The ore from the Nechalacho deposit was ground into powders and then subjected to gravity and magnetic separation processes (the flowsheet is shown in Figure 3.3) (Jordens et al., 2016). REM can be concentrated by gravity separation due to their higher densities relative to the associated gangue. In this work, a lab-scale Knelson centrifugal gravity concentrator (model KC-MD3; FLSmidth, Orillia, Ontario, Canada) was used for the gravity separation stage. The concentrate from the Knelson concentrator was subsequently fed to a lab-scale model WD (20) wet drum permanent magnetic separator (Carpco Inc., USA). There were two steps in the magnetic separation: the first step was to remove strongly ferromagnetic Fe-oxide minerals with a low-intensity magnet, labeled as Fe Magnet; the second step was to remove the remaining Fe-oxide

minerals and to concentrate strongly paramagnetic REM with a medium intensity magnet, labeled as RE Magnet (Ferron et al., 1991; Zhang & Edwards, 2013).

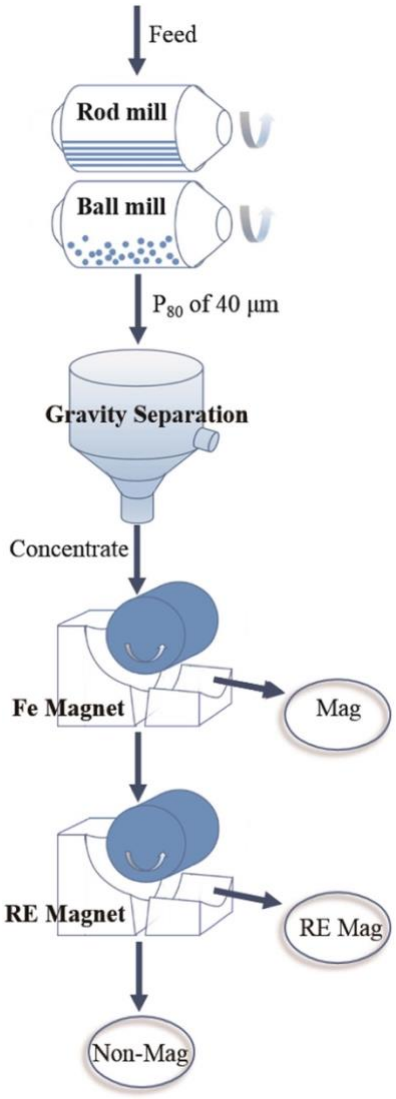

Figure 3.3 Flowsheet of main gravity and magnetic separation steps applied to the Nechalacho ores. P_{80} of 40 μm means that passing size of 80 wt % the feed is 40 μm.

One sample was taken from each magnetic separation product, labeled in Figure 3.3 as Mag, for the product selected by the first magnetic separation stage from Knelson concentrate; RE-Mag, for the product selected by the second magnetic separation stage; and Non-Mag, for the

remaining non-magnetic fraction. The three samples were then prepared for the SEM/EDS characterization. Initially, each sample was sprinkled at the bottom of a cylindrical holder, dispersed in white LR White Resin (London Resin Company Ltd, Reading, UK) and then mixed thoroughly. The holders containing the dispersed powders were cured in a vacuum oven for 48 h at a constant temperature of 60°C. After curing was complete, the samples were polished with silicon carbide papers from 100 to 1,200 grit, then polished using diamond suspensions with 1 μm grain size, and further polished using alumina suspension with a 50-nm grain size. As the samples are poor conductors, a thin (nominally 10-20 nm-thick) coating of an amorphous carbon layer was applied using an Edwards vacuum carbon coater E306 (Edwards, Crawley, UK) in order to avoid surface charging.

3.3.2 Phase map

Characterizations were performed with a Hitachi SU8230 cold field emission SEM (Hitachi High-Technologies, Rexdale, ON, Canada) equipped with a conventional XFlash® 6|60 Bruker SDD with a 60 mm^2 collection area and a Bruker Flat Quad XFlaxh® 5060F annular SDD (Bruker Nano, Berlin, Germany) with a 60-mm^2 collection area. The annular detector has special polymer windows which can absorb the backscattered electrons and only allow the X-rays to pass through. The probe current was measured with a Faraday cup mounted on the column with a NanoPico picoammeter from Hitachi (Hitachi High-Technologies). The EDS X-ray microanalysis was processed with the Bruker ESPRIT software (version 1.9) (Bruker Nano).

To obtain the phase map, the conventional EDS qualitative maps were quantified by Bruker ESPRIT software to acquire the net intensity maps, and then the *f*-ratio of each element at every pixel was calculated using the following equation:

$$f_i = \frac{I_i}{\sum_i^N I_i} \tag{3.2}$$

where I_i is the net X-ray intensity of element *i* in a N-element system from one spectrum (Horny, 2006). Using equation (3.2), the qualitative map of each element was converted to its *f*-ratio map, and a histogram of the *f*-ratio values was generated in the meantime. Then the mineral phases were manually defined by the ranges of the *f*-ratio values of the constituent elements in the histograms, and an open source Python script, pyPhaseMap (available on GitHub as pyphasemap repository), was run to convert the elemental *f*-ratio maps into a phase map. The *f*-ratios do not represent the real composition, but they are proportional to the concentrations of the corresponding elements. The adjustable *f*-ratio range is important to analyze minerals as their chemical compositions are usually not constant. The area fraction of each phase was calculated to evaluate the phase maps acquired at different conditions.

3.3.3 Analysis of count rate and energy resolution

In order to understand the impact factors on the count rate and energy resolution, the probe current and the processing time were varied during the analyses performed with the aSDD. During the acquisition, the dead time fraction (T_{DT}), the input count rate collected into the pulse processor (R_{in}), and the output count rate used for generating maps (R_{out}) were recorded. The T_{DT} given by the software is calculated by the following equation:

$$T_{DT} = \frac{R_{in} - R_{out}}{R_{in}} \quad (3.3)$$

T_{DT} and R_{in} were adjusted by changing the probe current (I_P), and this adjustment further changed R_{out}. The Bruker ESPRIT software uses the maximum pulse throughput count rate to represent the processing time, and three processing times, 60, 130, and 275 kcps were used. The smaller value means longer processing time for each pulse. The real system processing time (τ factor) was calculated by the following equation:

$$R_{out} = R_{in} e^{-R_{in}\tau} \quad (3.4)$$

As the software cannot provide an accurate input count rate at a high beam current, the real R_{in} needed to be calibrated using the following equation:

$$R_{in} = I_P \times \lim_{I_P \to 0} \frac{R_{in}}{I_P} \quad (3.5)$$

The calculation results are, 60 kcps, 1.18 μs; 130 kcps, 0.62 μs; 275 kcps, 0.29 μs, and more details are given in the Discussion section. The τ factor represents the period of time when one pulse is analyzed, and other pulses are not collected (Knoll, 2010). The longer real processing time for each pulse, the less noise and better energy resolution can be achieved in an EDS analysis. The Non-Mag sample was used for the map acquisition with the processing time of 60 and 258 kcps and the dead time fractions of 10 and 60% at 20 kV for 30 min. In addition, a standard sample (EDS-TM002), which consists of a thick layer containing C, Al, Mn, Cu, Zr, and trace amounts of Ar deposited on a silicon substrate, was also used for the systematic analyses of count rate and energy resolution (Hodoroaba et al., 2013). The analyses on the standard sample were performed at 10 kV, and the range of probe current was adjusted from 5 pA to 13.63 nA. The dead time

fraction of 60 kcps was adjusted in the range of 1-93%, and those of 130 and 258 kcps were adjusted in the range of 0-95%.

In this work, the full width at half maximum intensity (FWHM) was used to represent the energy resolution. The FWHM of La Lα, Ce Lα, Pr Lα, and Nd Lα lines were calculated in the study on REM because they are the most obvious peaks for each element in the chosen regions of interest (ROI). For the EDS-TM002 standard sample, the FWHM of the X-ray lines listed in Table 3.1 were calculated. These peaks were fitted using a Gaussian function, and the ROI background was fitted with a linear function by an open source Python script, X-ray Spectrum Analyzer (available on GitHub as xray_spectrum_analyzer). How well the peaks fit was verified visually using the residual plot and the position, width, and intensity of each peak were obtained.

Table 3.1 The analyzed X-ray lines and their respective energies of EDS-TM002 standard sample.

X-ray line	C Kα	Cu Lα	Al Kα	Zr Lα1	Zr Lβ1	Zr Lβ2	Ar Ka	Mn Kα	Mn Kβ	Cu Kα
Energy (eV)	281.77	930	1486.9	2042	2124	2201	2957	5898	6489.1	8046

3.4 Results and Discussion

3.4.1 Comparison of the phase maps acquired by the conventional and the annular SDDs

The Non-Mag sample, which is expected to have the highest fraction of REM, was used for the phase map analysis with the conventional and the annular SDDs. The secondary electron (SE) image in Figure 3.4 shows the area chosen for the map acquisition, and the phase maps of the

major phases acquired at the three current conditions listed in Table 3.2 for 5, 30, and 60 min at 20 kV are also displayed. When the aSDD is in the chamber, the backscatter electron (BSE) detector cannot be inserted due to the geometry of the annular detector. However, there is strong compositional contrast observed in the SE image, as part of the SE signal is, in fact, BSEs and they thus carry the compositional information.

Table 3.2 The current conditions applied for the map acquisitions in Figure 3.4.

Condition	Detector	Probe current (pA)	Output count rate (kcps)	Total counts		
				5 min	30 min	60 min
A	Annular SDD	280	67.6	20,688,661	116,028,510	201,809,640
B	Conventional SDD	280	2.0	579,210	3,138,044	5,742,796
C	Conventional SDD	1700	10.5	2,753,500	14,181,073	30,463,996

First, the maps were acquired with the aSDD at its optimal current condition (Condition A), which is commonly used to acquire X-ray maps. Then the same probe current was used with the cSDD (Condition B). After that, the cSDD was used at its optimal current condition (Condition C) by increasing the probe current while holding the other parameters constant. This enabled the performances of the two detectors at the same current conditions and their own optimal conditions were compared. As shown in Table 3.2, the count rate for generating X-ray maps with the aSDD can reach as high as 67.6 kcps with the probe current of 280 pA, whereas that of the cSDD is only 2.0 kcps. The high count rate contributes to the clear phase map acquired with the aSDD in 30 min.

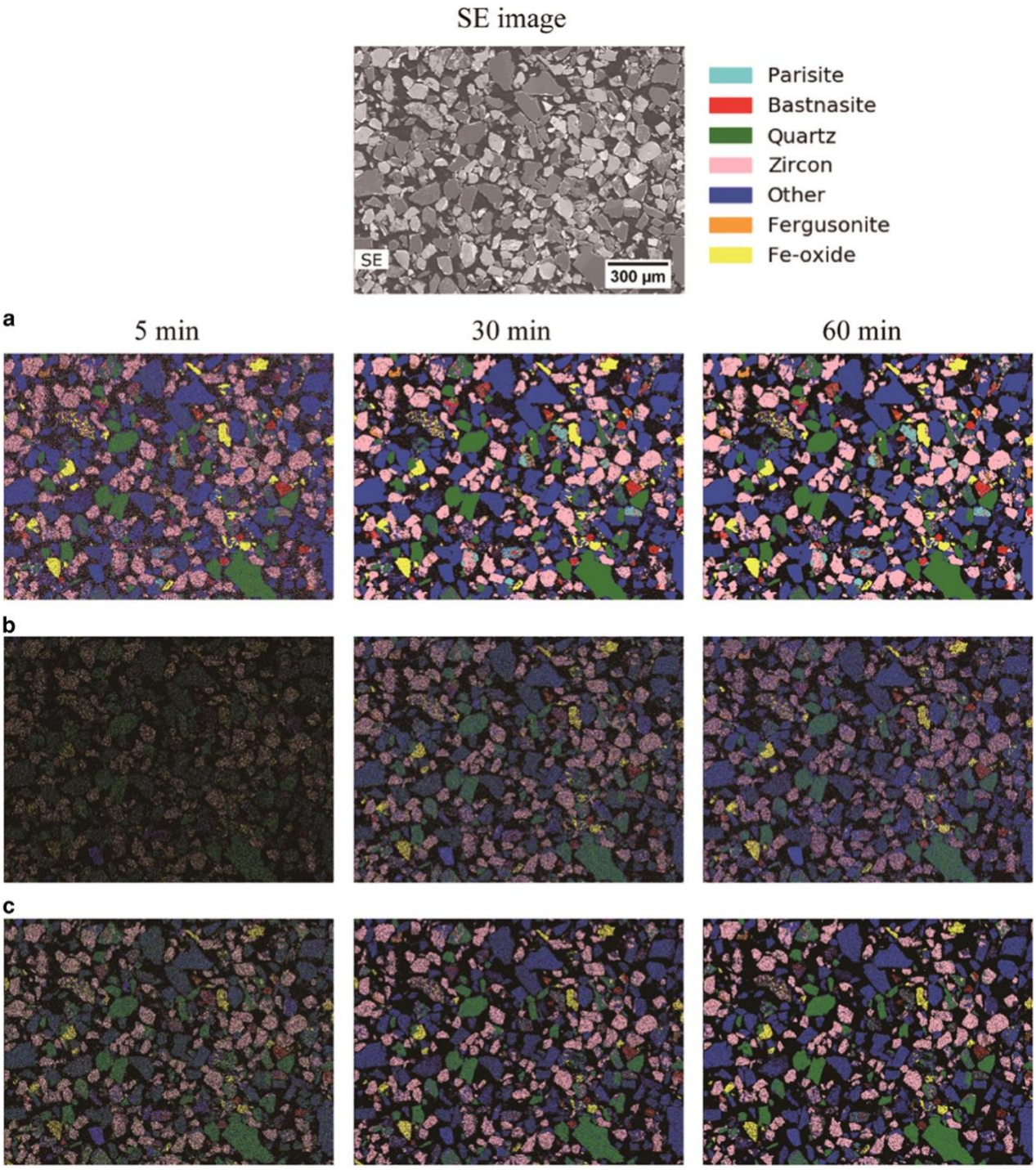

Figure 3.4 Phase maps of the Non-Mag sample acquired at the three conditions listed in Table 3.2 for 5, 30, and 60 min at an accelerating voltage of 20 kV. The working distances for the two detectors were both 15 mm.

Figure 3.5 shows the pixel fraction of each phase in the maps displayed in Figure 3.4. Since the powders were mounted in an epoxy resin, which is not shown in the maps, so the total fraction of all the phase does not equal one. In terms of phase identification, the number of counts determines whether the elemental peak can be detected, and only the statistically significant peaks can be considered for identification. The raised collecting count rate and extended acquisition time both can increase the number of counts. Thus, the significantly higher number of collected counts ensure that more pixels are identified at condition A than B or C. However, the maps acquired with the aSDD for 30 and 60 min are almost the same, indicating that one hundred million counts collected within 30 min are already sufficient to identify all the major phases.

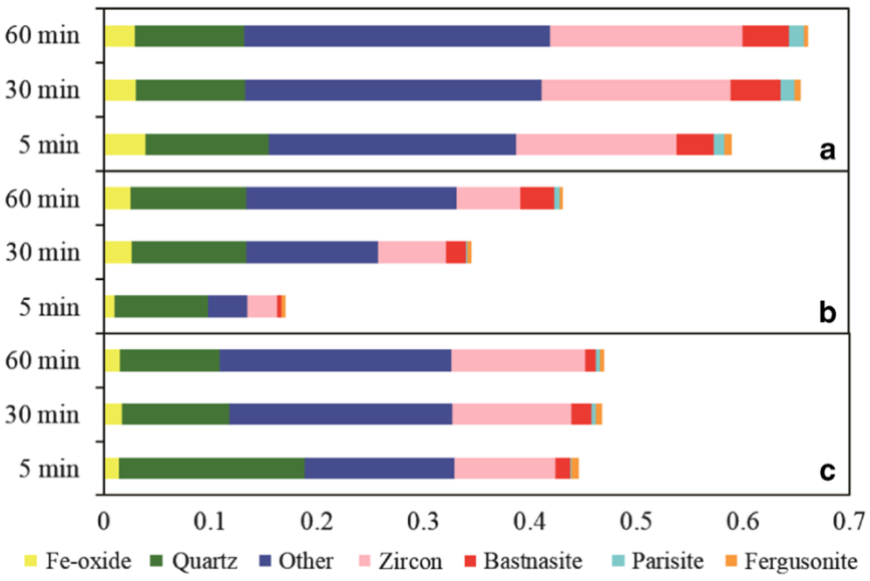

Figure 3.5 The area fraction of each phase shown in Figure 3.4.

Three REM were found in this area: bastnäsite [$(Ce,La,Y)F(CO)_3$], parisite [$Ca(Ce,La)_2(CO_3)_3F_2$], and fergusonite ($REENbO_4$), which are regarded as the main rare earth carriers in the Nechalacho deposit (Sheard et al., 2012). Bastnäsite and parisite are both rare earth carbonates, but parisite contains approximately 7% calcium, and calcium is the only element that

can be used to differentiate them, with the aSDD being better at identifying each phase. The improved signal-to-noise ratio of the spectrum, which results from the high count rate can decrease the detection limit. The difficulty of the analyses on REE is mainly due to the low X-ray intensities, and the common solution is to lengthen the acquisition time. However, the high count rate of the aSDD can solve this problem without sacrificing the analytical efficiency.

The phase map can also be used to optimize a REM separation flowsheet. Figure 3.6 shows the phase maps of the Mag, the RE-Mag, and the Non-Mag samples acquired with the annular and the conventional SDDs at their optimal conditions. All the maps were acquired at 20 kV for 60 min. Figure 3.7 displays the area fraction of each phase in all the identified phases, statistically illustrating the changes of the phases through the separation stages. The proportion of REM and zircon phases increases and the proportion of Fe-oxide phases greatly decreases after the two magnetic separation stages. However, there are still Fe-bearing minerals remaining in the Non-Mag sample, so more magnetic separation processes are required to further remove them.

The aSDD is proven to be an efficient instrument for map acquisition, and the maps of the products from different separation stages can assist in the design and optimization of a REM separation flowsheet. In this section, the analyses were performed at low magnification in order to observe the major phases. However, a phase identification at the micron scale requires detailed analysis with a high spatial resolution. The high count rate of the aSDD allows the use of lower accelerating voltage, which can result in an improved spatial resolution.

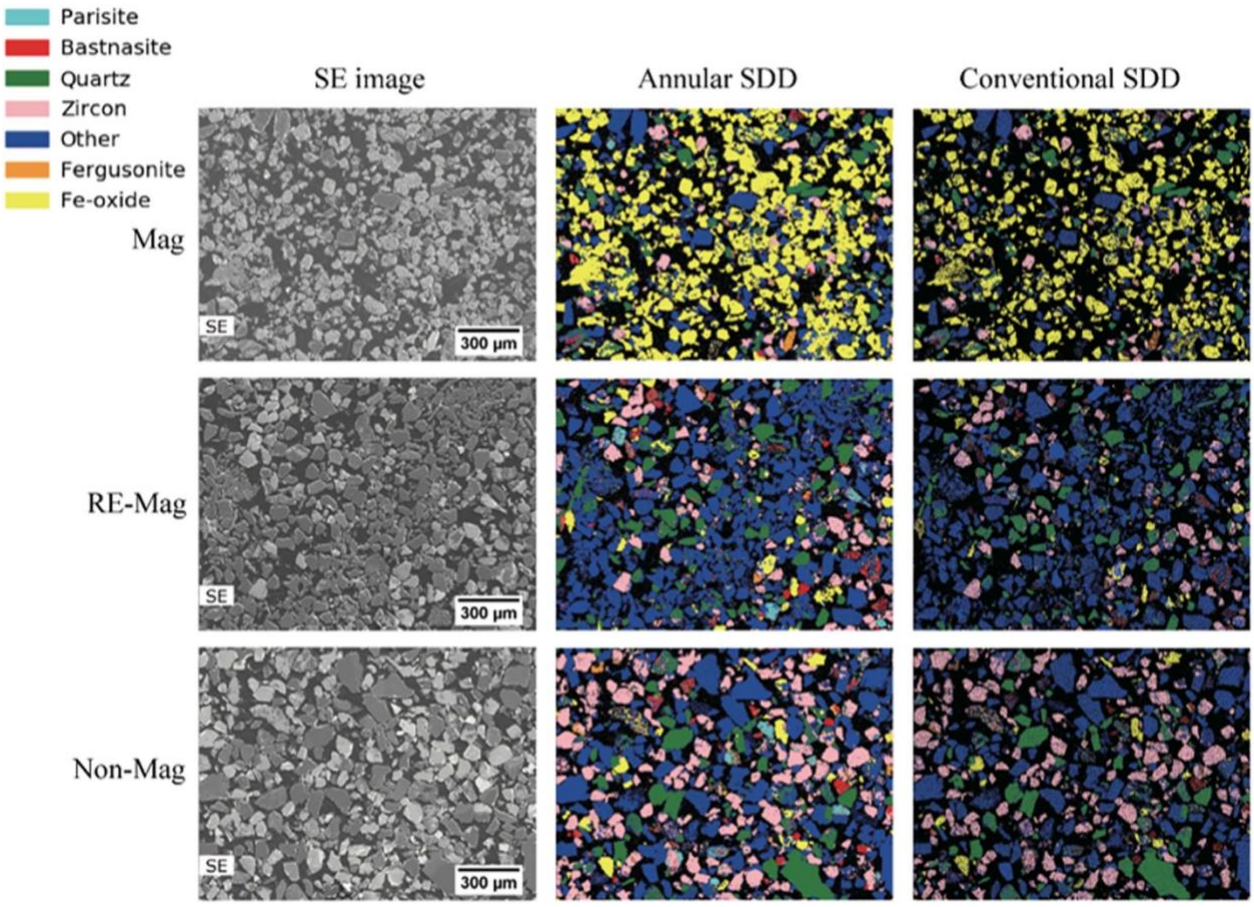

Figure 3.6 Phase maps of the Mag, the RE-Mag and the Non-Mag samples acquired with the annular and conventional silicon drift detectors (SDD) at their optimal conditions with an accelerating voltage of 20 kV and an acquisition time of 60 min.

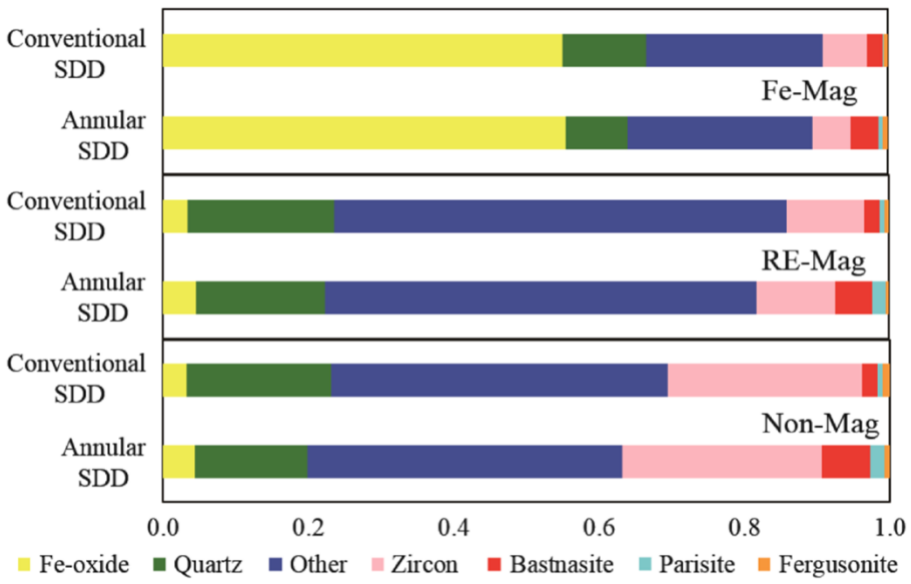

Figure 3.7 The area fraction of each phase in relation to all of the identified phases shown in Figure 3.6. SDD, silicon drift detector.

3.4.2 The application of the annular SDD at a low accelerating voltage

A beam energy of 20 kV is commonly used in order to get a required overvoltage for the analyzed peaks and collect sufficient X-ray counts. In order to make the most of the high count rate of the annular detector, the phases analyses were performed at lower beam energy, aiming to achieve a high spatial resolution. Figure 3.8 displays the maps of fergusonite, zircon, and the overlaps of the two phases at the accelerating voltages of 20, 10, and 5 kV, which visually illustrate the impacts of the beam energy on the spatial resolution of the X-ray microanalysis. Even though the beam broadening effect, which is driven by the accelerating voltage, will have an impact on the analytical resolution, its contribution can be ignored in a field emission SEM which normally has a source size smaller than 5 nm. Table 3.3 lists the acquisition conditions for the maps displayed in Figure 3.8.

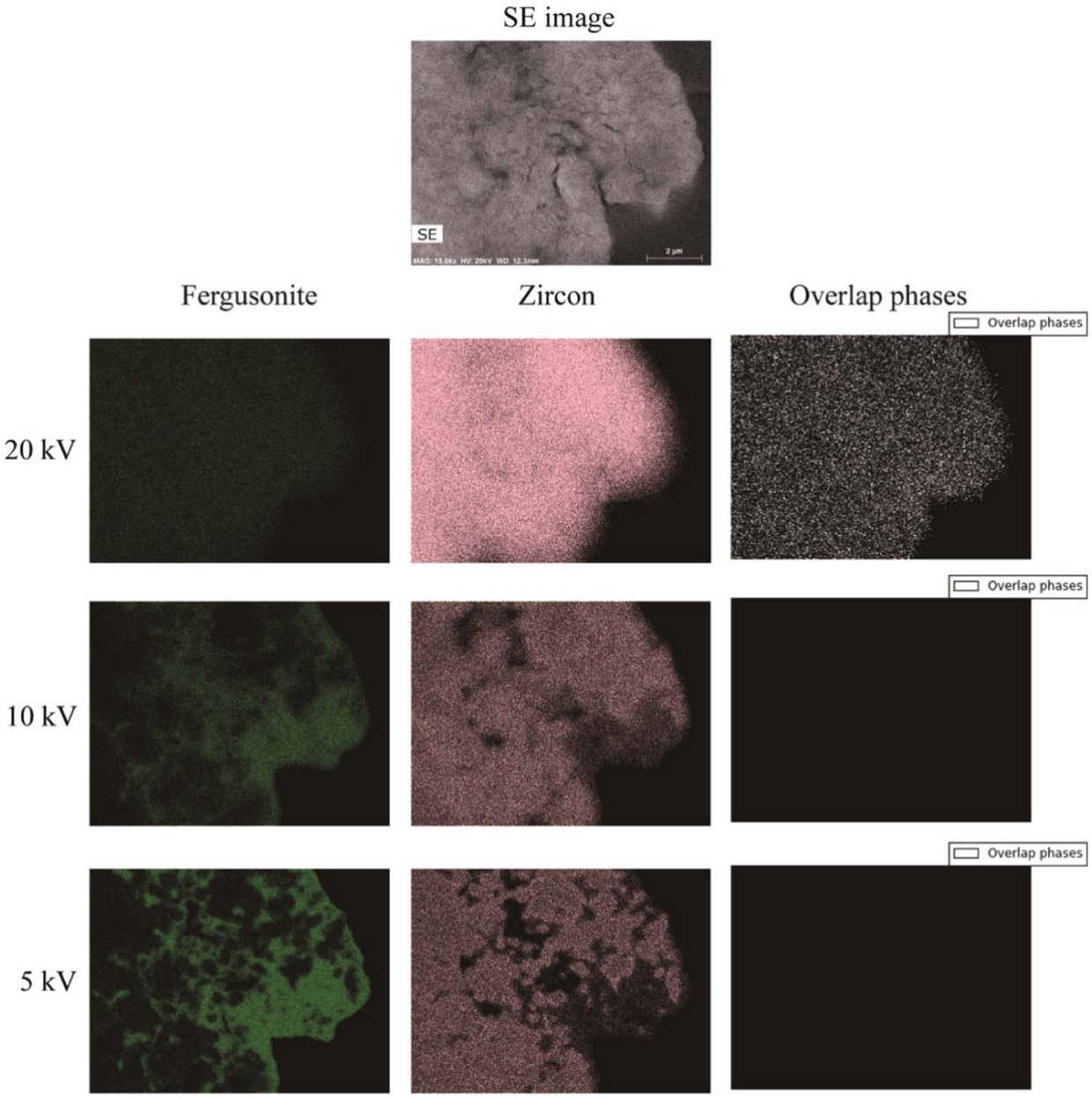

Figure 3.8 Phase maps of the fergusonite and the zircon phases acquired with the secondary electron (SE) image was acquired at 20 kV.

Table 3.3 Acquisition conditions for the maps displayed in Figure 3.8.

Beam energy (kV)	Beam current (nA)	Acquisition time (min)
20	0.42	20
10	1.87	20
5	0.98	30

Fergusonite often occurs in this case with zircon, which is also considered to be a major rare earth carrier in this deposit (Sheard et al., 2012). With the decrease of the accelerating voltage, the improved spatial resolution makes the edges of each phase much clearer. At 20 kV, a completely bright phase is observed, meaning that this phase was identified as both fergusonite and zircon. However, at 10 and 5 kV, overlapped phases are observed, indicating that the two phases were completely differentiated. The high spatial resolution analysis shows that there are no REE existing in the zircon phase.

In order to maximize the characteristic X-ray counts, the accelerating voltage (E_0) should exceed the critical ionization energies (E_C) of the analyzed X-ray lines by overvoltage ($U = E_0/E_C$) of 2 to 3 (Goldstein et al., 1981). In the fergusonite and zircon phases, Y and Zr are the main elements, and the E_C of their Lα lines are 2.080 and 2.222 keV, so 5 kV is still appropriate to analyze them. However, the E_C of other REE L-lines are in the range of 5.4-9.3 keV (E_C of La Lα is 5.483 keV and E_C of Lu Lα is 9.244 keV). Thus, the accelerating voltage should be selected based on the X-ray lines to be analyzed.

Although the REE M-lines have lower excitation energies, the serious overlaps limit their use. In addition to the overlaps between different REE, the interferences with other light elements also generate problems in identification. For example, the energy of Dy Mα line is 1.293 keV, and that of Mg Kα line is 1.254 keV, but both of the two elements were found in this ore, and the two lines cannot be separated in an EDS spectrum. Besides the issue of serious overlaps, the EDS analysis on low energy X-ray lines (below 1 keV) is still problematic. The strong absorption from the specimen and the low primary fluorescence yield make the detection limit for REE M-lines

much lower than their L-lines. Thus, L-lines are always preferred for the analyses on REM, even they require relatively high beam energy.

The overvoltage of 2 to 3 is a compromise between the peak/background ratio and the spatial resolution. Table 3.4 lists the generation, and emission ranges of the analyzed X-ray lines in fergusonite and zircon phases at the accelerating voltages of 5, 10, and 20 kV. The X-ray generation range (X_G) was calculated by Anderson & Hasler (1966), and the real X-ray emission range (X_E) was modified by the Gauvin model (2007) to allow for the absorption effect. The calculation results in Table 3.4 indicate that the distinguishable features in fergusonite and zircon phases are below 0.2 μm at 5 kV, around 0.5 μm at 10 kV, and beyond 1 μm at 20 kV, which are consistent with the observations in Figure 3.8. As shown in Figure 3.8, the features with a size of around 0.5 μm can be observed at 10kV, but smaller features can only be observed at 5 kV.

Table 3.4 The generation ranges and emission ranges of the analyzed X-ray lines in fergusonite and zircon phases at the accelerating voltages of 5, 10 and 20 kV.

Phase	Element and X-ray line		$\boldsymbol{X_G}$ (μm)			$\boldsymbol{X_E}$ (μm)		
			E_0 = 5 keV	E_0 = 10 keV	E_0 = 20 keV	E_0 = 5 keV	E_0 = 10 keV	E_0 = 20 keV
Fergusonite	Y	Lα	0.135	0.552	1.889	0.129	0.462	1.070
	Nb	Lα	0.122	0.539	1.876	0.118	0.472	1.209
	O	Kα	0.185	0.602	1.939	0.160	0.388	0.601
Zircon	Zr	Lα	0.140	0.593	2.045	0.135	0.511	1.265
	Si	Kα	0.167	0.620	2.073	0.164	0.583	1.684
	O	Kα	0.201	0.654	2.106	0.174	0.423	0.659

Another important use of the phase map is to observe single particles, with the aim of analyzing the liberation degree of the target minerals. Before any separation can be undertaken, the ore must be crushed and ground into the size required to liberate the valuable minerals at the coarsest particle size (Wills & Finch, 2015). It is critical to choose an appropriate grinding size,

which can establish an effective and efficient beneficiation process to avoid energy waste in over crushing or grinding and make the subsequent separation stages easier and cheaper to operate.

Figure 3.9 shows the phase maps of the liberated, the mid-liberated, and the unliberated target REM particles, aiding the choice of an appropriate grinding size. The maps were acquired at 10 kV for 1 h, and all phases are labeled. An accelerating voltage of 10 kV was chosen as a compromise between the required spatial resolution and the preference of using REE L-lines. Figures 3.9(a) and 3.9(b) display the partially liberated particles with the size of +60 μm. Figure 3.9(c) shows a wholly liberated rare earth particle with the size of around 40 μm, but K-Feldspar and Fe-oxide are observed inside, the non-REM impurities will decrease the grade of the final concentrate, having an impact on the economics of the process.

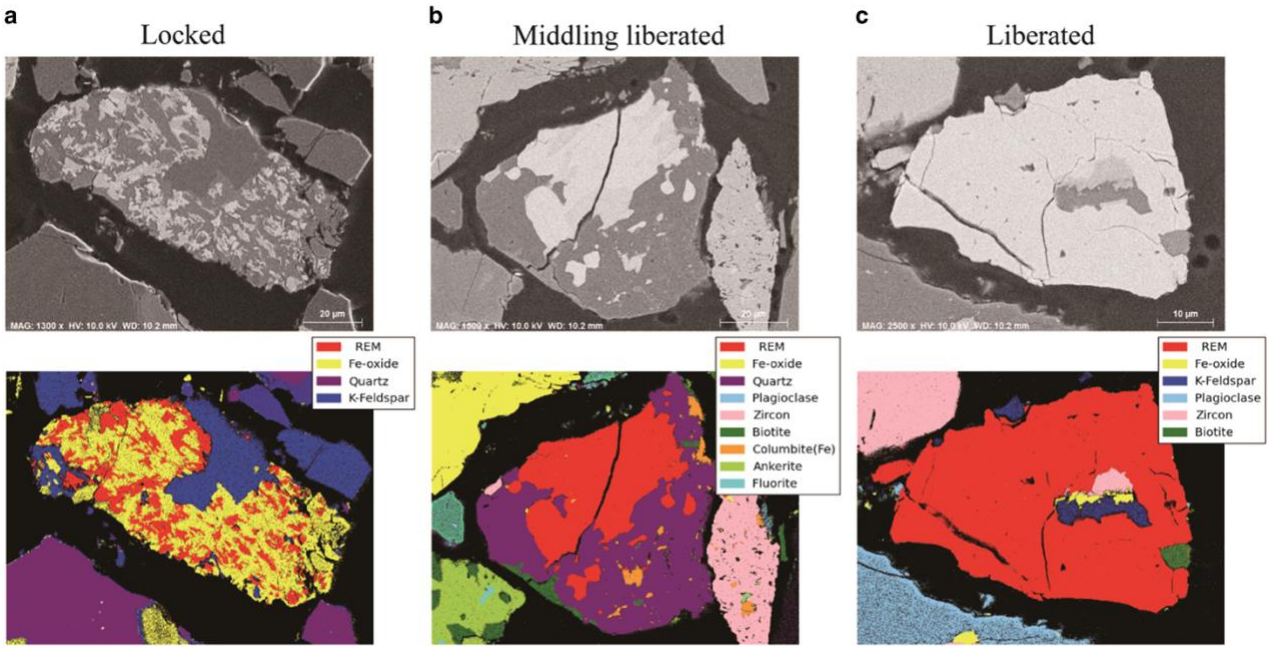

Figure 3.9 Phase maps of the liberated, the mid-liberated, and the unliberated rare earth minerals acquired with the annular silicon drift detector at an accelerating voltage of 10 kV for 1 h. (a) Locked rare earth minerals (REM) particle; (b) middling liberated REM particle; and (c) liberated REM particle.

Except for the liberation degree, the particle size also has an effect on recovery efficiency. It has been reported that the standard ideal particle size range for the subsequent flotation is of the order of 10 - 100 μm (Rahman et al., 2012). Fine particles can produce a high liberation degree, but exhibit a low efficiency of collision with the bubbles, which decreases the flotation efficiency. All these factors should be considered when choosing the grinding size. The high-resolution phase map can provide timely information on the mineral liberation, helping to identify an appropriate grinding size.

3.4.3 Count rate and energy resolution with the annular SDD

The aSDD has the advantage of a high collecting count rate, this allows the acquisition of high-quality maps at a low accelerating voltage within a short acquisition time. In order to make full use of this, the best acquisition condition of aSDD is explored in this section. In addition to the count rate, which determines whether the collected counts are sufficient for an accurate quantification within a limited time, the energy resolution, which directly affects the peak overlaps in a spectrum, is another important factor for elemental analysis and phase identification. This is especially important for REE as, due to the serious overlaps of their L-lines and M-lines, a high energy resolution is required to distinguish them, and a large number of counts is required by an accurate deconvolution on the overlapped peaks. Thus, in this work, the probe current and the processing time were adjusted to explore the impacts of count rate and energy resolution on the phase map.

In this section, the Non-Mag sample was used for the map acquisition at four conditions labeled A through D in Table 3.5. As discussed in the previous sections, the aSDD has a large solid angle, which allows for a higher collecting count rate than the cSDD. However, not all the collected counts can be analyzed, and the R_{out} represents the real count rate used to generate the X-ray maps. Figure 3.10 displays the phase maps acquired under the corresponding conditions, and the area fraction of each phase.

Table 3.5 Four conditions used to acquire the phase maps displayed in Figure 3.10 with the annular silicon drift detector.

Condition	Processing time, τ	Probe current, $\boldsymbol{I_P}$ (pA)	Dead time fraction, $\boldsymbol{T_{DT}}$	Input count rate, $\boldsymbol{R_{in}}$ (kcps)	Output count rate, $\boldsymbol{R_{out}}$ (kcps)
A	60 kcps	105	10%	74.1	66.2
B	60 kcps	920	60%	599.5	221.9
C	275 kcps	390	10%	241.4	218.8
D	275 kcps	4370	60%	2880.7	1003.8

Compared with the other three conditions, condition A has a relatively lower R_{out}, so the map is noisier and fewer pixels were identified. However, the total counts used to generate maps should be estimated with R_{out} and T_{DT} together. For example, conditions B and C have similar R_{out}, but they have different live time for collecting counts. Although the three conditions B, C, and D have different R_{out} and T_{DT}, the phase maps, as well as the area fraction of each phase, are very similar. This again indicates that as long as the required counts for phase identification are collected, the extra counts do not further improve the maps.

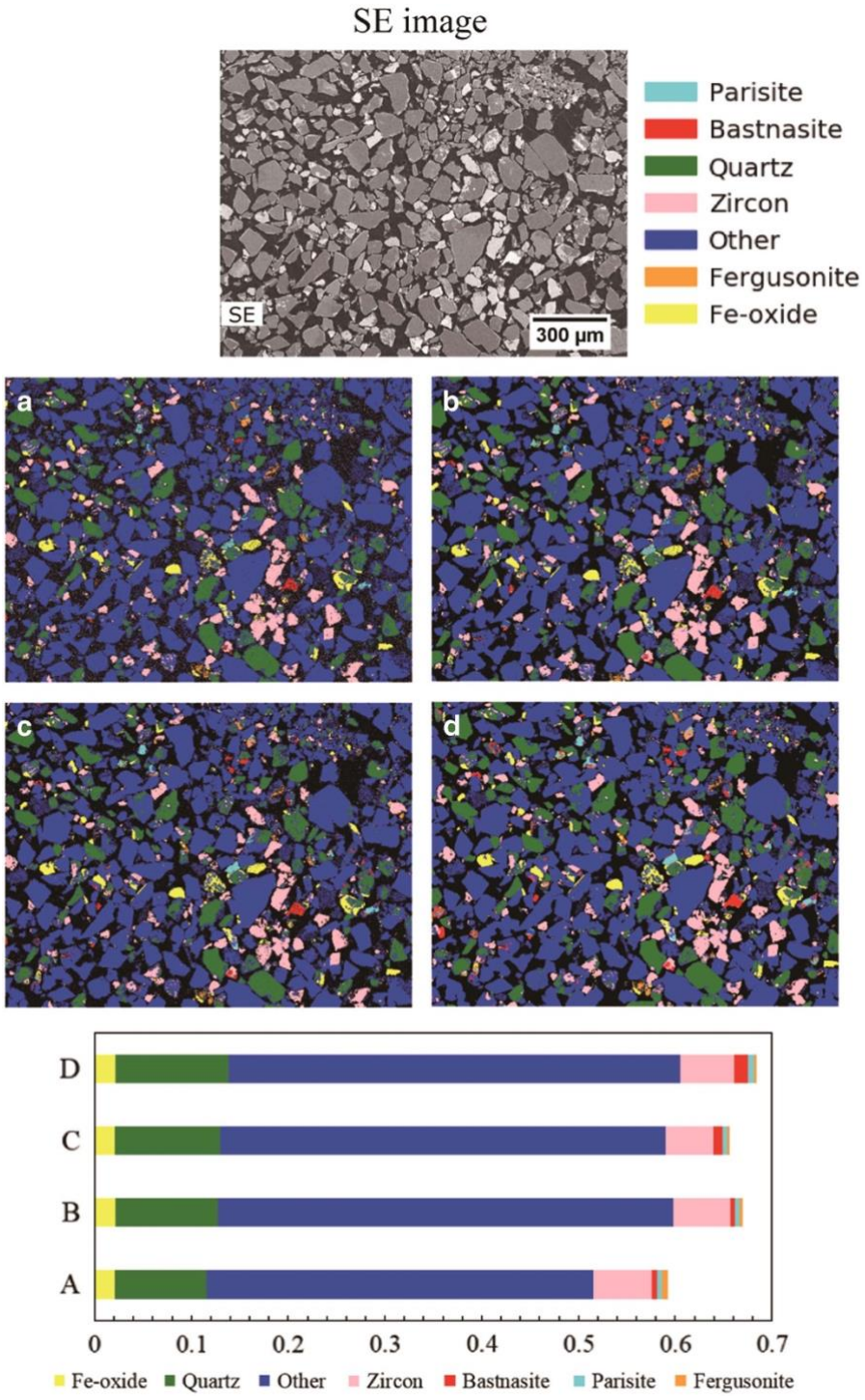

Figure 3.10 Secondary electron (SE) image and (a-d) phase maps acquired at A-D conditions listed in Table 3.5 with the annular silicon drift detector at an accelerating voltage of 20 kV for 30 min. The area fraction of each phase is also displayed.

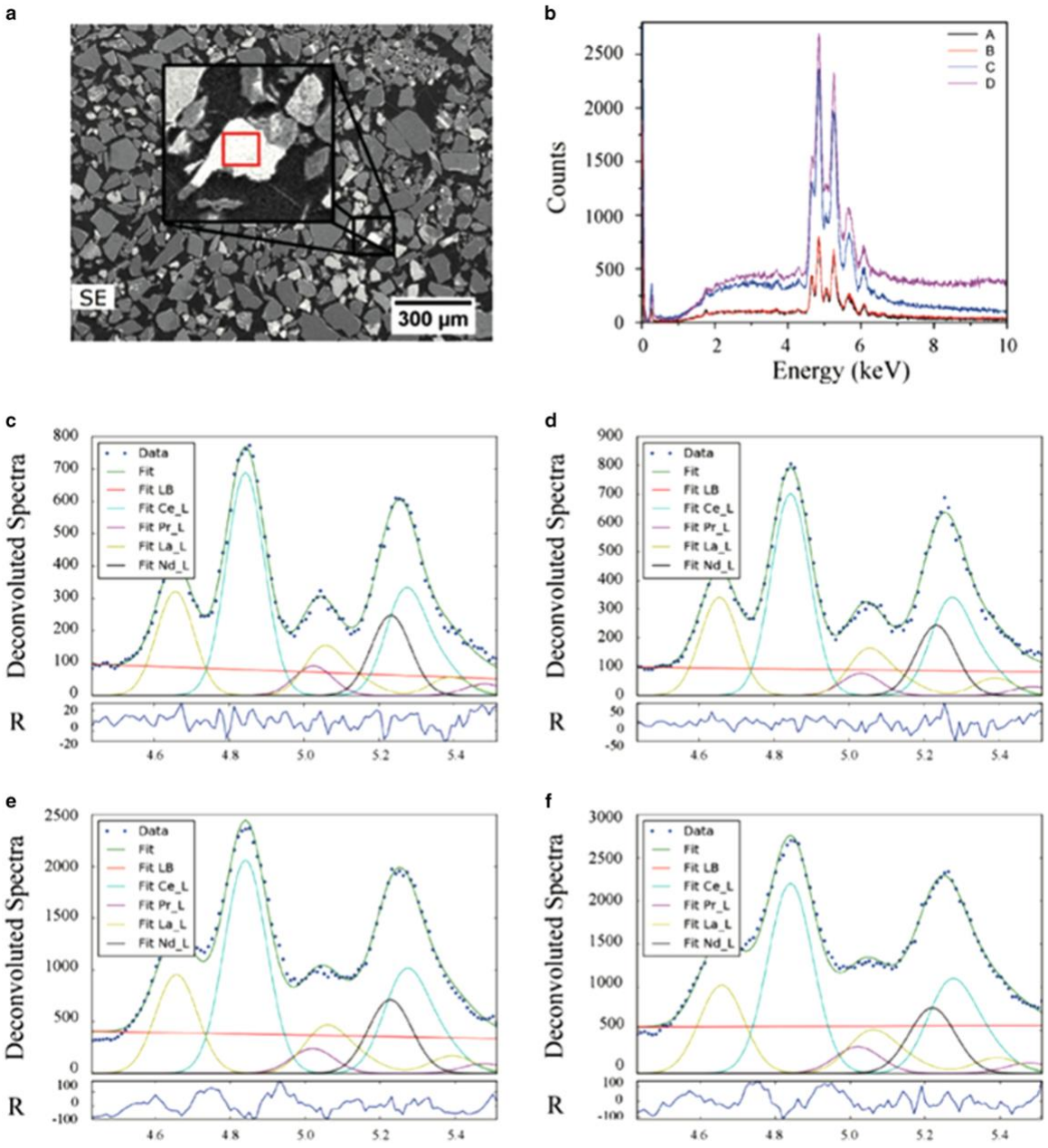

Figure 3.11 Spectra acquired at the four conditions listed in Table 3.5 in the selected area [red square in (a)]. (a) Secondary electron (SE) image; (b) sum spectra in the selected area in (a); (c)-(f) the deconvoluted spectra of rare earth elements. The residual (R) of the fit is also displayed.

Energy resolution also has an important impact on phase identification. Area spectra were extracted from the rare earth phase marked in the red frame in Figure 3.11(a), and the spectra are displayed in Figure 3.11(b). Conditions C and D collected many more counts, not only for the REE

peaks, but also for the backgrounds. The spectra visually indicate that the total counts used to generate maps at conditions B and C are different. Since these REE have similar atomic numbers, serious overlaps of their L-lines are observed in the area spectra. The deconvolution results are shown in Figures 3.11(c) - 3.11(f), and the FWHM of La Lα, Ce Lα, Pr Lα, and Nd Lα are listed in Table 3.6. For the ease of viewing, not all the X-ray lines within this energy range are displayed. As shown in Table 3.6, except for the decrease of the pulse processing time, the increase of T_{DT} will also degrade the energy resolution.

Table 3.6 Energy resolution of REE peaks (La Lα, Ce Lα, Pr Lα and Nd Lα lines) displayed in Figure 3.10 at the corresponding conditions A through D.

Condition	Processing time	FWHM (eV)			
		La Lα1	Ce Lα1	Pr Lα1	Nd Lα1
A	60 kcps	116.1	118.1	120.2	122.2
B	60 kcps	118.2	120.2	122.2	124.2
C	275 kcps	129.8	131.6	133.4	135.3
D	275 kcps	138.9	140.6	142.4	144.1

As discussed above, R_{out} is influenced by the probe current and the processing time, and the energy resolution is mainly influenced by the processing time. In order to systematically explore the relationships between these factors, a standard sample (EDS-TM002) was used to measure T_{DT}, R_{in}, and R_{out} with changing I_P and τ. Figure 3.12(a) illustrates the experimental relationship between the R_{out} and the R_{in} with the processing time of 275, 130 and 60 kcps, and their fitting curves, such that the τ factors in equation (3.4) were calculated: 60 kcps, 1.18 μs; 130 kcps, 0.62 μs; 258 kcps, 0.29 μs. According to equation (3.4), the maximum value of R_{out} will be 43% R_{in}, which occurs when R_{in} equals $1/\tau$. Figure 3.12(b) illustrates the relationship between R_{out} and T_{DT}, which is consistent with the expectation that the maximum R_{out} will occur when T_{DT} equals to 5%, as deduced from equations (3.3) and (3.4).

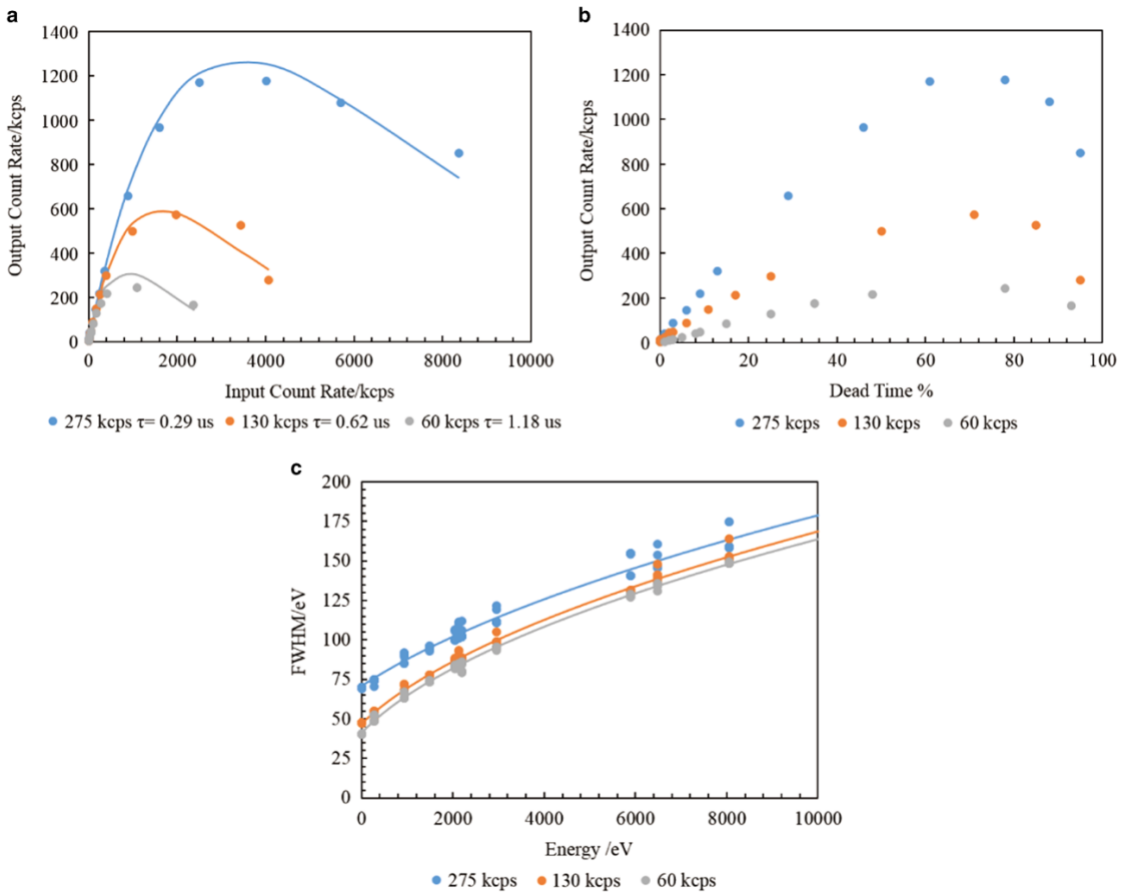

Figure 3.12 The relationships between dead time fraction, input count rate, output count rate, and energy resolution measured with the standard sample EDS-TM002. An accelerating voltage of 10 kV was used and the range of probe current was adjusted between 5 pA to 13.63 nA. FWHM, full width at half maximum intensity.

Even though short processing time can produce a high count rate, the energy resolution, which is proportional to the X-ray line energy and the electronic noise, is largely compromised. The long processing time can effectively decrease the electronic noise. Figure 3.12(c) illustrates the FWHM of the X-ray lines listed in Table 3.1 with the three processing times, and their fitting curves. Only points with a dead time fraction below 10% are shown in this figure. The experimental and calculated results show that FWHM increases with higher line energy and a shorter processing time.

Regarding the analysis on REE, all the REE L-lines have an energy higher than 4keV with several subshell lines, so a high energy resolution and a long processing time are preferred. However, considering the analytical efficiency, the processing time should be chosen according to the applications. For example, when the phase map is performed at a low magnification to evaluate the REM beneficiation efficiency, differentiating REE is not necessary, so a relatively short processing time can be used to obtain a quick map acquisition. That is why the maps acquired at the four conditions in Figure 3.10 are all acceptable. However, a high energy resolution is necessary for quantitative analysis. For example, bastnäsite can be subdivided to bastnäsite-(Ce) and bastnäsite-(La) depending on the ratio of the constituted Ce and La concentrations, so the differentiation between them requires a high energy resolution to accurately measure the intensity of each rare earth element.

3.5 Conclusion

In comparisons between an annular and a conventional SDDs, the aSDD, performing at optimized conditions makes the phase map a practical solution for characterizing REM. The high count rate of the aSDD, which benefits from its larger solid angle compared with the cSDD, contributes to a high signal-to-noise ratio of EDS maps in short acquisition time, even with low beam energy. The high-resolution phase map generated at a low accelerating voltage is helpful to identify phases at the micron scale. Regarding applications, the phase map can assist to choose an

appropriate grinding size, to judge the efficiency of separation processes, and to optimize a REM beneficiation flowsheet.

In order to make full use of the advantage of high count rate, the optimal condition for map acquisition with the aSDD was explored. In terms of the phase map acquisition on REM, the processing time should be chosen depending on the applications. On the one hand, when only the general phase information is required, a relatively shorter processing time can be used to obtain a quick map acquisition; on the other hand, when different REE need to be differentiated, and the intensity of each element is required to be accurately measured, a long processing time is necessary to improve the energy resolution for a more accurate peak identification.

Chapter 4

Multivariate Statistical Analysis on SEM/EDS Phase Map of Rare Earth Minerals

In Chapter 3, the phase map analyses using an aSDD were performed on rare earth minerals, and the large solid angle of the aSDD enables EDS mapping with a high collecting count rate. In this chapter, the data processing methods based on the multivariate statistical analysis were applied to the phase maps to further improve the mapping analytical efficiency.

- This chapter has been submitted as: Teng, C.* & Gauvin, R. Multivariate Statistical Analysis on an SEM/EDS Phase Map of Rare Earth Minerals. *Scanning* (in press).

4.1 Abstract

The scanning electron microscope/energy dispersive spectroscopy (SEM/EDS) system is widely applied to rare earth minerals (REMs) to qualitatively describe their mineralogy and quantitatively determine their composition. The performance of multivariate statistical analysis on the EDS raw dataset can enhance the efficiency and the accuracy of phase identification. In this work, the principal components analysis (PCA) and the blind source separation (BSS) algorithms were performed on an EDS map of a REM sample, aiming to achieve an efficient phase map analysis. The PCA significantly denoised the phase map, and was used as a preprocessing step for the following BSS. The BSS separated the mixed EDS signals into a set of physically interpretable components, bringing convenience to the phase separation and identification. Through the comparison between the independent component analysis (ICA) and the non-negative matrix factorization (NMF) algorithms, the NMF was confirmed to be more suitable for EDS mapping.

4.2 Introduction

Industrial demands for rare earth elements (REEs) keep rising as a result of their increasing application in high-technology electronic devices. As sources of these elements, the rare earth minerals (REMs) and their bearing ores are required to be characterized with more efficient techniques to weigh the REEs concentrations. The most popular characterization system is the scanning electron microscope coupled with the X-ray energy dispersive spectroscopy (SEM/EDS) due to its fast and easy operation. The annular silicon drift detector (aSDD), which enhances the count rate and spatial resolution of phase mapping, can achieve a more efficient EDS analysis (Teng et al., 2018). However, the small proportion of REMs in the ores and the low concentration of REEs in the REMs may cause the problem of insufficient X-ray intensities for distinct peaks in the sum spectrum, resulting in omissions of rare earth phases in an EDS mapping analysis. To settle this issue, the simplest way is to extend the acquisition time to overwhelm the spectrum background, but the trade-off is the analytical efficiency.

This study investigates an alternative method, which applies the multivariate statistical analysis (MSA) on a map dataset to extract REEs intensities, and thus effectively shortens the data acquisition time. The MSA treats an EDS map as a set of spectral images (SIs) which encompass the spectrum at each pixel to reduce the dataset redundancy, and then distinguishes the spectra for similarities and differences without predetermining elements (Bosman et al., 2006). Through combining similar SIs, the original dataset is decomposed into a limited number of components to capture the major information. In this way, the phases with different chemical constituents can be distinguished without any biased expectation, providing preliminary knowledge for further quantitative analyses (Kotula et al., 2003; 2012).

The principal component analysis (PCA) is the most widely used algorithm among various MSA methods, which creates a set of orthogonal variables and orders them as decreasing variations (Wold et al., 1987, Trebbia & Bonnet, 1990, Parish & Brewer, 2010). Its most popular applications for X-ray microanalysis are dimensionality reduction and noise subtraction through maintaining the leading components with higher variances and discarding the rest as noise. It has been applied to EDS spectra to remove background counts and extract characteristic X-ray intensities, which shortened the necessary acquisition time (Saghi et al., 2016). It was also used to directly distinguish particles with different chemical compositions or morphologies in an EDS map (Genga et al., 2012). However, the orthogonal constraint followed by the PCA neglects any physical consideration, which may cause difficulties in interpreting the decomposed components.

As an alternative to avoid this limitation, the blind source separation (BSS) unmixes the original dataset into a set of statistically independent components to directly capture the essential data structure (de la Peña, et al., 2011). Among the various BSS algorithms, the two most commonly applied to X-ray microanalysis are the independent component analysis (ICA) and the non-negative matrix factorization (NMF), which both consider each decomposed component as a typical event occurring between the electron beam and the specimen (Cardoso, 1998; Lee & Seung, 1999, Hyvärinen & Oja, 2000). The main difference between the two algorithms is that the NMF only allows additive combinations and prevents subtractions to force all components to be non-negative, but the ICA allows both combinations and subtractions (Wu et al., 2010, Jany et al., 2017). Even though the BSS can be performed independently, it usually requires the PCA as a preliminary step to make the original dataset less correlated and decide the ummixed dimension (Jany et al., 2017). There are more and more studies using the combination of PCA and BSS to

distinguish different phases instead of the traditional elemental identification method (Rossouw et al., 2015b; 2016).

In this study, the PCA and BSS algorithms were performed on an EDS map dataset acquired on a REMs sample for only 5 minutes, aiming to achieve an efficient phase analysis and find the optimal data processing procedure.

4.3 Materials and Experimental Methods

4.3.1 Sample

The ore powders from the Nechalacho deposit (Thor Lake in Northwest Territories, Canada) were sprinkled at the bottom of a cylindrical holder, dispersed in white LR White Resin (London Resin Company Ltd, Reading, England) and then mixed thoroughly. The holder containing the dispersed powder was cured in a vacuum oven for 48 hours at a constant temperature of 60℃. After curing was complete, the sample was polished with silicon carbide papers, followed by diamond suspensions of 1 µm grain size (Buehler, Lake Bluff, IL, USA) and alumina suspension of 50 nm grain size (Buehler). As the sample is a poor conductor, a thin (nominally 10-20 nm-thick) coating of an amorphous carbon layer was applied using an Edwards vacuum carbon coater E306 (Edwards, Crawley, England) in order to avoid surface charging.

4.3.2 SEM/EDS characterization

Characterizations were performed with a Hitachi SU8230 cold field emission SEM (Hitachi High-Technologies, Rexdale, ON, Canada) equipped with a Bruker Flat Quad XFlaxh® 5060F aSDD (Bruker Nano, Berlin, Germany) with a 60-mm^2 collection area. Two sets of EDS maps were acquired for 5 minutes and 60 minutes in a same area at the condition listed in Table 4.1 using the Bruker ESPRIT software (version 1.9) (Bruker Nano). The probe current was measured with a Faraday cup mounted on the column with a NanoPico picoammeter from Hitachi (Hitachi High-Technologies), and the total counts were recorded by the Bruker ESPRIT.

Table 4.1 Current conditions of the map acquisitions.

Beam energy	Probe current	Collecting count rate	Total counts	
			5 min	60 min
20 kV	280 pA	67.6 kcps	20,688,661	201,809,640

4.3.3 Phase map analysis

To obtain the phase map, the conventional EDS qualitative maps were quantified by Bruker ESPRIT software to acquire the net intensity maps, and then the *f*-ratio of each element at every pixel was calculated using equation (4.1):

$$f_i = \frac{I_i}{\sum_i^N I_i} \tag{4.1}$$

where I_i is the net X-ray intensity of element i in a N-element system from one spectrum (Horny, 2006). Using equation 4.1, the qualitative map of each element was converted to its *f*-ratio map,

and a histogram of the *f*-ratio values was generated in the meantime. Figure 4.1 displays the *f*-ratio map of Si-Kα (a) and its histogram (b) as an example: the number of peaks in the histogram refers to the number of minerals containing Si. Then the mineral phases were manually defined with the ranges of the *f*-ratio values of the constituted elements according to the histograms, and an open source Python script, pyPhaseMap (available on GitHub as pyphasemap repository), was run to convert the elemental *f*-ratio maps into a phase map (Brodusch et al., 2017, Teng et al., 2018). The *f*-ratios do not represent the real composition, but they are proportional to the concentrations of the corresponding elements. The adjustable *f*-ratio range is important to analyze minerals as their chemical compositions are usually not constant. The area fraction of each phase was calculated to evaluate the phase maps acquired at different conditions. The major phases were identified in the major-phase maps, and the distributions of the REMs were illustrated through overlaying the REM-phase maps with the SE image.

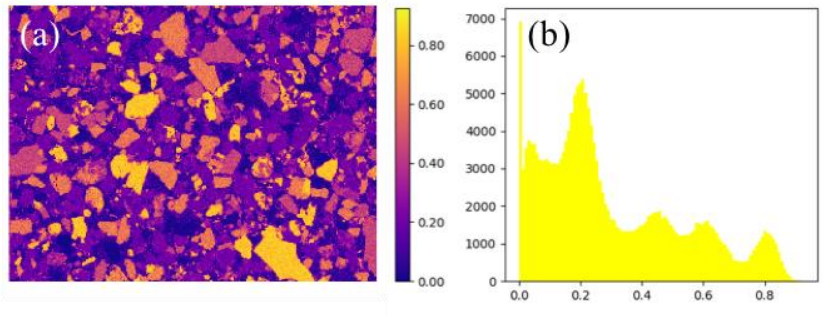

Figure 4.1 Si-Kα *f*-ratio map (a) and its histogram (b).

4.3.4 Multivariate statistical analysis

The Python based open source, Hyperspy (de la Peña et al., 2017), was used to perform the MSA, including the PCA, and the BSS using ICA and NMF algorithms, on the 5-minute map. The

number of pixels in the map is 512*384, so there are 512*384 channels of the SI dataset. The singular value decomposition algorithm was used for the PCA, and the cumulant based algorithm was used for the ICA. The explained variance ratio of the components decomposed by the PCA was plotted against the component index in a scree plot, which is helpful to estimate the number of components remaining for the denoising analyses and the output dimensions for the following BSS analyses, including the ICA and NMF treatments. In the BSS analyses, a new dataset was reconstructed with the selected components, and the modified X-ray intensity maps were retrieved from it. And then, the improved phase map analysis was performed with the modified X-ray maps. The 5-minute REM maps, including the original one and the MSA-modified ones, were evaluated by counting the correctly and incorrectly identified pixels, considering the 60-minute map as a reference: the pixels identified as rare earth phases both in the 5-minute map and the 60-minute map were counted as the correct phases, but those only identified in the 5-minute map were counted as the noise.

4.4 Results and Discussion

4.4.1 Denoising analysis with the PCA

Figure 4.2 displays the phase maps acquired at the conditions listed in Table 4.1. In the phase maps, only the major phases were identified, and a large amount of the minor phases were labeled as “Other”. The 60-minute maps, including the major-phase map [Figure 4.2(a)] and the REM-phase map [Figure 4.2(b)], are much clearer compared with the 5-minute maps [Figure 4.2(c)

the major-phase map and Figure 4.2(d) the REM-phase map] as a result of the approximate 10 times collected X-ray counts. The main rare earth carriers in this deposit: bastnäsite $(Ce,La,Y)F(CO_3)$, parisite $(Ca(Ce,La)_2(CO_3)_3F_2)$, and fergusonite $(YNbO_4)$ (Sheard et al., 2012), were identified in the maps. In the three REMs, the main REEs are La, Ce, Pr, and Nd, so these elements were used for the phase identification in this work. Figure 4.2(e) is the spatial difference map which was computed by subtracting the phases in Figure 4.2(b) from Figure 4.2(d) to show the pixels misidentified as the rare earth phases in the 5-minute map. These misidentified pixels are concentrated in the mounted epoxy resin and should be removed to make the real mineral phases more visible. The comparisons shown in Figure 4.2 confirm that the acquisition time of 5 minutes is insufficient for an accurate phase identification.

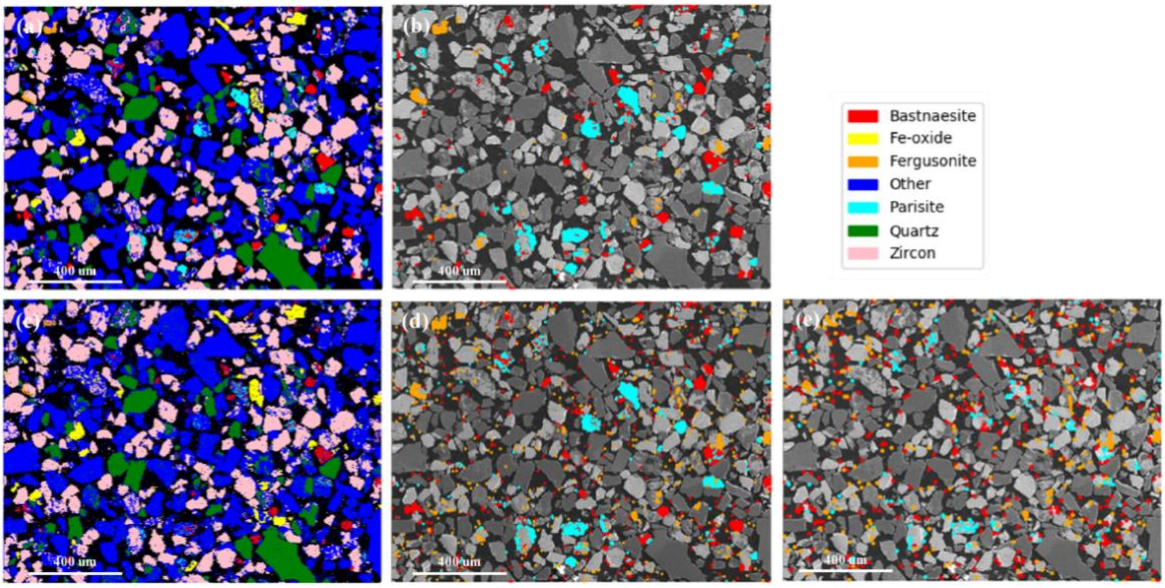

Figure 4.2 Phase maps acquired at the conditions listed in Table 4.1. (a) 60-minute major-phase map; (b) 60-minute REM-phase map; (c) 5-minute major-phase map; (d) 5-minute REM-phase map; and (e) 5-minute noise map.

In order to improve the 5-minute map, the PCA algorithm was executed to decompose the original map, and the variances of the first 50 components are plotted against their index in Figure 4.3. The routine PCA and the weighted PCA were both applied on the dataset, and their scree plots are displayed in Figure 4.3(a) and Figure 4.3(b), respectively. As shown in Figure 4.3(a), the leading 22 components have relatively higher variances compared to the rest, but the weighted PCA algorithm revealed the significantly higher variances of the first 9 components. A compromise should be made in the component selection: all the useful information ought to be included, but the less components remaining can effectively shorten the processing time. However, the physical meaning of each component cannot be interpreted, so a direct component selection for the new dataset construction cannot be achieved.

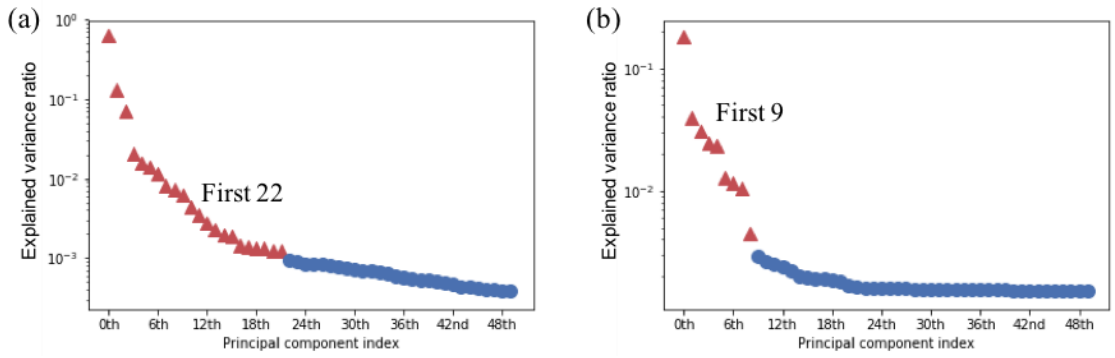

Figure 4.3 Explained variance ratio of the first 50 PCA components. (a) routine PCA; (b) weighted PCA.

The denoising analyses were performed with the first 9 and 22 components after the execution of the weighted and routine PCA algorithms, respectively, and the results were shown in Figure 4.4. As explained previously that the phase identification was processed with the elemental *f*-ratio maps which were computed with the elemental intensity maps by applying equation (4.1) at each pixel, the *f*-ratio map processing is critical to the phase map analysis. Figures

4.4(a) - 4.4(c) show the *f*-ratio maps of La-Lα (4.65 keV) as examples: Figure 4.4(a) is the original La-Lα *f*-ratio map, and Figures 4.4(b) and 4.4(c) are the denoised La-Lα *f*-ratio maps retrieved from the first 9 and 22 components. According to Figures 4.4(b) and 4.4(c), the major La-bearing phases are among the first 9 components as the two maps do not have significant differences.

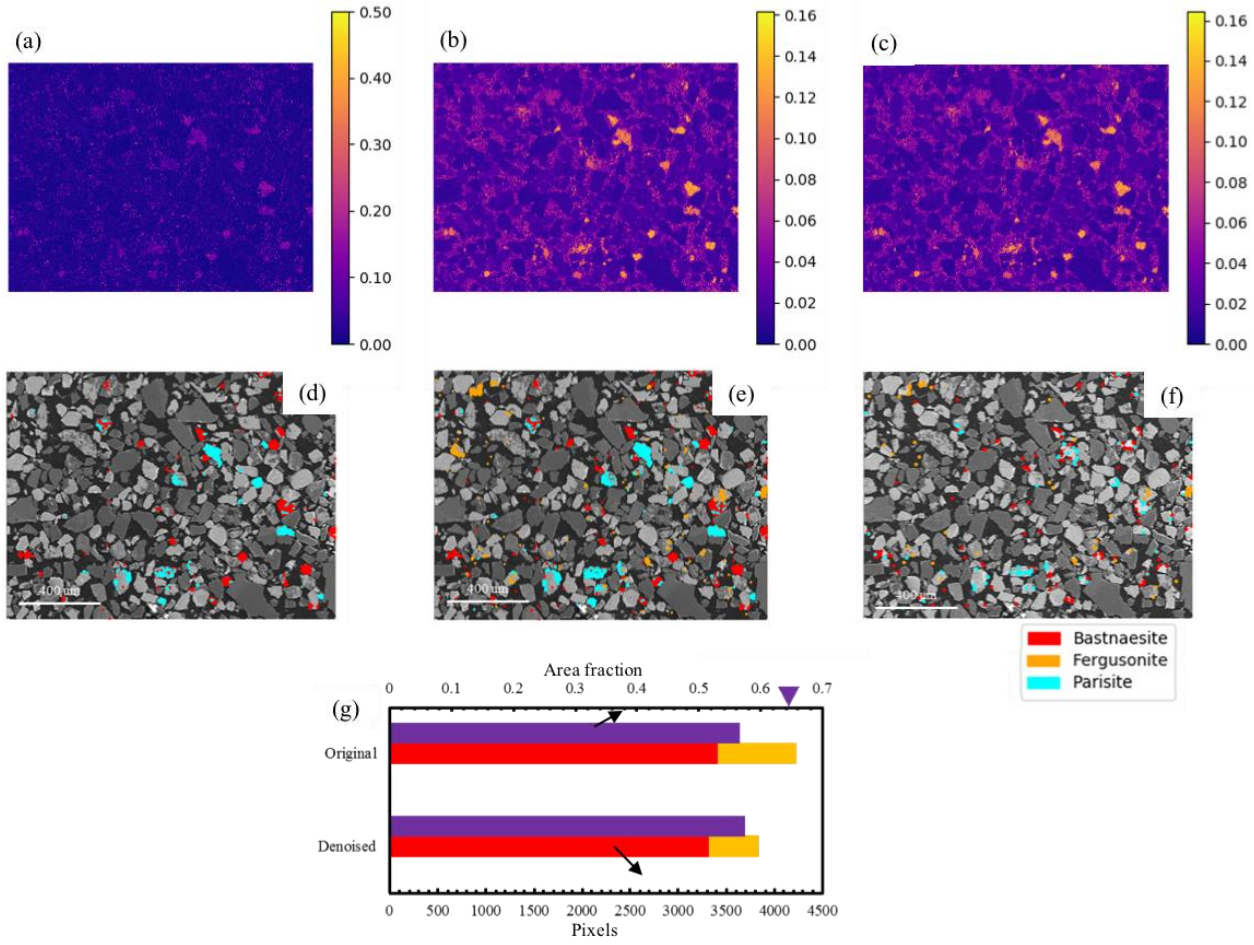

Figure 4.4 Denoising analyses with PCA on the 5-minute map. (a) Original La-Lα *f*-ratio map; (b) denoised La-Lα *f*-ratio map with the first 9 weighted PCA components; (c) denoised La-Lα *f*-ratio map with the first 22 routine PCA components; (d) REM-phase map with the first 9 weighted PCA components; (e) REM-phase map with the first 22 routine PCA components; (f) noise map of the 22-component denoised 5-minute map; (g) bar chart of the phase identification.

According to equation (4.1), the *f*-ratio is a normalized value, and is proportional to the concentrations of the corresponding elements. Since most minerals do not have constant chemical compositions, the computation of the *f*-ratio facilitates the phase identification by setting the threshold of each phase using the elemental *f*-ratio values, and the phase map is processed by applying the phase identification at each pixel. Figures 4.4(d) and 4.4(e) display the denoised REM-phase maps with the first 9 (weighted PCA) and 22 (routine PCA) components, which are both clearer than the original 5-minute map. However, when only the first 9 components were kept, the information of the orange phases (fergusonite) were totally discarded [Figure 4.4(d)]. Thus, the threshold of 22 is more appropriate to achieve both accurate phase identification and noise reduction.

Figure 4.4(f) shows the spatial difference map between the denoised 5-minute map using the first 22 routine PCA components and the 60-minute map. Compared to Figure 4.2(e), after the PCA denoising analysis, a large amount of noise was removed from the phase map. Figure 4.4(g) statistically compares the rare earth phases (red bars) and the noise (yellow bars) identified in the original 5-minute map and the 22-component denoised one. The two maps have similar pixels correctly identified as REM, but the modified map has significantly less noise. The purple bars represent the sum area fraction of all mineral phases, which show that the total identified pixels in the two maps are similar, but less than that in the 60-minute map (the purple triangle). Since the powder was mounted in the epoxy resin, the sum fraction of all mineral phases does not equal unity. Either the observation on the maps or the data summarized in the chart confirms that the decomposition of the original dataset and the reconstruction with selected PCA components can achieve the reduction of misidentified pixels and a more accurate phase identification.

Since there are a large number of minerals in this sample, the number of remaining components should be carefully checked in order to save processing time and avoid phase omissions. However, taking this 5-minute map as an example, the optimal denoising threshold might be a number between 9 and 22, but the detailed selection cannot be further made due to the unknown information in each component. In this case, the BSS is a more convenient method as each component can be physically interpreted.

4.4.2 ICA-based and NMF-based BSS analyses

Two BSS algorithms, the ICA and NMF, were executed on the 5-minute dataset, and the output dimension was set to 22 according to the previous PCA results. A direct phase separation was achieved with the two algorithms: each BSS component was distinguished in the form of a multi-element X-ray intensity map and its sum spectrum, which presents the phases with similar chemical compositions. The spectrum is helpful for phase identification, and the map directly shows the phase distribution.

Figure 4.5 shows the rare earth components (RE-components) separated by the ICA algorithm, including the bastnäsite and parasite [Figure 4.5(a)], and the fergusonite [Figure 4.5(b)]. Remarkably, there are some non-rare-earth phases presenting darker particle profiles compared with the epoxy background in the distribution map [as arrowed in white in Figure 4.5(b)]. Since the ICA algorithm allows both combinations and subtractions, the subtraction calculation may result in negative values and physically uninterpretable results in an EDS map. Except for the

mineral phases, the component of epoxy resin was also distinguished from the original dataset, as shown in Figure 4.5(c).

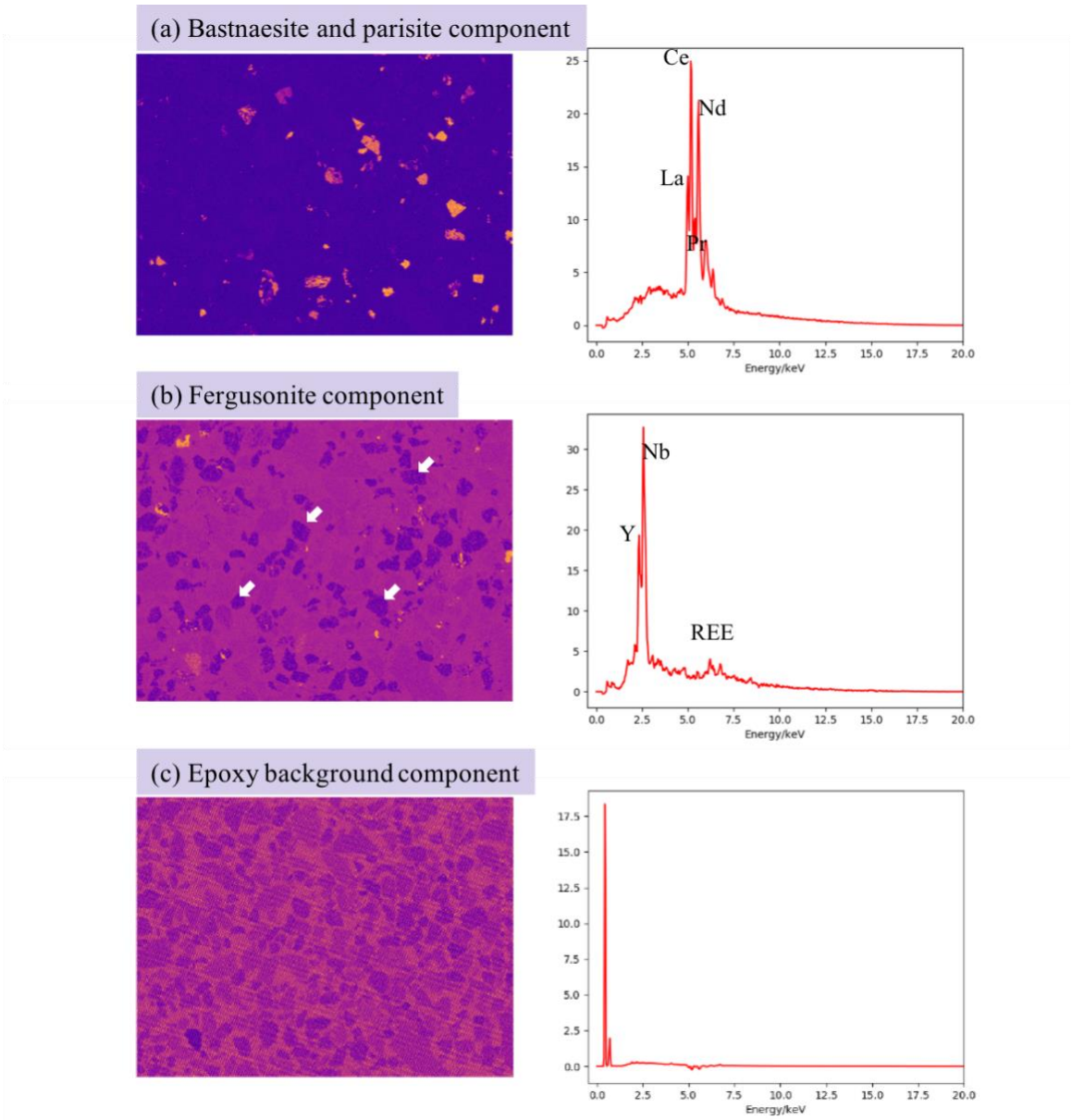

Figure 4.5 RE-components separated by ICA-based BSS. (a) Bastnäsite and parisite component; (b) fergusonite component; (c) epoxy component.

The ICA makes the component selection much easier, but the recognition power for the phase separation is decided by the preset output dimension. As shown in Figure 4.5(a), the

bastnäsite and the parisite were considered as one component when the dimension was set to 22. If further differentiation between the two phases needs to be processed, there will be repetitive attempts to set the output dimension and perform the data separation as the components are unpredictable. In addition, the computation time is also a considerable issue, which limits the output dimension not to set to a large number. Thus, it is preferred to reconstruct a new dataset with selected components, retrieve the modified X-ray intensity maps, and then perform a phase map analysis with the manual identification.

Regarding the retrieval of the modified X-ray intensity maps, the different component selection for the new dataset reconstruction may lead to different results. Figure 4.6(a) shows the La-Lα intensity map retrieved from the full dataset without any component exclusion. The non-rare earth phases can be obviously observed as the collected X-ray counts are insufficient. Also, the noise collected from the epoxy background is also shown in this map. As shown in Figure 4.5(c), the epoxy background component was also identified and separated from the original dataset, so this component could be excluded when the new dataset was reconstructed. The modified La-Lα intensity map retrieved from the dataset excluding the epoxy resin component is shown in Figure 4.6(b). This map is slightly clearer than Figure 4.6(a), but other mineral phases are still visible. Figure 4.6(c) shows the map retrieved only from the RE-components, which thoroughly avoids the interferences from other phase signals. However, the uninterpretable dark particle profiles are also observed in Figure 4.6(c) (as arrowed in white).

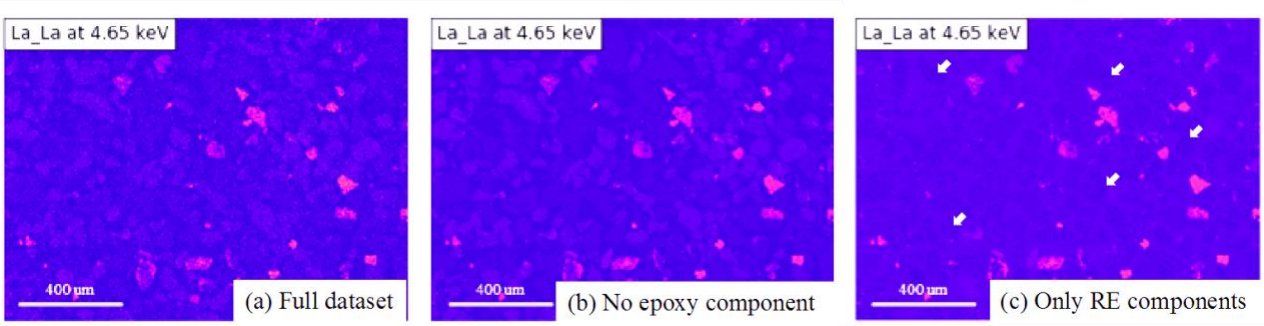

Figure 4.6 La-Lα intensity maps retrieved from ICA datasets.

Since the ICA allows the complex cancellations between positive and negative numbers to realize the linear combination of these components, the decomposed EDS spectrum and the map may lose their intuitive physical meanings and fail to duplicate the reality (Wu et al., 2010). By contrast, the NMF-based BSS only allows the combinations and can thoroughly avoid this issue. Figure 4.7 shows the NMF RE-components, including the bastnäsite and parasite component [Figure 4.7(a)], the fergusonite component [Figure 4.7(b)], and the epoxy component [Figure 4.7(c)]. Figure 4.8 illustrates the comparison of the La-Lα intensity maps, including the one retrieved from the full dataset [Figure 4.8(a)], the modified one retrieved from the dataset excluding the NMF epoxy component [Figure 4.8(b)], and the map retrieved from the NMF RE-components [Figure 4.8(c)].

As shown in Figure 4.7, the NMF RE-components fit better with the fact without the dark particle profiles compared with the ICA components. Regarding the X-ray intensity map, the La-Lα map retrieved from the RE-components [Figure 4.8(c)] successfully gets rid of the noise from the epoxy background and the interferences from other phases. However, the NMF spectra are far from a real EDS spectrum with some sharp jumps, and by contrast, the ICA spectra have much smoother outlines. A more direct comparison is illustrated in Figure 4.9, which displays the ICA

and NMF spectra of the bastnäsite and parisite component, and a real EDS spectrum extracted from a bastnäsite phase. The spectra after the BSS treatments represent the X-ray signals of the separated components, so strange jumps are observed compared to the conventional EDS spectrum.

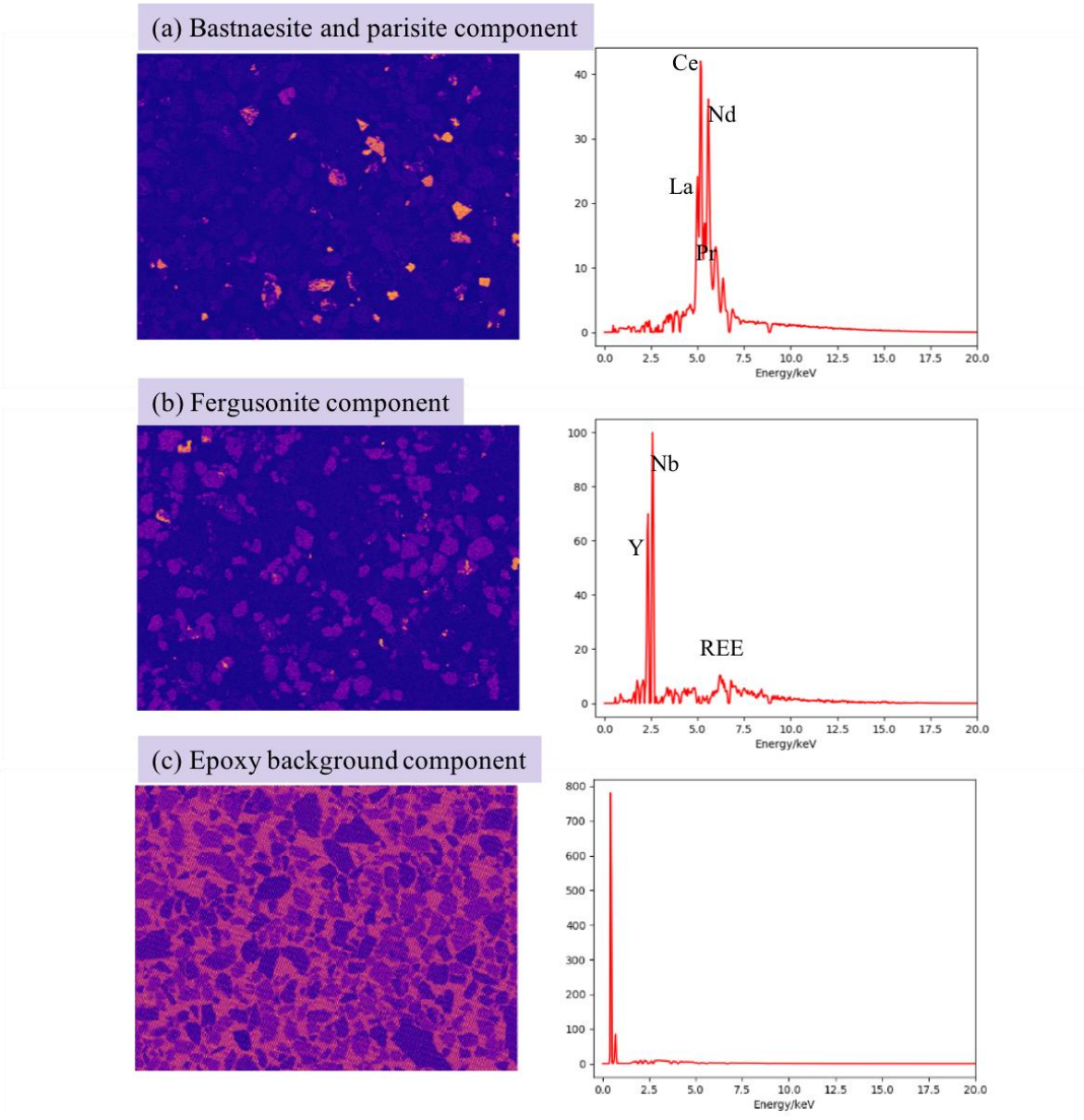

Figure 4.7 RE-components separated by NMF-based BSS. (a) Bastnäsite and parisite component; (b) fergusonite component; (c) epoxy component.

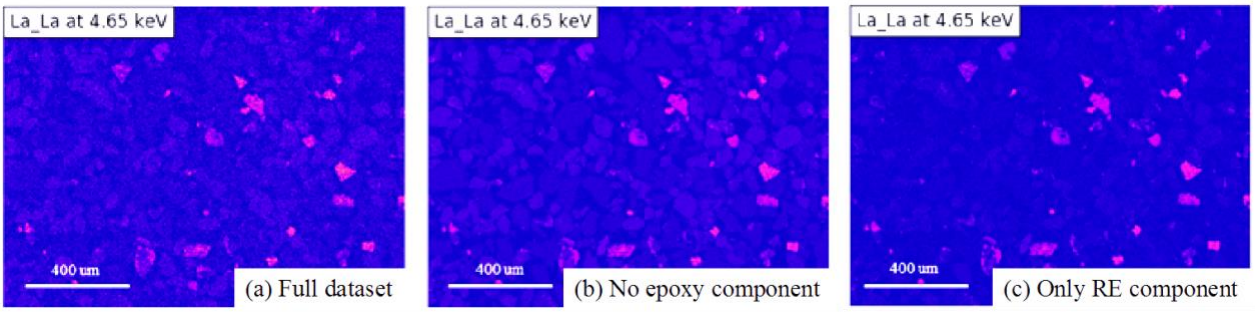

Figure 4.8 La-Lα intensity maps retrieved from NMF datasets.

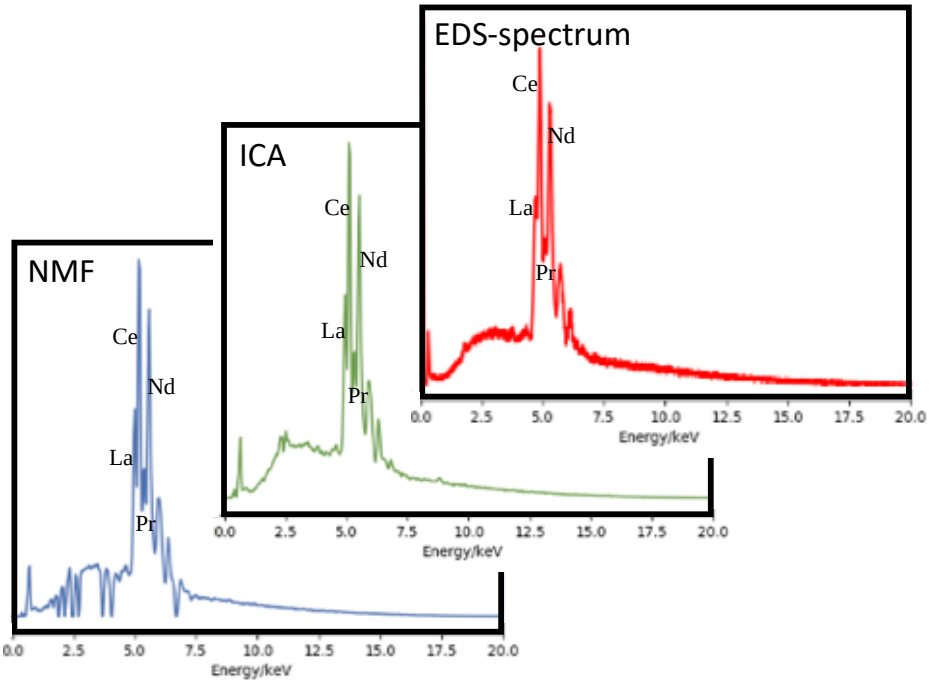

Figure 4.9 Comparison between ICA and NMF spectra and a real EDS spectrum.

With the modified X-ray maps retrieved from the reconstructed dataset, the phases were further identified. The phase maps were processed with the different datasets reconstructed with the selected ICA and NMF components, and they are statistically compared in terms of the phase identification of the rare earth phases (red bars) and the noise (yellow bars), and the sum area fraction of all mineral phases (purple bars) in Figure 4.10. Two datasets were reconstructed for the ICA and NMF algorithms respectively: one with all the components and one excluding the epoxy

component. As shown in this figure, both the NMF and ICA algorithms significantly denoised the map, but there are less rare earth phases identified after the ICA treatment. Additionally, the subtractions of the epoxy background do not further improve the maps. Since the BSS calculation aims to recover the sources using the observed data, the dataset separation can underscore the data structure. Thus, even without component exclusion, the mineral phases can be more outstanding just through the data decomposition and reconstruction.

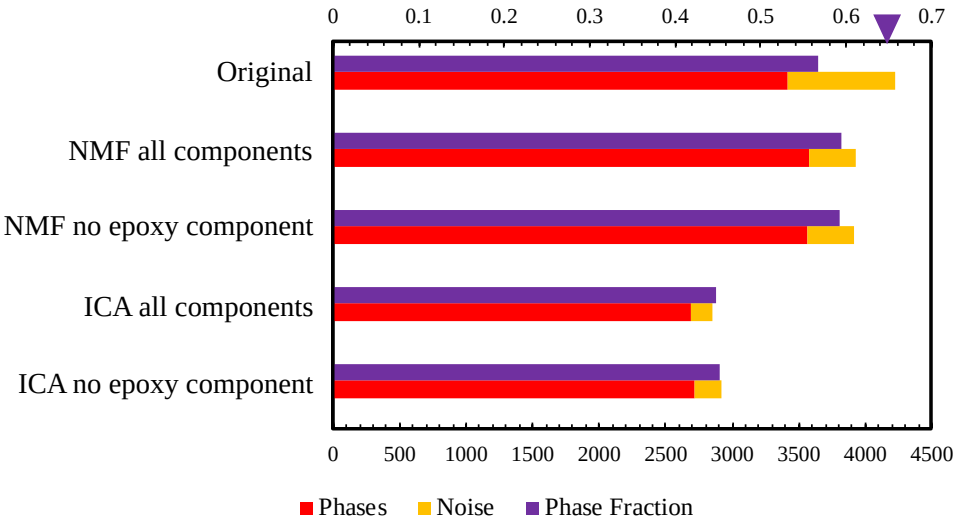

Figure 4.10 Rare earth phases (red bars) and noise (yellow bars) identified in the 5-minute map datasets. The purple bars represent the proportions of all phases identified in the 5-minute maps, and the purple triangle indicates that in the 60-minute map.

Besides the identification of REMs, the proportion of all identified mineral phases (purple bars) is also an important criterion for evaluating the applied algorithms. As shown in Figure 4.10, the NMF algorithm can also increase the proportion of all phases, improving the identification power for the 5-minute map. The ultimate objective of this study is to find the optimal procedure to achieve an efficient phase analysis, which can render the 5-minute map with the 60-minute

quality. Compared with the original 5-minte map, the BSS modified maps have great improvements, and can achieve a similar quality of the 60-minute one.

4.5 Conclusion

The PCA and BSS analyses were performed on an EDS map dataset which was acquired on a REM sample for only 5 minutes. Through the denosing analysis with the PCA, a much clearer phase map was obtained. The number of remaining components should be carefully checked in order to avoid the phase omissions and save the computation time. The BSS treatments can provide a similar denoising result, but they have different principles: the PCA-denoising is achieved by remaining the components with higher variances and discarding the rest as noise, but the BSS-denoising is achieved by directly excluding the undesired components.

Through the performance of BSS, the mineral phases with similar compositions were directly separated, bringing convenience to the phase identification. However, due to the complex nature of this mineral sample, an accurate component separation is not easily achieved just using the BSS. In order to avoid repetitive attempts on the data separation, it is preferred to combine the BSS analysis with the conventional phase map analysis. The components decomposed by the BSS can provide a preliminary idea of the sample, and then the phase map can be processed with the modified X-ray intensity maps which are retrieved from the reconstructed dataset. In this way, the phase identification and noise reduction can be both achieved. Through the comparisons between

the ICA and NMF algorithms the NMF is more suitable for a phase map analysis due to its smaller signal reduction.

Chapter 5

The *f*-ratio Quantification Method for X-ray Microanalysis Applied to Mg-Al-Zn Alloys

In Chapters 3 and 4, the highly efficient phase map analysis produced with the elemental X-ray maps acquired using an SEM/EDS system was described. The *f*-ratios calculated with the characteristic X-ray intensities of constituent elements were used for phase identification. In this chapter, the quantification method based on the *f*-ratio computation, the *f*-ratio method, was applied to Mg-Al-Zn systems. The use of pure-element (PE) standards and the beam current influences are investigated.

- This chapter has been published as: Teng, C.*, Demers, H., Chu, X. & Gauvin, R. (2019). The *f*-ratio Quantification Method for X-ray Microanalysis Applied to Mg-Al-Zn Alloys. *Microscopy and Microanalysis* **25(**1), 58-69. doi:10.1017/S1431927618015684.

5.1 Abstract

The *f*-ratio quantitative X-ray microanalysis method has been recently developed for binary systems based on a scanning electron microscope/energy dispersive spectroscopy (SEM/EDS) system. This method incorporates traditional EDS experiments and Monte Carlo simulations, and calibration factors are calculated with standard samples to evaluate the differences between them. In this work, the *f*-ratio method was extended to Mg-Al-Zn multi-element systems using a cold field emission SEM and a tungsten emission SEM. Results show that the stability of the beam current does not influence the *f*-ratio quantification accuracy. Thus, the *f*-ratio method is suitable for quantitative X-ray mapping with a long-time acquisition or even an unstable beam current. Compared to other quantitative techniques including the routine standardless analysis and the standard-based *k*-ratio method, the *f*-ratio method is a simple and accurate quantification method.

5.2 Introduction

A scanning electron microscope/energy dispersive spectroscopy (SEM/EDS) system is a popular instrument for quantitative X-ray microanalysis due to its simple and fast operation. The use of a silicon drift detector endows the EDS spectrum acquisition with high efficiency and good energy resolution (125-129 eV, full peak width at half maximum at Mn Kα: 5,890 eV) (Newbury, 2002; Çubukçu et al., 2008; Newbury & Ritchie, 2015). Regarding the quantitative analysis, the Castaing equation (*k*-ratio method) (Castaing, 1951) enables EDS to be performed as a standard-based quantification technique with accuracy and precision comparable to wavelength dispersive spectrometry (WDS) (Ritchie et al., 2012). In order to make full use of the advantage that an EDS spectrum can exhibit all characteristic X-ray peaks at one time, the standardless method was developed to eliminate the needs for real standards and measurements of electron dose, but the quantification accuracy is greatly undermined (Newbury et al., 1995; Çubukçu et al., 2008; Newbury & Ritchie, 2013). Therefore, the *f*-ratio method, which has similar experimental procedures with the routine EDS standardless analysis, was developed as an alternative to the traditional *k*-ratio method to perform the standard-based quantitative analysis (Horny, 2006; Horny et al., 2010).

The *f*-ratio method incorporates EDS experiments and Monte Carlo simulations, and calibration factors are calculated with standard samples having known compositions to evaluate the differences between them. This method has been applied to the binary Cu-Au standard alloy [SRM 482, from the National Institute of Standards and Technology (NIST) standards mounted by Geller MicroÅnalytical Laboratory Inc., Boston, MA, USA] of 20, 40, 60, and 80 wt.% of Au, and the quantification results reach an accuracy better than 5% with beam-energy-dependent

calibration factors, which is better than the EDS standardless quantification (Horny et al., 2010). However, Horny used the Cu-Au alloy (40 wt.% Au) to calculate the calibration factors and to compute the compositions of other Cu-Au alloys, restricting the choice of standards: only a compound standard which contains all the target elements could be used. With the number of constituent elements increasing, it becomes harder to find such a compound standard, and it would be more convenient if pure-element (PE) standards can be used. Thus, the purpose of this work is to extend the *f*-ratio method to multi-element systems and to validate the use of PE standards in the *f*-ratio quantification.

In this work, two types of Mg-Al-Zn ternary systems: an Mg_{45}-Al_{27}-Zn_{28} cast alloy and an Mg-Al-Zn diffusion alloy were quantitatively analyzed by the SEM/EDS systems using the *f*-ratio method with the compound standard and PE standards. A cold field emission SEM (CFE-SEM) and a tungsten emission SEM were used to investigate the influence of the beam current stability on the *f*-ratio quantification accuracy. The quantification results of the *f*-ratio method were compared with the EDS standardless analysis and the standard-based *k*-ratio method.

5.3 The *f*-ratio Quantification Method

The theory of quantitative X-ray microanalysis was firstly proposed by Castaing in 1951, and then was developed to the well-known *k*-ratio method (Castaing, 1951; Goldstein et al., 1981). However, this method requires an identical acquisition condition for the unknown specimen and standards, which is difficult to achieve in a CFE-SEM due to its unstable beam current. In order to

eliminate the influence of beam current, the Cliff-Lorimer method (Cliff & Lorimer, 1975) was proposed, which uses a ratio of the characteristic X-ray intensities of two elements ($\frac{I_A}{I_B}$) in one spectrum. However, this method is not suitable for systems having trace elements: when I_B is close to 0, the use of I_B in denominator will cause large variations in the ratio due to the poor counting statistics (Horny et al., 2010). Thus, in order to resolve these issues, the *f*-ratio method was developed, which can be described as:

$$f_A = \frac{I_A}{I_A + I_B} \tag{5.1}$$

where I_A and I_B are the net characteristic X-ray intensities in one spectrum. Instead of thin-foils studied in the Cliff-Lorimer method, the *f*-ratio method was firstly developed for bulk samples.

One feature of this method is that it couples the EDS experiment and the Monte Carlo simulation. In this work, the MC X-ray program (v1.6.4) (Gauvin & Michaud, 2009) was used to perform the simulations of X-ray generations and emissions. It is an easy program to input the desired sample composition, select the physical models for X-ray generation and emission, set the microscope parameters, and obtain the simulated X-ray intensities. The effects of the beam energy, ionization cross-section models, mass-absorption coefficients, and X-ray generation methods are all calculated in the simulations.

The first step to perform the *f*-ratio quantification is to calculate the calibration factors with standards. The *f*-ratio method requires a standard sample with known composition to correct the differences between experiments and simulations. With the standard sample, the experimental intensities (I_A^{exp} and I_B^{exp}) are measured and the experimental *f*-ratios (f_A^{exp} and f_B^{exp}) are calculated. Then, the theoretical intensities (I_A^{th} and I_B^{th}) are simulated with the composition of the

standard, and the theoretical *f*-ratios (f_A^{th} and f_B^{th}) are calculated. After that, the experimental and simulated *f*-ratios can be associated by inserting a calibration factor Λ_{A-B}:

$$f_A^{exp} = \frac{I_A^{exp}}{I_A^{exp}+I_B^{exp}} = \frac{I_A^{th}}{I_A^{th}+\Lambda_{A-B}I_B^{th}} \tag{5.2}$$

Thus, the calibration factor Λ_{A-B} is determined as:

$$\Lambda_{A-B} = \frac{f_A^{th}}{f_B^{th}}\frac{f_B^{exp}}{f_A^{exp}} = \frac{I_A^{th}}{I_B^{th}}\frac{I_B^{exp}}{I_A^{exp}} \tag{5.3}$$

The X-ray intensities of A and B used to calculate the *f*-ratios are from the same spectrum, so the computed calibration factor is independent of the beam current. Additionally, it is recommended to use an energy-dependent calibration factor to obtain a higher quantification accuracy (Horny, 2010). In a multi-element system, calibration factors for each pair of elements are required, and their *f*-ratios are given as:

$$f_i = \frac{I_i^{th}}{I_i^{th}+\sum_{i\neq j}\Lambda_{i-j}I_j^{th}} \tag{5.4}$$

However, if PE standards are used, the beam current and the acquisition time should be measured during the acquisitions on the standards in order to correctly simulate the X-ray emission with the same electron dose. Thus, the calibration factor should be calculated for each element as:

$$\Lambda_A = \frac{I_A^{exp}}{I_A^{th}} \tag{5.5}$$

Even though equation (5.5) and the conventional *k*-ratio both use the X-ray intensities of the same element, equation (5.5) compares the experiment and simulation, but the *k*-ratio compares the

unknown sample and the standard. With the calibration factors calculated with PE standards, the *f*-ratio should be rewritten as:

$$f_A^{exp} = \frac{I_A^{exp}}{I_A^{exp}+I_B^{exp}} = \frac{\Lambda_A I_A^{th}}{\Lambda_A I_A^{th}+\Lambda_B I_B^{th}} = \frac{I_A^{th}}{I_A^{th}+\frac{\Lambda_B}{\Lambda_A} I_B^{th}} \tag{5.6}$$

$$f_i = \frac{I_i^{th}}{I_i^{th}+\sum_{i\neq j}\frac{\Lambda_j}{\Lambda_i} I_j^{th}} \tag{5.7}$$

The *f*-ratio quantification works by performing simulations on the target system to build the relationship between the system composition and its elemental *f*-ratios. A Python script is used to change the composition in the target system, input the compositions into the MC X-ray program (Gauvin & Michaud, 2009), and obtain the theoretical X-ray intensities. The step size of the compositional change determines the precision of the quantification results. However, if the step size is too small, the quantification efficiency will be undermined.

With the simulated X-ray intensities, the calibrated *f*-ratios can be calculated according to equation (5.4) or (5.7) depending on the types of standards used, and then associated with the system composition. This relationship is the key for the *f*-ratio quantification, which is used to find the corresponding composition with the experimental *f*-ratios of the unknown sample measured by a routine EDS acquisition. The experimental procedures are the same as the standardless analysis without the need to measure the beam current. However, the current limitation of the *f*-ratio method is the normalized quantification result, as the input composition to the MC X-ray program has to be normalized. Thus, the constituent elements should be accurately identified before the quantification.

5.4 Samples and Experimental Methods

5.4.1 Standard Mg_{45}-Al_{28}-Zn_{27} alloy

A Mg-Al-Zn cast alloy with an inductively coupled plasma atomic emission spectroscopy (ICP-AES) measured composition of 44.74 wt.% Mg, 27.76 wt.% Al, and 27.50 wt.% Zn was studied in this work. It was used as the target specimen for the quantitative analyses, and the ICP-AES result was considered as the reference composition. Although it is not a homogeneous sample [its backscattered electron (BSE) image is shown in Figure 5.1], its composition is consistent when large areas at a low magnification are analyzed. The electron probe microanalyzer (EPMA)/ wavelength dispersive spectroscopy (WDS) results show that this sample has an average composition of 44.75 ± 0.19 wt.% Mg, 28.82 ± 0.27 wt.% Al, and 27.91 ± 0.41 wt.% Zn with five raster beam analyses performed on areas of 253 × 189 μm^2 (magnification 500×). Thus, the alloy was also used as a standard compound to calculate the calibration factors. The influence of its heterogeneity on the quantifications will be discussed later.

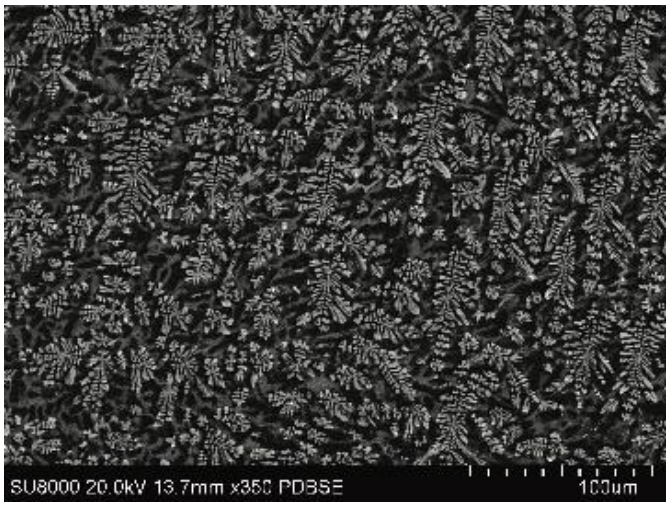

Figure 5.1 BSE image of Mg_{45}-Al_{28}-Zn_{27} alloy at 20 kV.

For SEM observations, the sample was ground with silicon carbide papers from 100 to 1200 grit and then polished with the diamond paste of 3 μm (Buehler, Lake Bluff, IL, USA) and 1 μm grain size (Anamet, Montreal, QC, Canada). The final polishing step was performed with the OP-S Suspension (Struers Inc., Cleveland, OH, USA). Since Mg-Al alloys are susceptible to oxidation, ethyl alcohol was used as a lubricant during the polishing.

5.4.2 Mg-Al-Zn-Cu diffusion alloy

The Mg-Al-Zn-Cu diffusion alloy was also studied in this work. To fabricate this diffusion sample, four pieces of pure metals (aluminum, magnesium, zinc, and copper) were subjected to a preliminary polishing treatment to obtain a flat and clean surface. After that, they were placed together according to the schematic view in Figure 5.2(a), and then sealed into a quartz tube filled with argon gas. The tube was inserted in a Lindberg tube electrical resistance furnace at 325 °C for 20 days to allow diffusion. After 20 days, the sample was taken out, mounted in an epoxy resin, and prepared for SEM observations. The metallographic preparation procedures used for this sample were the same as above.

The diffused layers formed at interfaces between the different pieces, while the regions far from the interfaces remained pure metals. A clearer illustration of the diffusion sample is shown in the BSE image [Figure 5.2(b)]. The Mg-Al-Zn alloy was used for the analysis of the ternary system, and the pure metals located far from the interfaces were used as the PE standards.

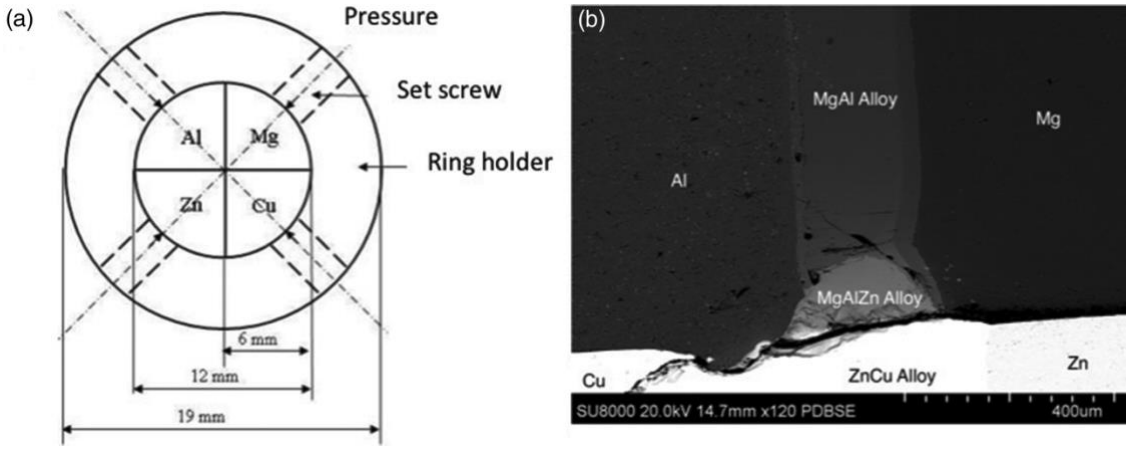

Figure 5.2 The Mg-Al-Zn-Cu diffusion alloy sample: (a) schematic view and (b) BSE image.

5.4.3 Microanalysis

A CFE-SEM, Hitachi SU-8000 (Hitachi High-Technologies, Rexdale, ON, Canada) was used for observations. The CFE features the increased brightness and small beam size, but the beam current is not stable. A tungsten emission SEM, Hitachi SU-3500 (Hitachi High-Technologies, Rexdale, ON, Canada) with a relatively stable current was also used. In the Hitachi SU-8000, EDS X-ray microanalysis was performed using an 80 mm^2 silicon drift detector (Oxford, Abingdon, Oxfordshire, UK) controlled by INCA software (version 4.15) (Oxford, Abingdon, Oxfordshire, UK). In the Hitachi SU-3500, EDS analysis was performed using the same detector controlled by an Aztec software (version 3.0) (Oxford, Abingdon, Oxfordshire, UK). The CASINO program (v2.4.9.2) (Drouin et al., 2007) was used to compute the electron and X-ray ranges excited by the electron beam.

For the Mg_{45}-Al_{28}-Zn_{27} alloy, its average bulk composition was analyzed by performing the SEM/EDS analyses on areas with a size of 253 × 189 μm^2 (magnification 500×) at 20 kV with

a live time of 300 s. Both the Hitachi SU-8000 and Hitachi SU-3500 were used, in order to investigate the influence of the beam current stability on the quantification results. Various quantitative techniques were applied, including the *f*-ratio method, the standardless and standard-based analysis performed by the software attached to the respective spectrometer (INCA for the Hitachi SU-8000 and Aztec for the Hitachi SU-3500), and the standard-based *k*-ratio method performed by the DTSA-II software (version Jupiter 2017-11-06) (Ritchie, 2011a). The PE standards (SPI Supplies Inc., West Chester, PA, USA) were used for all the standard-based analyses. A Faraday cup with a NanoPico picoammeter (Hitachi High-Technologies, Rexdale, ON, Canada) was used to measure the beam currents before and after each point acquisition on the PE stanards with a live time of 300 s. This specimen was also analyzed by an EPMA/WDS system (JEOL 8900) (JEOL, Peabody, MA, USA) with a raster beam on areas of 253 × 189 μm^2 (magnification 500×) at 20 kV with the acquisition time of 60 s for each peak, and MgO, Al_2O_3, and ZnO were used as standards for Mg, Al, and Zn, respectively.

Since the Mg_{45}-Al_{28}-Zn_{27} alloy is a multiphase sample, the composition of each phase was also analyzed by the *f*-ratio method. The EDS point analyses were performed with the Hitachi SU-8000 at 5 kV with a live time of 300 s. The *f*-ratio quantitative X-ray maps were also computed for this sample. An overnight (~ 6 hours) X-ray map was acquired with the Hitachi SU-8000, then the *f*-ratio calculation was applied on each pixel, and the phase map was calculated with a Python script (Teng et al., 2018).

For the Mg-Al-Zn diffusion sample, line scan analyses were performed with the Hitachi SU-8000 at 5 and 20 kV. The live time of each point on the line scan was 60 s. The same set of data was analyzed by the *f*-ratio method, the EDS standardless analysis, and the standard-based *k*-

ratio method performed with DTSA-II software (Ritchie, 2011a). The PEs located far from the diffusion layers were used as PE standards for the *f*-ratio method and the *k*-ratio method. The beam current was measured by a Faraday cup with a NanoPico picoammeter (Hitachi High-Technologies, Rexdale, ON, Canada) before and after each point acquisition with a live time of 300 s. In addition, the Mg_{45}-Al_{28}-Zn_{27} alloy was also used as the compound standard for the *f*-ratio quantification on this alloy, and area spectra with a size of 253 × 189 μm^2 (magnification 500×) were acquired with a live time of 300 s.

5.4.4 The *f*-ratio quantifications on Mg-Al-Zn systems

To perform the *f*-ratio quantification method on the Mg-Al-Zn systems, the calibration factors between the three elements were calculated according to equation (5.3) or (5.5) depending on the types of standards used. When the Mg_{45}-Al_{28}-Zn_{27} alloy was analyzed, the simulated X-ray intensities were calibrated with the PE standards, so the calibration factors were calculated as:

$$\Lambda_{Mg} = \frac{I_{Mg}^{exp}}{I_{Mg}^{th}};\ \Lambda_{Al} = \frac{I_{Al}^{exp}}{I_{Al}^{th}};\ \Lambda_{Zn} = \frac{I_{Zn}^{exp}}{I_{zn}^{th}} \tag{5.8}$$

But when the Mg_{45}-Al_{28}-Zn_{27} alloy was used as a standard, the calibration factors were calculated as:

$$\Lambda_{Mg-Al} = \frac{I_{Mg}^{th}}{I_{Al}^{th}}\frac{I_{Al}^{exp}}{I_{Mg}^{exp}};\ \Lambda_{Mg-Zn} = \frac{I_{Mg}^{th}}{I_{Zn}^{th}}\frac{I_{Zn}^{exp}}{I_{Mg}^{exp}};\ \Lambda_{Al-Zn} = \frac{I_{Al}^{th}}{I_{Zn}^{th}}\frac{I_{Zn}^{exp}}{I_{Al}^{exp}} \tag{5.9}$$

Due to the poor energy resolution in an EDS spectrum, the sum of a whole X-ray family intensity (e.g., for Al, the sum of intensities of Kα and Kβ) was used in the calculations to avoid the error introduced by deconvolution.

Table 5.1 shows the models applied to simulate the X-ray generation and emission in the MC X-ray program. The microscope parameters were set according to the corresponding instrument and the experimental conditions, such as the accelerating voltage and the take-off angle. When the PE standards were used, the electron dose of each standard was kept the same for the experiment and the simulation. In addition, the detector efficiency is a key factor for X-ray collection, but some basic parameters (e.g., the thickness of the window) are difficult to be accurately measured, so the default settings of the detector were used. Since the calibration factors are aimed at evaluating the differences between the experiments and simulations, they are reusable at the same accelerating voltage with the same instrument.

To build the relationship between the system composition and its elemental *f*-ratios, the simulations were performed on the Mg-Al-Zn system with a step size of 0.05 atomic fraction. For example, the first input composition to the simulation was $Mg_{0.00}Al_{0.00}Zn_{1.00}$, and then the second was $Mg_{0.00}Al_{0.05}Zn_{0.95}$. In this way, the simulations were run over all the possible compositions in the Mg-Al-Zn system. And then, the calibrated *f*-ratios were calculated as equations (5.10) - (5.12) depending on the standards applied:

$$f_{Mg} = \frac{I_{Mg}}{I_{Mg}+\Lambda_{Mg-Al}I_{Al}+\Lambda_{Mg-Zn}I_{Zn}} \; or \; \frac{I_{Mg}}{I_{Mg}+\frac{\Lambda_{Al}}{\Lambda_{Mg}}I_{Al}+\frac{\Lambda_{Zn}}{\Lambda_{Mg}}I_{Zn}} \tag{5.10}$$

$$f_{Al} = \frac{I_{Al}}{I_{Al}+\Lambda_{Al-Mg}I_{Mg}+\Lambda_{Al-Zn}I_{Zn}} \; or \; \frac{I_{Al}}{I_{Al}+\frac{\Lambda_{Mg}}{\Lambda_{Al}}I_{Mg}+\frac{\Lambda_{Zn}}{\Lambda_{Al}}I_{Zn}} \tag{5.11}$$

$$f_{Zn} = 1 - f_{Mg} - f_{Al} \quad (5.12)$$

Table 5.1 Models used for Monte Carlo simulations performed by MC X-ray software.

Parameter	Model
Total Elastic Cross Sections	
Elastic Electron Cross Section	Mott (Czyżewski et al., 1990) & Browning (Browning et al., 1994)
Screening	Henoc & Maurice (Henoc & Maurice, 1976)
Elastic Collisions	
Electron Energy Loss	Bethe (Bethe et al., 1938) & Joy & Luo (Joy & Luo, 1989)
Mean lionization potential	Joy & Luo (Joy & Luo, 1989)
Computation of X-rays	
Mass Absorption Coefficient	Chantler (Chantler, 1995; Chantler, 2000)
Characteristic Cross Section	Casnati (Casnati et al., 1982)
Bremsstrahlung Cross Section	Kirkpatrick & Wiedmann (Kirkpatrick & Wiedmann, 1945)

Thus, the relationship between the system composition and the calibrated theoretical *f*-ratios was obtained. After finishing all the simulation works, the EDS acquisitions were performed on the unknown target sample to obtain f_{Mg}^{exp}, f_{Al}^{exp}, and f_{Zn}^{exp}. And then, the unknown composition was interpolated by a Python script with the experimental *f*-ratios.

5.5 Results and Discussion

5.5.1 The *f*-ratio quantitative analysis on Mg_{45}-Al_{28}-Zn_{27} alloy

5.5.1.1 Calibration factors with PE standards

To investigate the influence of the beam current on the PE standard-based calibration factors, a CFE-SEM (Hitachi SU-8000) and a tungsten emission SEM (Hitachi SU-3500) were both used. The CFE gun usually has an intrinsic poor beam current stability despite its excellent

resolution capabilities; while the thermal field emitter generates a more stable current. Figure 5.3 shows the beam currents of the CFE-SEM (Hitachi SU-8000) and the tungsten emission SEM (Hitachi SU-3500) measured over 160 min, and the results confirm that larger variations (12 vs. 4.5%) and fluctuations are observed with the Hitachi SU-8000.

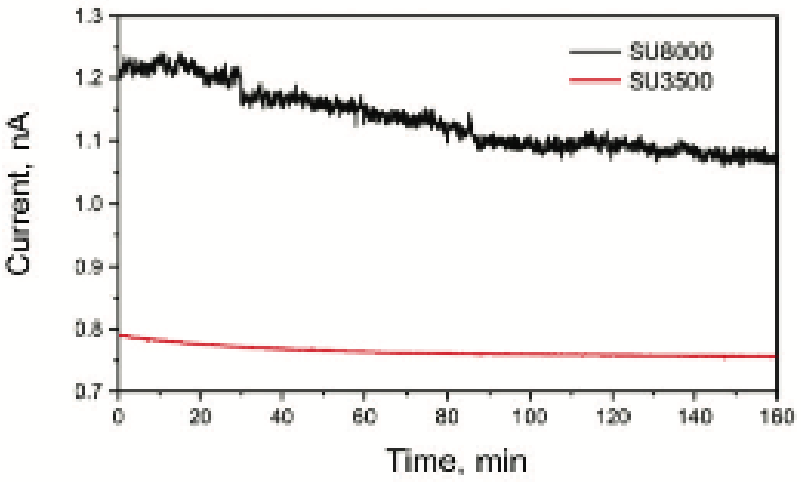

Figure 5.3 Time-dependent beam current measured on CFE versus tungsten SEM.

Calibration factors with PE standards (Mg, Al, and Zn) calculated with the two SEMs at 20 kV (Zn K-lines and L-lines) are listed in Table 5.2. When PE standards are used, accurate measurements of the beam current during the standard acquisitions are required in order to ensure the corresponding simulation has the same electron dose. Even though Figure 5.3 shows a poor stability of the CFE beam current in a long period, the acquisition time on each standard is only around 5 min. Hence, there is no obvious change of the beam current during the acquisitions of the three standards: the beam current of the Hitachi SU-8000 was around 370 nA, and that of the SU-3500 was around 470 nA, indicating the beam current can be accurately measured during the standards acquisitions, even with CFE-SEM.

Table 5.2 Calibration factors for Mg-Al-Zn system with PE standards at 20 kV.

Instrument	$\frac{\Lambda_{Al}}{\Lambda_{Mg}}$	$\frac{\Lambda_{Zn-K}}{\Lambda_{Mg}}$	$\frac{\Lambda_{Zn-L}}{\Lambda_{Mg}}$	$\frac{\Lambda_{Zn-K}}{\Lambda_{Al}}$	$\frac{\Lambda_{Zn-L}}{\Lambda_{Al}}$
SU-8000	0.958	0.790	2.419	0.824	2.524
SU-3500	0.964	0.831	2.473	0.863	2.564

Theoretically, all the calibration factors should be equal to 1 if the simulation is accurate enough. As shown in Table 5.2, $\frac{\Lambda_{Al}}{\Lambda_{Mg}}$ is close to 1, indicating that simulations of Mg K-lines and Al K-lines intensities are consistent with the experiments, but calibration factors for Zn L-line data are far from unity. The challenges of using transition element L-lines in X-ray quantitative analysis have been well studied (Armstrong & Crispin, 2012; Statham & Holland, 2014). For the experiments, the L-lines have multiple subshells, thus, the accurate measurement and extraction of experimental intensities is difficult. Regarding the simulation, the lack of reliable X-ray generation parameters for L-lines also affects the simulation accuracy. Additionally, the Coster-Kronig effect, which affects the emission of L-lines, is also not calculated in the MC X-ray program. All these factors make it more difficult to compute with L-lines than K-lines.

5.5.1.2 The *f*-ratio quantification

The EDS area spectra at a low magnification (500×) were acquired on the Mg_{45}-Al_{28}-Zn_{27} alloy with the two SEMs and quantified by the *f*-ratio method to investigate the influence of beam current (the results are listed in Table 5.3). The acquisitions were performed at 20 kV, and the calibration factors listed in Table 5.2 were used for the calculations. Both Zn K-lines and L-lines were used, and the results of Zn K-lines are much closer to the reference values. Furthermore, even though the experimental parameters and the calibration factors vary with the instruments, no significant difference in the quantification results is observed between the two SEMs. Thus, the

beam current stability does not influence the quantification results, and the calibration factors calculated with the respective instrument are necessary.

Table 5.3 Quantification results calculated by the *f*-ratio method[1, 2].

	SU-8000			SU-3500		
	Mg	Al	Zn	Mg	Al	Zn
20kV (Zn K-lines)	44.55% ± 0.34%	27.68% ± 0.38%	27.77% ± 0.04%	44.99% ± 0.15%	27.98% ± 0.13%	27.04% ± 0.28%
20kV (Zn L-lines)	46.25% ± 0.26%	29.41% ± 0.31%	24.34% ± 0.05%	45.96% ± 0.18%	29.82% ± 0.15%	24.22% ± 0.33%

1. The quantification results are normalized.
2. Reference composition measured by ICP-AES: 44.74 wt.% Mg, 27.76 wt.% Al, and 27.50 wt.% Zn.

As mentioned above, the beam current was measured during the acquisitions on the standards. Different from the traditional *k*-ratio method, which uses the beam current to correct the ratio of X-ray intensities between the unknown specimen and the standards, the *f*-ratio method uses the beam current to ensure the simulation is performed with the same electron dose as the experiment. Once the calibration factors are determined, all the quantifications afterwards are independent of the beam current. Thus, the *f*-ratio method is suitable for a long-time acquisition even with an unstable beam current, such as the quantitative X-ray mapping with a CFE-SEM.

The *f*-ratio quantitative map requires the same computation processes for each pixel in a map, so a high count-rate or a long acquisition time is necessary for a precise quantification. The computed *f*-ratio quantitative maps and the phase map are shown in Figure 5.4. The φ phase, τ phase, and matrix are identified in the phase map. Recent studies show that the φ phase and the τ phase with chemical formulae of $Mg_{21}(Al, Zn)_{17}$ and $Mg_{32}(Al, Zn)_{49}$ are the two main ternary phases in a Mg-Al-Zn system (Bergman et al., 1957; Bourgeois et al., 2001; Montagné & Tillard, 2016). In the two phases, Zn and Al atoms can substitute in the lattice without a fixed stoichiometric ratio (Feng & Ma, 2007).

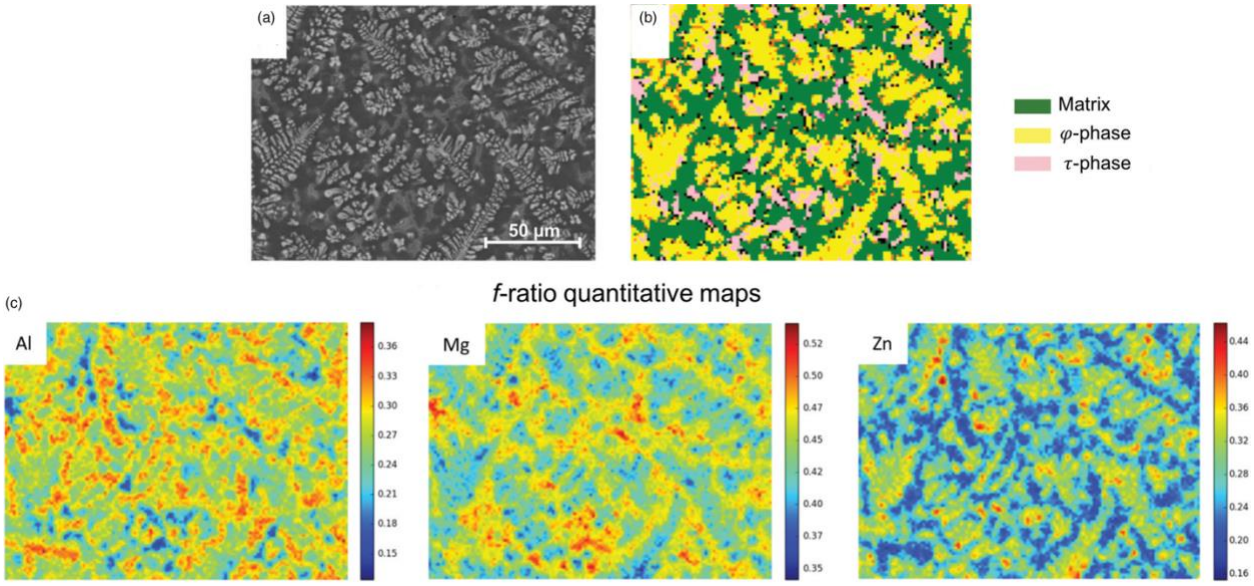

Figure 5.4 The *f*-ratio quantitative maps and phase map on the Mg_{45}-Al_{28}-Zn_{27} sample at 20 kV. (a) BSE image; (b) phase map processed by Python scripts; and (c) *f*-ratio standard-based quantitative X-ray maps.

In order to study the composition of each phase, the quantitative analyses were performed at a higher magnification. Figure 5.5 shows BSE images of the Mg_{45}-Al_{28}-Zn_{27} sample captured using the Hitachi SU-8000 at 30 kV [Figure 5.5(a)] and 5 kV [Figure 5.5(b)] at an on-screen magnification of 5k×. The phase circled in red observed at 30 kV becomes invisible at a lower accelerating voltage (5 kV), revealing a 3D structure formed during casting. Due to the fact that X-rays have a larger interaction volume than backscatter electrons, when EDS point analyses are performed at different positions on one phase shown in a BSE image, the collected X-ray counts may be excited from the phases hidden deeper below the observed ones, and the obtained compositions may have variations. Thus, a point analysis at a lower voltage is preferred to ensure a single phase is analyzed. Figure 5.5(c) illustrates the ranges (depth) of the BSE counts and the emitted characteristic X-ray counts of the three constituent elements at 30 and 5 kV simulated with the average composition (44.74 wt.% Mg, 27.76 wt.% Al, and 27.50 wt.% Zn). This is only an

estimation of the interaction volume inside this sample as the real ranges vary with the phase composition.

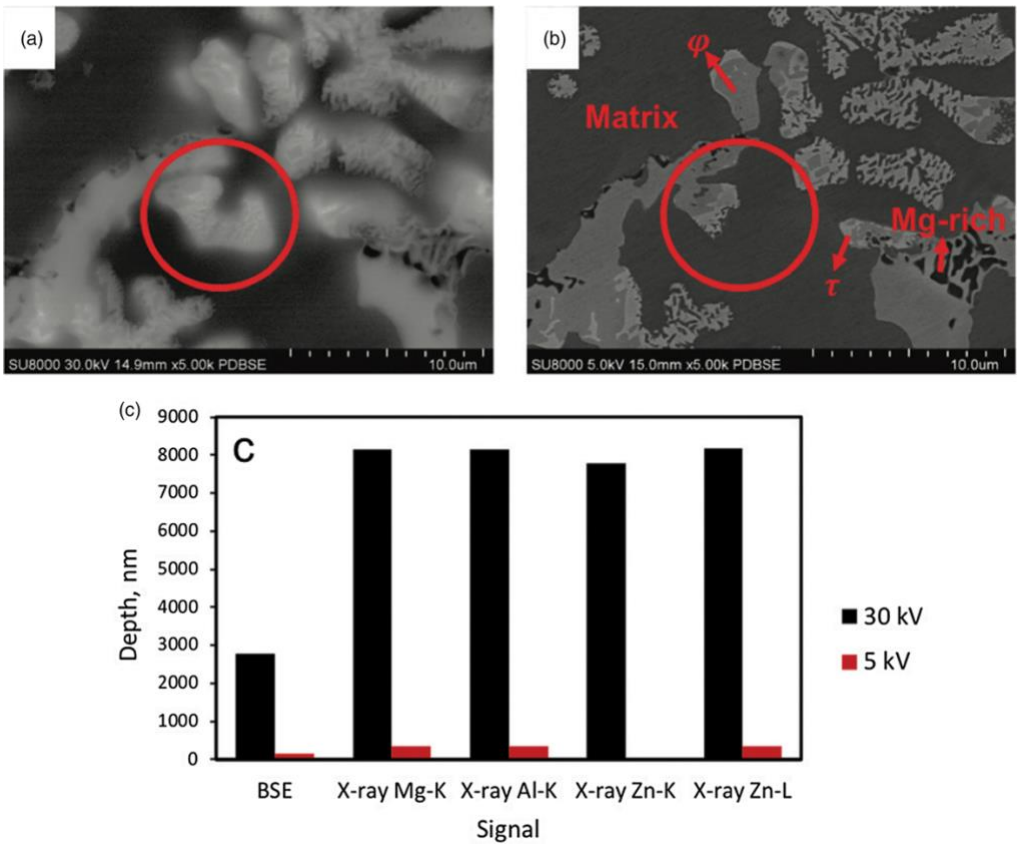

Figure 5.5 BSE images of the Mg_{45}-Al_{28}-Zn_{27} sample at 30 kV (a) and 5 kV (b) at a magnification of 5k× captured by the CFE-SEM Hitachi SU-8000. (c) The ranges (depth) of the BSE counts and the emitted characteristic X-ray counts at 30 and 5 kV.

As shown in Figure 5.5(b), except for the three phases labeled in the phase map [(Figure 5.4(b)], a Mg-rich phase is also identified at a higher magnification. Table 5.4 lists the compositions of the four phases quantified with the *f*-ratio method at 5 kV and the calculated formulae of the φ and τ phases. Compared with the ideal chemical formulae, the measured formula of the φ phase shows a good consistency, but a larger difference is observed on the τ phase. With the composition of each phase, the average composition of this sample (areas at a magnification

of 500×) was calculated coupled with each phase abundance, and the calculation result is displayed in the last row in Table 5.4. Since the Mg-rich phases are hard to identify at a low magnification, the calculations of the phase abundance are influenced, and around 5 wt.% error is obtained relative to the ICP-AES result.

Table 5.4 Compositions of phases in the Mg_{45}-Al_{28}-Zn_{27} sample calculated with the *f*-ratio method[1].

	Weight Fraction			Calculated formula
Phase	Mg (%)	Al (%)	Zn (%)	
φ phase $Mg_{21}(Al, Zn)_{17}$	40.93	19.26	39.81	$Mg_{21}(Al, Zn)_{16.5}$
τ phase ($Mg_{32}(Al, Zn)_{49}$)	29.69	24.04	46.27	$Mg_{32}(Al, Zn)_{42.0}$
Matrix	47.65	32.09	20.26	--
Mg-rich	86.51	6.56	6.93	--
Bulk composition (calculated)	42.60	25.29	32.11	--

1. Reference composition measured by ICP-AES: 44.74 wt.% Mg, 27.76 wt.% Al, and 27.50 wt.% Zn.

5.5.1.3 Comparisons with other quantitative techniques

In order to validate the *f*-ratio method, the quantification results were compared with other quantitative techniques, as shown in Figure 5.6. The labels on the y-axis are the quantification methods, where "std *f*-ratio" and "stdless *f*-ratio" refer to the *f*-ratio method corrected and not corrected with the calibration factors; "std EDS" and "stdless EDS" refer to the standard-based and standardless EDS analyses performed by the software coupled with the respective spectrometer (INCA for the Hitachi SU-8000 and Aztec for the Hitachi SU-3500); "DTSA-II" refers to the standard-based *k*-ratio method performed by DTSA-II software. Only spectra acquired by the Hitachi SU-8000 were analyzed by DTSA-II software, and only Zn K-lines were used for the analyses. Additionally, the EPMA/WDS results are also shown in Figure 5.6.

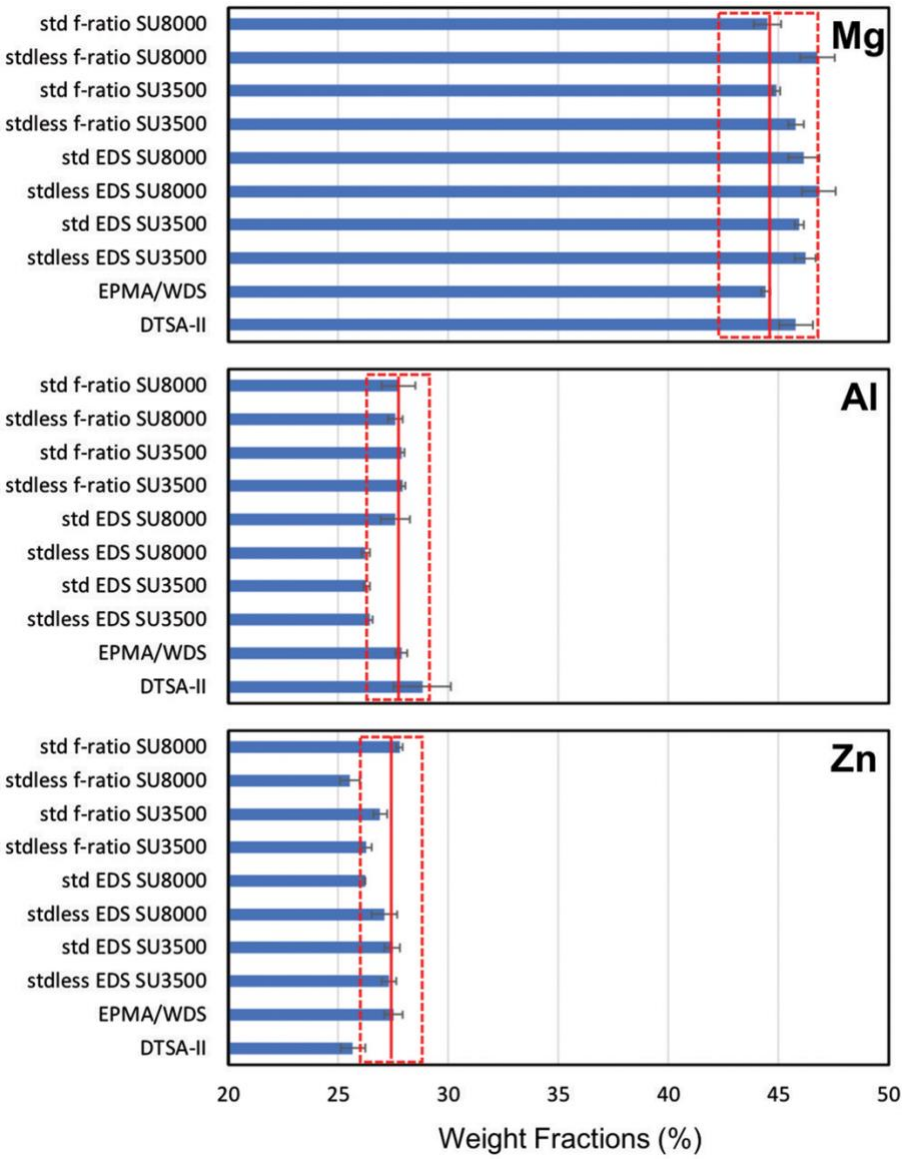

Figure 5.6 Quantification results of the Mg_{45}-Al_{28}-Zn_{27} sample.

The reference values are labeled as the red lines in this figure, and the red dash lines indicate the ranges within a relative error of 5%, which is considered as an acceptable accuracy for major constituents (Newbury & Ritchie, 2015). From Figure 5.6, it can be concluded that: (1) the EPMA/WDS provides values close to the references as expected; (2) the two SEMs do not show significant differences in the *f*-ratio quantification; (3) the calibrated *f*-ratio method with standard samples gives results closer to the reference values compared with the standardless *f*-ratio,

indicating the calibration factors can effectively improve the accuracy of this quantification method.

5.5.2 Line scan analyses on Mg-Al-Zn diffusion alloy

5.5.2.1 Calibration factors

As global analyses of the Mg_{45}-Al_{28}-Zn_{27} sample produce a consistent composition, this sample was used as a standard to calculate the calibration factors. It is a risk to acquire an area spectrum on a multiphase sample as a standard spectrum since the ZAF factors vary with the phase composition. The right way to calculate the X-ray emission is to sum the contribution of the ZAF factors at each phase. However, the abundances of phases are difficult to accurately calculate at a low magnification, which would introduce more errors into the calculation. According to the previous discussions, the average bulk composition of the Mg_{45}-Al_{28}-Zn_{27} alloy was calculated with area spectra, as listed in Table 5.3, and was also calculated with the composition and abundance of each phase, as listed in the last row in Table 5.4, but the former results are closer to the reference values. Thus, area spectra were acquired on this alloy to estimate the overall X-ray emission and calculate the calibration factors.

In order to validate the use of the Mg_{45}-Al_{28}-Zn_{27} sample as a standard, Table 5.5 compares the calibration factors calculated with this sample and the PE standards at 5 and 20 kV. Based on equations (5.2) and (5.6), the ratio of the PE-standard-based calibration factors of two elements should be theoretically equal to their compound-standard-based calibration factor, as equation (5.13):

$$\frac{\Lambda_B}{\Lambda_A} = \Lambda_{A-B} \tag{5.13}$$

As shown in Table 5.5, the results calculated with the two types of standards are very similar, but there are still tiny differences which may be caused by the heterogeneity of the Mg_{45}-Al_{28}-Zn_{27} sample. The *f*-ratio quantification results with the two types of standards will be discussed in the next section. Regarding the influence of the beam energy, Λ_{Mg-Al} at 5 kV is closer to 1 for the two types of standards. However, the calibration factors of Zn L-lines are significantly different from unity for both accelerating voltages.

Table 5.5 Calibration factors for the Mg-Al-Zn system.

Mg_{45}-Al_{28}-Zn_{27} standard					
	Λ_{Mg-Al}	Λ_{Mg-Zn}		Λ_{Al-Zn}	
		Λ_{Mg-ZnK}	Λ_{Mg-ZnL}	Λ_{Al-ZnK}	Λ_{Al-ZnL}
5 kV	0.972	--	2.692	--	2.771
20 kV	0.937	0.769	2.257	0.820	2.409
PE standards					
	$\frac{\Lambda_{Al}}{\Lambda_{Mg}}$	$\frac{\Lambda_{Zn-K}}{\Lambda_{Mg}}$	$\frac{\Lambda_{Zn-L}}{\Lambda_{Mg}}$	$\frac{\Lambda_{Zn-K}}{\Lambda_{Al}}$	$\frac{\Lambda_{Zn-L}}{\Lambda_{Al}}$
5 kV	0.988	--	2.726	--	2.759
20 kV	0.958	0.790	2.419	0.824	2.524

In order to further explore the interactions between the three elements, the ZAF factors in the Mg_{45}-Al_{28}-Zn_{27} alloy were calculated by DTSA-II software with the PE standards at 5 and 20 kV using the following equation (Ritchie, 2011b), as listed in Table 5.6.

$$C_A = \frac{(ZAF)_{un}}{(ZAF)_{std}} \cdot k_A \tag{5.14}$$

Comparing the *A*-factors of Al Kα and Mg Kα, a larger amount of Al Kα radiation was absorbed in the specimen. According to the calculation of Λ_{Mg-Al} [equation (5.9)], either the underestimation of I_{Mg}^{th} or the overestimation of I_{Al}^{th} can cause Λ_{Mg-Al} to be smaller than 1.

Regarding the *F*-factors of Mg Kα, additional 0.5% of Mg Kα radiation at 20 kV and 0.3% at 5 kV were produced by the fluorescence effect, which was not calculated in the MC X-ray program, resulting in the underestimation of I_{Mg}^{th}. Additionally, since I_{Mg}^{th} was underestimated more at the higher accelerating voltage, a larger divergence of Λ_{Mg-Al} from unity is observed at 20 kV.

Table 5.6 ZAF factors of Mg_{45}-Al_{28}-Zn_{27} sample calculated by DTSA-II software.

	Mg Kα-line			Al Kα-line			Zn Kα-lines			Zn Lα-lines		
	Z_{Mg}	A_{Mg}	F_{Mg}	Z_{Al}	A_{Al}	F_{Al}	Z_{Zn}	A_{Zn}	F_{Zn}	Z_{Zn}	A_{Zn}	F_{Zn}
5 kV	1.082	0.889	1.003	1.039	0.843	1.000	--	--	--	0.828	1.050	1.006
20 kV	1.056	0.402	1.005	1.019	0.274	1.000	0.862	1.003	1.000	--	--	--
	1.056	0.421	1.005	1.019	0.288	1.000	--	--	--	0.886	1.282	1.011

As shown in Table 5.6, the *F*-factors of the most characteristic X-ray lines are very close to 1.0, except for Zn Lα at 20 kV with an effect of 1.1% (F_{Zn} = 1.011). The L-ionization edges of Zn range from 1.034 to 1.208 keV, which are slightly lower than the energy of Mg Kα (1.253 keV). Thus, Mg K-lines were absorbed by the Zn atom, and an additional amount of Zn L-lines counts was produced by the fluorescence effect. Thus, Zn K-lines are preferred when both K-lines and L-lines are available for calculation.

5.5.2.2 Quantification results

A line scan analysis across the Mg-Al-Zn ternary phases [Figure 5.7(a) and 5.7(b)] on the diffusion alloy was performed at 20 kV. The *f*-ratio quantification results calibrated by the PE standards and the Mg_{45}-Al_{28}-Zn_{27} alloy are both shown in Figure 5.7(c) (Zn K-lines were used). The two types of standards produced very similar results. Three distinct phases are observed based on the compositional contrast in the BSE images and the quantification results: one φ phase [$Mg_{21}(Al, Zn)_{17}$] and two τ phases [$Mg_{32}(Al, Zn)_{49}$]. The interaction volume of X-ray counts is

around 3 μm with the compositions shown in Figure 5.7(c) at 20 kV, so smooth compositional variations are observed near the interfaces.

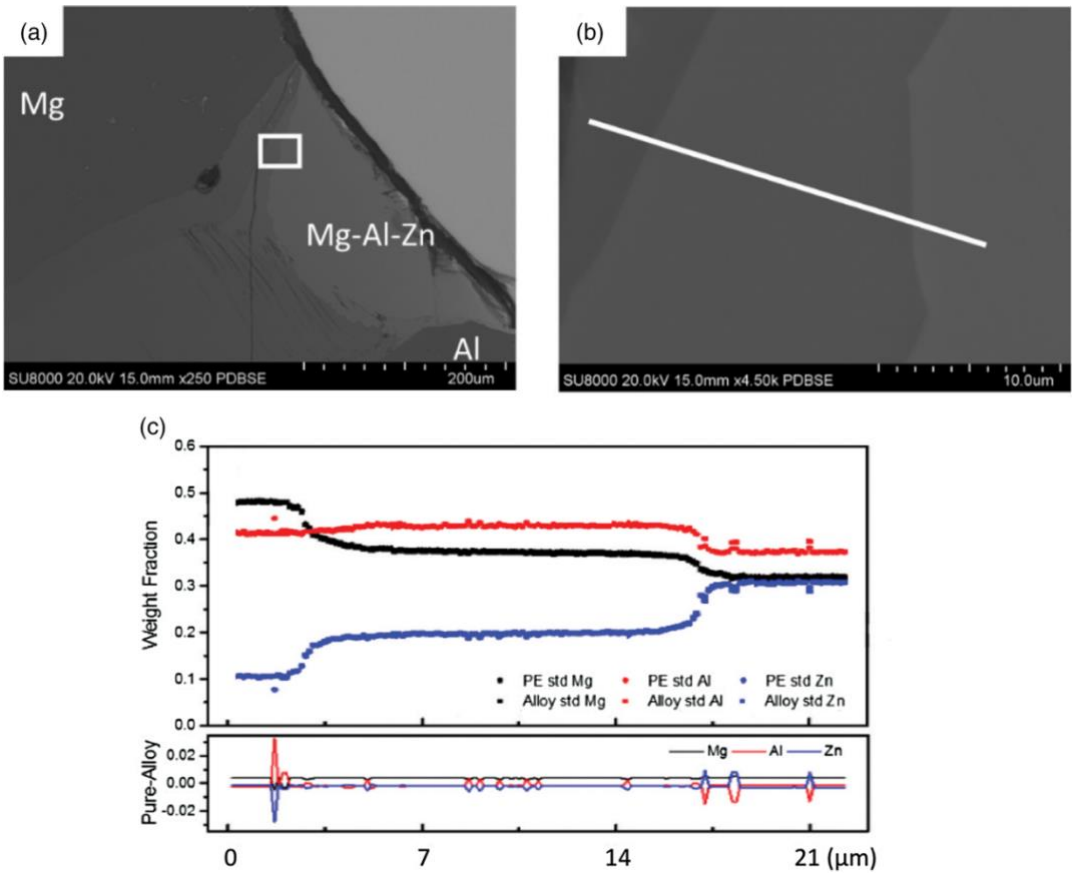

Figure 5.7 Line scan analysis on the diffusion Mg-Al-Zn alloy with the *f*-ratio method at 20 kV. (a) BSE image; (b) enlarged BSE image of the framed area in (a); and (c) weight fractions of Mg, Al, and Zn calculated with the PE standards and the alloy standard. The differences between the two sets of calculations are also shown.

The net differences between the two sets of calculations are also shown in Figure 5.7(c). Differences less than 4 wt.% are observed between the calculations with the two types of standards, and the large differences mainly concentrate at phase interfaces. At the phase boundary, the X-ray absorption cannot be correctly calculated, this thus leads to an inaccurate simulation. Also, the interface may not be flat enough and the X-ray counts collection could be affected. Except for the

exceptions at the interfaces, the general differences fall within 1 wt.%, indicating that both the PE standards and the alloy standard can be used to calibrate the simulated *f*-ratios.

In order to validate the *f*-ratio method at different accelerating voltages, the line scan analysis was also performed at 5 kV at the same region. The previous study has reported that a beam-energy-dependent calibration factor provides a higher *f*-ratio quantification accuracy than a constant one (Horny et al., 2010), so the respective calibration factors at 5 kV (listed in Table 5.5) were used. Figure 5.8 compares the *f*-ratio quantification results (with the PE standards and with the alloy standard) at different accelerating voltages (5 and 20 kV) and with different X-ray lines (Zn K-lines and Zn L-lines), and the result of Zn K-lines at 20 kV was considered as the reference composition. Except for the *f*-ratio method, the same comparisons of the EDS standardless analysis and the standard-based *k*-ratio method performed by DTSA-II software are also shown in this figure.

Regarding the quantifications at different accelerating voltages, differences within 2 wt.% are observed for the *f*-ratio method [black columns in Figures 5.8(b) and 5.8(c)] and DTSA-II software [black columns in Figure 5.8(d)], which are relatively smaller than the standardless analysis [black columns in Figure 5.8(a)]. Regarding the results calculated with Zn K-lines and L-lines at 20 kV (red columns in Figure 5.8), differences within 1 wt.% are observed for all the quantitative techniques. It can be concluded that the *f*-ratio method and DTSA-II software have a better consistency with different X-ray lines at various accelerating voltages relative to the EDS standardless analysis.

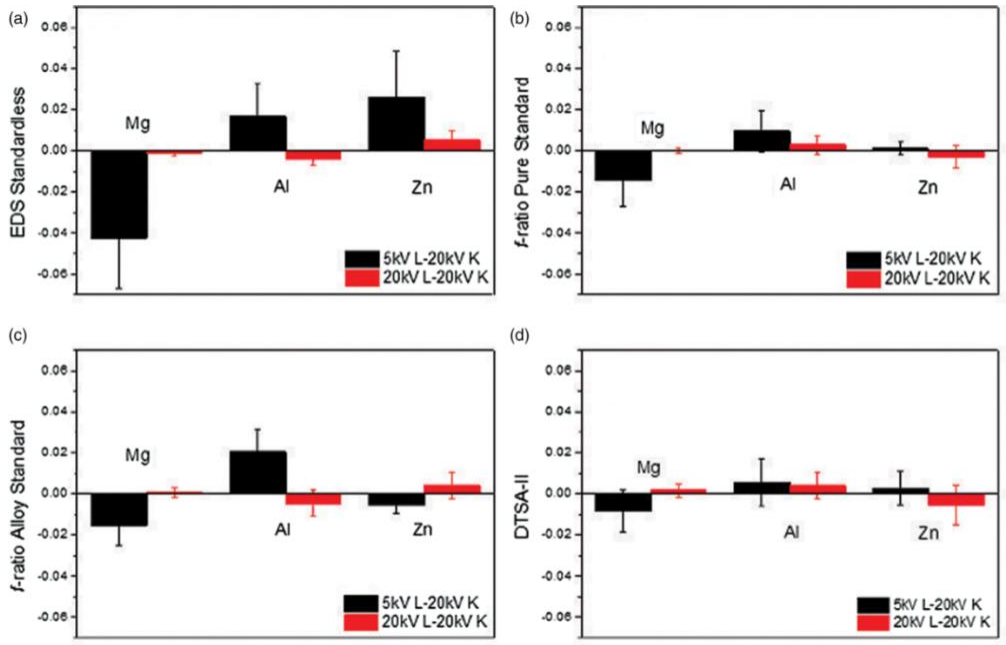

Figure 5.8 Comparisons of the quantification results on the Mg-Al-Zn diffusion alloy at 5 kV (black bars) and 20 kV (red bars). (a) The EDS standardless analysis; (b) the *f*-ratio method calibrated with the PE standards; (c) the *f*-ratio method calibrated with the alloy standard; and (d) the standard-based *k*-ratio method performed by DTSA-II software.

Figure 5.9 shows the comparisons between the different quantification techniques to study the accuracy of the *f*-ratio method, where the DTSA-II results were considered as the reference values at 5 and 20 kV respectively. Differences within 2 wt.% are observed at 5 kV and within 1 wt.% at 20 kV between the *f*-ratio method and DTSA-II. In contrast, larger differences are observed for the EDS standardless analysis versus the DTSA-II results. Thus, the *f*-ratio method and the DTSA-II software can produce similar quantification results at different accelerating voltages.

Compared with the routine EDS standardless analysis, the *f*-ratio method is a type of standard-based computation and exhibits a better accuracy over the range of the used accelerating voltages. Compared to the standard-based *k*-ratio method, the *f*-ratio method only needs standards to calibrate the differences between experiments and simulations. If calibration factors are already

determined for an instrument at a certain accelerating voltage, standard samples are no longer required. Thus, a database incorporating all the elements can be built for a set of instruments, and the standard-based quantification can be achieved without a real standard.

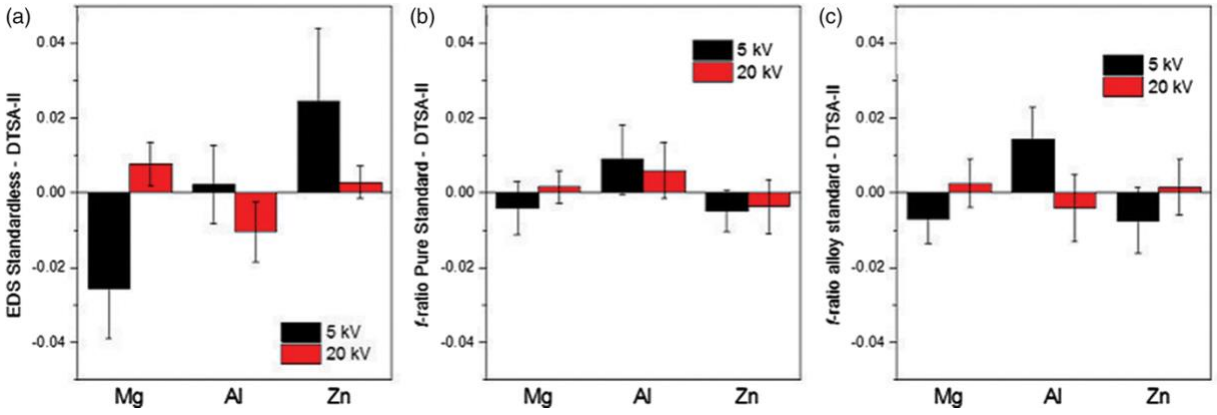

Figure 5.9 Comparisons of the quantification results between different techniques with DTSA-II on the Mg-Al-Zn diffusion alloy at 5 kV (black bars) and 20 kV (red bars). (a) EDS standardless analysis; (b) the *f*-ratio method calibrated with the PE standards; and (c) the *f*-ratio method calibrated with the alloy standard.

5.6 Conclusion

The *f*-ratio method is an effective and efficient approach to perform standard-based quantitative analyses on multi-element systems. It combines EDS experiments and Monte Carlo simulations, and calibration factors are required to evaluate the differences between them. The beam-energy-dependent calibration factors, which need to be determined for each instrument, can effectively improve the *f*-ratio quantification accuracy. When elements L-lines and K-lines are both available for the analysis, K-lines are preferred due to the inaccurate simulations and multiple

subshells of L-lines. PEs and compounds can be both used as standards. When PE standards are used, the beam current needs to be correctly measured. However, no obvious influences of the beam current stability are observed on the *f*-ratio quantification results, indicating that the *f*-ratio method can be applied to any type of electron microscope. This feature is typically beneficial for quantitative X-ray mapping with a long-time acquisition or an unstable beam current.

Chapter 6

The *f*-ratio Quantification Method Applied to Standard Minerals with a Cold Field Emission SEM/EDS

In Chapter 5, the PE-standard-based *f*-ratio quantification method was applied to Mg-Al-Zn systems. However, as a new quantification method, it still requires extensive validations to be performed in more complex systems. In this chapter, the *f*-ratio method was performed on three standard mineral specimens [kyanite (Al_2SiO_5), albite ($NaAlSi_3O_8$), and orthoclase ($KAlSi_3O_8$)], and the option of standards was extended to any standard specimen containing the target elements. The impacts of the beam energy and standard composition on the quantification results are investigated.

- This chapter has been published as: Teng, C.*, Yuan, Y. & Gauvin, R. (2019). The *f*-ratio Quantification Method Applied to Standard Minerals with a Cold Field Emission SEM/EDS. *Talanta* **204**, 213-223. doi:10.1016/j.talanta.2019.05.107.

6.1 Abstract

The *f*-ratio method is a standard-based quantification method which was originally developed based on a cold field emission scanning electron microscope/energy dispersive spectroscopy (CFE-SEM/EDS) system. It incorporates traditional EDS experiments and Monte Carlo simulations, and standards with known compositions are needed to calibrate the differences between them. However, as a new quantification method, the *f*-ratio method still requires extensive validations to be performed in different systems. In this study, the *f*-ratio method was used to analyze three certified minerals: kyanite (Al_2SiO_5), albite ($NaAlSi_3O_8$) and orthoclase ($KAlSi_3O_8$), and the option of standards was extended to any standard specimen containing the target elements. The effects of standards and beam energies on the calibration factors and the quantification results were discussed, and no significant influence was observed. The quantification results were also compared with the conventional standardless analysis and the standard-based *k*-ratio method, and the results show the *f*-ratio method is capable to achieve both the merits of a satisfactory accuracy and simple experimental procedures.

6.2 Introduction

The scanning electron microscope/energy dispersive spectroscopy (SEM/EDS) system is popular for X-ray microanalysis due to its simple and fast operation. The EDS quantitative analysis performed with the standard-based *k*-ratio method (Castaing, 1951) is capable to reach the comparable accuracy and precision with the wavelength dispersive spectrometry (WDS) (Ritchie et al., 2012). In order to eliminate the needs of real standards and measurements of electron dose, the standardless analysis has emerged, but the trade-off is the quantification accuracy (Newbury et al., 1995; Newbury & Ritchie, 2013b). Under these circumstances, the *f*-ratio method, which combines both the merits of simple experimental procedures and an improved accuracy, was developed as an alternative to the traditional standard-based *k*-ratio method (Horny et al., 2010; Teng et al., 2019).

One distinctive feature of the *f*-ratio method is it combines the conventional EDS acquisition and the Monte Carlo simulation. Equation (6.1) shows the definition of the *f*-ratio with the experimental characteristic X-ray intensities (I_i^{exp}) or the theoretically simulated intensities (I_i^{th}) in a multi-element system:

$$f_i = \frac{I_i^{exp}}{\sum I_i^{exp}} = \frac{I_i^{th}}{I_i^{th} + \sum_{j \neq i} \Lambda_{i-j} I_i^{th}} \tag{6.1}$$

where Λ_{i-j} represents the calibration factor between any two elements, which is calculated with a standard having the known composition. This method was firstly applied to a set of binary Cu-Au alloys [SRM 482, from National Institute of Standards and Technology (NIST) standards mounted by Geller MicroÅnalytical Laboratory Inc., Boston, MA, USA], using a 60 wt.% Cu - 40 wt.% Au alloy as the standard (Horny et al., 2010). The use of a compound standard containing all the target

elements enables the whole quantification process to be independent of the beam current, but such a proper standard becomes difficult to find when the number of constituent elements increases. And then, the use of pure-element (PE) standards was investigated in the ternary Mg-Al-Zn systems, and a good consistency is obtained between the PE-standard-based quantification results and the compound-standard-based (Teng et al., 2019). So far, the limited applications of the *f*-ratio method all give a satisfactory accuracy less than 5 % with beam-energy-dependent calibration factors (Horny et al., 2010; Teng et al., 2019).

However, as a new quantification method, the *f*-ratio method still requires extensive validations to be performed in more complex systems. In this study, this method was performed on three standard mineral specimens [kyanite (Al_2SiO_5), albite ($NaAlSi_3O_8$), and orthoclase ($KAlSi_3O_8$)], and the option of standards was extended to any standard specimen containing the target elements. The quantification results were discussed in terms of the standards compositions and the accelerating voltages, and were compared with those of the conventional standardless analysis and the standard-based *k*-ratio method.

6.3 Materials and Experimental Methods

6.3.1 Specimens

The certified compositions of the standard mineral specimens: kyanite (Al_2SiO_5), albite ($NaAlSi_3O_8$) and orthoclase ($KAlSi_3O_8$) (Geller MicroÅnalytical Laboratory Inc., Boston, MA,

USA) are listed in Table 6.1. Even though the orthoclase has a theoretical formula of $KAlSi_3O_8$, a trace element Na (~ 2 wt.%) was detected in this specimen. Table 6.2 lists the standards used for the standard-based *k*-ratio and *f*-ratio quantitative analyses of the above three specimens.

Table 6.1 Reference compositions of the specimens studied in this work.

	Weight Fraction				
	O	Na	Al	Si	K
Al_2SiO_5	0.4937	--	0.333	0.1733	--
$NaAlSi_3O_8$	0.4876	0.0876	0.1027	0.3207	--
$KAlSi_3O_8$	0.4626	0.0195	0.0990	0.3035	0.1061

Table 6.2 Standards used for the *k*-ratio and the *f*-ratio analyses.

	The *k*-ratio method				The *f*-ratio method			
	Na	Al	Si	K	Na	Al	Si	K
Al_2SiO_5[a]	--	Pure Al[b]	Pure Si[b]	--	--	Pure Al[b]	Pure Si[b]	--
					--	$NaAlSi_3O_8$[a]		--
					--	$KAlSi_3O_8$[a]		--
					--	$CaAl_2Si_2O_8$[a]		--
$NaAlSi_3O_8$[a]	NaF[a]	--	--	--	NaF[a]	Pure Al[b]	Pure Si[b]	--
					NaF[a]	Al_2SiO_5[a]		--
					NaF[a]	$KAlSi_3O_8$[a]		--
					NaF[a]	$CaAl_2Si_2O_8$[a]		--
$KAlSi_3O_8$[a]	--	--	--	KCl[a]	NaF[a]	Pure Al[b]	Pure Si[b]	KCl[a]
					NaF[a]	Al_2SiO_5[a]		KCl[a]
						$NaAlSi_3O_8$[a]		KCl[a]
					NaF[a]	$NaAlSi_3O_8$[a]		KCl[a]
					NaF[a]	$CaAl_2Si_2O_8$[a]		KCl[a]

a. from Geller MicroÅnalytical Laboratory Inc., Boston, MA, USA
b. from SPI Supplies Inc., West Chester, PA, USA

6.3.2 SEM/EDS characterization

The observation was performed with a Hitachi SU-8000 CFE-SEM (Hitachi High-Technologies, Rexdale, ON, Canada), and the EDS X-ray microanalysis was performed using an 80 mm^2 silicon drift detector (Oxford Instruments, Abingdon, Oxfordshire, UK) controlled by an

INCA software (version 4.15) (Oxford Instruments, Abingdon, Oxfordshire, UK). 10 EDS point-acquisitions with a live time of 300 s at 10 kV, 15 kV, and 20 kV, and 200 s at 25 kV and 30 kV were performend on each specimen. The INCA software was calibrated before the acuquisitions at each beam energy in order to correctly measure the X-ray intensities. The spectrum acquisitions were performed 3 hours after the flashing to obtain a relatively stable beam current. The beam current was measured by a Faraday cup with a NanoPico picoammeter (Hitachi High-Technologies, Rexdale, ON, Canada) before and after each point acquisition and the average value is used to estimate the electron dose during the whole acquisition. The applied quantification techniques include the *f*-ratio method, the standardless and standard-based analysis performed by the INCA software (version 4.15) attached with the spectrometer, and the standard-based *k*-ratio method performed by the DTSA-II software (version Jupiter 2017-11-06) (Ritchie, 2011a; 2011b). For all the standard-based analyses, the concentrations of O were calculated by stoichiometry.

6.3.3 The *f*-ratio method

The *f*-ratio method couples traditional EDS experiments and Monte Carlo simulations using a calibration factor, which is computed through performing the experiments and simulations on a standard with known composition. Equation (6.2) shows a binary standard as an example:

$$f_A^{exp} = \frac{I_A^{exp}}{I_A^{exp} + I_B^{exp}} = \frac{I_A^{th}}{I_A^{th} + \Lambda_{A-B} I_B^{th}} \tag{6.2}$$

where I_A^{exp} and I_B^{exp} are the experimentally measured characteristic X-ray intensities, and I_A^{th} and I_B^{th} are the theoretically simulated ones. Thus, the calibration factor can be determined as:

$$\Lambda_{A-B} = \frac{I_A^{th}}{I_B^{th}} \frac{I_B^{exp}}{I_A^{exp}} \tag{6.3}$$

Since I_A^{exp} and I_B^{exp} are from one spectrum, as well as I_A^{th} and I_B^{th}, the calibration factor is independent of the beam current. However, when PE standards are used for the two elements, the calibration factor should be calculated for each element respectively:

$$\Lambda_A = \frac{I_A^{exp}}{I_A^{th}} \tag{6.4}$$

And thus, equations (6.2) and (6.3) should be rewritten as:

$$f_A^{exp} = \frac{I_A^{exp}}{I_A^{exp}+I_B^{exp}} = \frac{\Lambda_A I_A^{th}}{\Lambda_A I_A^{th}+\Lambda_B I_B^{th}} = \frac{I_A^{th}}{I_A^{th}+\frac{\Lambda_B}{\Lambda_A} I_B^{th}} \tag{6.5}$$

$$\Lambda_{A-B,PE} = \frac{\Lambda_B}{\Lambda_A} = \frac{\frac{I_B^{exp}}{I_B^{th}}}{\frac{I_A^{exp}}{I_A^{th}}} \tag{6.6}$$

In equation (6.6), I_A^{exp} and I_B^{exp} (I_A^{th} and I_B^{th}) are not from the same spectrum, so the beam current and the acquisition time should be measured during their acquisitions, aiming to ensure I_A^{exp} and I_A^{th} (I_B^{exp} and I_B^{th}) have the same electron dose (Teng et al., 2019). In this study, the choice of standards is not limited to a compound standard or PE standards (as shown in Table 6.2) but extended to any combination of separate standards containing the target elements. In this case, the calculation procedures are similar with those using PE standards.

In this study, the MC X-ray program (version 1.6.4) (Guavin & Michaud, 2009) and the DTSA-II software (version Jupiter 2017-11-06) (Ritchie, 2009; 2011a) were both used to perform the simulations of the standards to calculate the calibration factors. The settings of the detector

models in the two programs were different: for the MC X-ray, most of the detector parameters were the default settings as it was originally designed for the SEM used in this work; but for the DTSA-II, a user-defined detector model was associated by importing a real EDS spectrum acquired by the simulated detector (Ritchie, 2009). Regarding the simulations on the X-ray generation and emission, the models used in the two techniques are listed in Table 6.3, and more details of the simulations can be found in the references (Guavin, 2005; Ritchie, 2009).

Table 6.3 Models for X-ray emission in the MC X-ray and the DTSA-II programs.

	MC X-ray	DTSA-II
Electron Energy Loss	Bethe (Bethe et al., 1938)	Bethe (Bethe et al., 1938)
Mean Ionization Potential	Joy & Luo (Joy & Luo, 1989)	Joy & Luo (Joy & Luo, 1989)
Electron Cross Section	Mott (Czyżewski et al., 1990) & Browning (Browning et al., 1994)	NIST Electron Elastic-Scattering Cross-Section database (version 4.0) (Powell et al., 2016)
Mass Absorption Coefficients	Chantler (Chantler, 1995; 2000)	Chantler (Chantler, 1995; 2000)
Characteristic X-ray Cross Section	Casnati (Casnati et al., 1982)	Bote & Salvat (Bote & Salvat, 2008)
Bremsstrahlung X-ray Cross Section	Kirkpatrick & Wiedman (Kirkpatrick & Wiedmann, 1945)	Seltzer & Berger (Seltzer & Berger, 1986)

The *f*-ratio quantification works by performing simulations on the target system to build the relationship between the system composition and its elemental *f*-ratios. In this study, the simulations of the O-Al-Si, O-Na-Al-Si, and O-Na-Al-Si-K systems were performed with the MC X-ray program to apply the *f*-ratio analyses on the kyanite, albite, and orthoclase specimens, respectively. A Python script was used to execute the simulations, which involves changing the target composition, setting the simulation condition (e.g., physical models for the X-ray emission, microscope parameters, etc.), and collecting the simulated intensities. The step size of the compositional change in the simulation determines the precision of the quantification results, but

also affects the simulation efficiency. In this study, the step size was set at 2 at.% for the O-Al-Si system and 5 at.% for the O-Na-Al-Si and the O-Na-Al-Si-K systems.

After the simulations, the theoretical *f*-ratios were calibrated with the calibration factors calculated by the MC X-ray program. Taking the *f*-ratios in the O-Al-Si system as examples:

$$f_{Al} = \frac{I_{Al,K}}{I_{Al,K}+\Lambda_{Al-Si}I_{Si,K}+\Lambda_{Al-O}I_{O,K}} \tag{6.7}$$

$$f_{Si} = \frac{I_{Si,K}}{I_{Si,K}+\Lambda_{Si-Al}I_{Al,K}+\Lambda_{Si-O}I_{O,K}} \tag{6.8}$$

$$f_O = \frac{I_{O,K}}{I_{O,K}+\Lambda_{O-Al}I_{Al,K}+\Lambda_{O-Si}I_{Si,K}} = \frac{I_{O,K}}{I_{O,K}+\frac{1}{\Lambda_{Al-O}}I_{Al,K}+\frac{1}{\Lambda_{Si-O}}I_{Si,K}} = 1 - f_{Al} - f_{Si} \tag{6.9}$$

However, when pure Al and pure Si were used as standards, only Λ_{Al-Si} was calculated as there was no standard used for O. Thus, only f_{Al} and f_{Si} were calibrated as in a binary system:

$$f_{Al} = \frac{I_{Al,K}}{I_{Al}+\Lambda_{Al-Si}I_{Si}} \tag{6.10}$$

$$f_{Si} = \frac{I_{Si,K}}{I_{Si,K}+\Lambda_{Si-Al}I_{Al,K}} = \frac{I_{Si,K}}{I_{Si,K}+\frac{1}{\Lambda_{Al-Si}}I_{Al,K}} = 1 - f_{Al} \tag{6.11}$$

Similar computations were also performed on the O-Na-Al-Si and the O-Na-Al-Si-K systems, and the K-line X-ray intensities of the constituent elements were used. Due to the poor energy resolution in an EDS spectrum, the calculation employed the sum radiation of the K-shell (e.g., $I_{Al,K}$ represents the sum intensities of Kα and Kβ) to avoid errors introduced by deconvolution.

In this way, the system compositions are associated with the calibrated *f*-ratios, and this relation could be used to find the composition of the unknown specimen. To obtain the

quantification results, the experimental *f*-ratios of the target specimens were measured by routine EDS acquisitions, and the corresponding compositions were interpolated by a Python script. The experimental procedure is the same as a standardless analysis without a need to measure the beam current.

6.4 Results

6.4.1 Quantification on the kyanite specimen (Al_2SiO_5)

In order to perform the *f*-ratio quantitative analysis on the kyanite specimen (Al_2SiO_5), the O-Al-Si system was calibrated with the calibration factors of Λ_{Al-Si}, Λ_{Al-O}, and Λ_{Si-O}. The PE standards (pure Al and pure Si) and the compound standards [kyanite (Al_2SiO_5), albite ($NaAlSi_3O_8$), orthoclase ($KAlSi_3O_8$), and anorthite ($CaAl_2Si_2O_8$)] were used to compute the calibration factors, and calculation results are illustrated in Figure 6.1 [(a) Λ_{Al-Si}, (b) Λ_{Al-O}, and (c) Λ_{Si-O}]. The computations were conducted at the accelerating voltages of 10 kV, 15 kV, 20 kV, 25 kV, and 30 kV (represented by the color dots), and simulations were performed with the MC X-ray (top graphs) and DTSA-II (middle graphs) programs. The bottom graphs illustrate the average differences between the calibration factors computed with the two programs.

As shown in Figure 6.1, the calibration factors are composition-dependent. The $NaAlSi_3O_8$ and the $KAlSi_3O_8$ have the same atomic fractions of the three target elements, so the similar factors were calculated with them, especially for Λ_{Al-Si}. Regarding the beam energy effect, the calibration

factors calculated with the PE standards have a poorer stability on the beam energy compared with the other compound standards [Figure 6.1(a)]. For the differences between the MC X-ray and the DTSA-II programs, Λ_{Al-Si} fluctuate around 0 with all standards, indicating a good consistency between the two programs, but wide gaps are observed on calibrating O K-line intensity, revealing the issues in the simulations of O radiation.

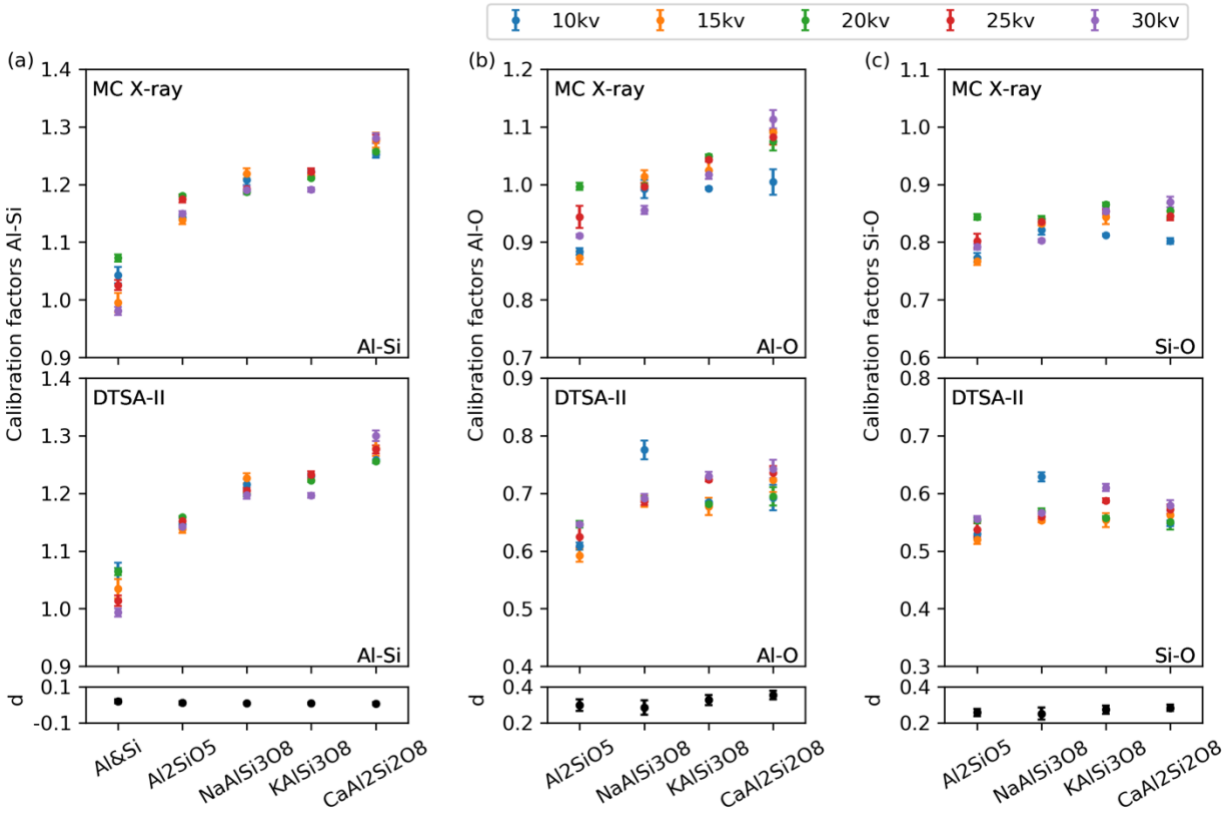

Figure 6.1 Calibration factors in the O-Al-Si system. (a) Λ_{Al-Si}; (b) Λ_{Al-O}; and (c) Λ_{Si-O}.

With the related calibration factors, the simulated X-ray intensities in the O-Al-Si system were calibrated at the corresponding beam energy, and the quantification results of the kyanite specimen are shown in Figure 6.2. Except for the *f*-ratio method with different standards, the results of standardless (labelled as EDS stdless) and standard-based (labelled as EDS std) EDS analyses performed by the INCA software, and the standard-based *k*-ratio method performed by the DTSA-

II software (labelled as DTSA-II) are also shown in this figure. The black solid lines indicate the reference concentrations of the three elements, and the dashed squares indicate the ranges within a relative error of ± 5 %, which is considered as the acceptable accuracy for major constituents (Newbury & Ritchie, 2015).

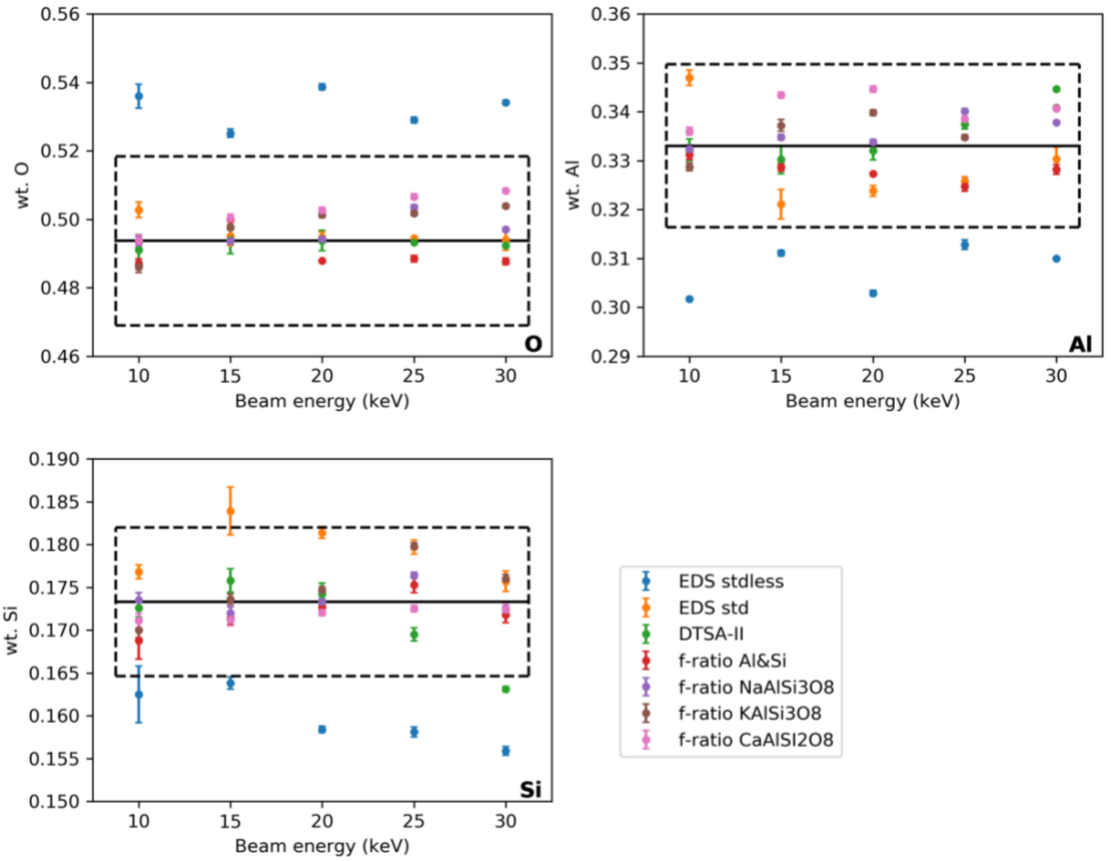

Figure 6.2 Quantification results of the kyanite specimen with the beam-energy-dependent calibration factors.

The quantification results confirm that the standard-based analysis, including both the *k*-ratio method and the *f*-ratio method, can provide a higher accuracy vs. the standardless analysis. Regarding the *f*-ratio method, even though the calibration factors vary with the standard composition, the quantification results are little influenced by standards. Since the beam-energy-

dependent calibration factors are used, there is no obvious beam energy effect on the quantification results.

However, Figure 6.1 shows that the calibration factors do not significantly vary with the beam energy in most cases, so the average value at all the beam energies was calculated for each standard. The *f*-ratio quantification results with the constant factors are illustrated in Figure 6.3. As shown in this figure, except for the PE-standard-based computations (red dots), other quantification results all have a satisfactory accuracy. However, the PE-standard-based computation is a special case where the O-related calibration factors are missing, which causes the system not fully calibrated.

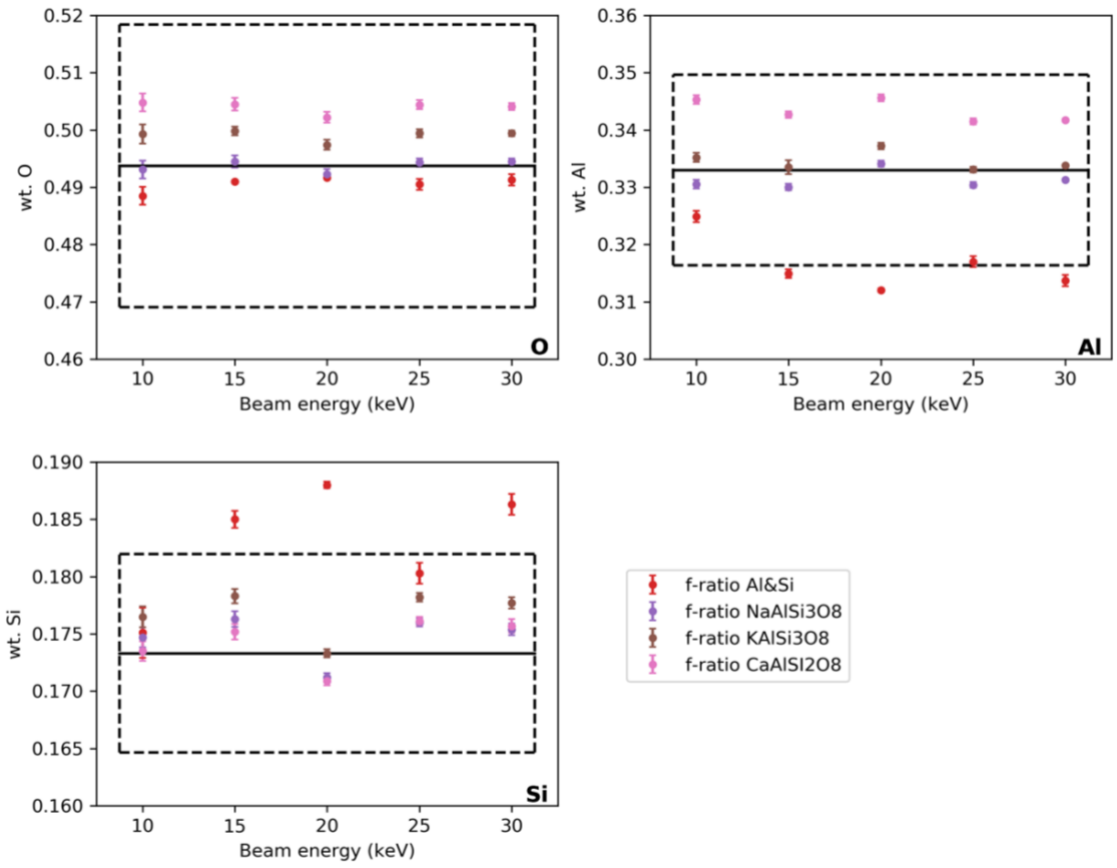

Figure 6.3 Quantification results of the kyanite specimen with the constant calibration factors.

6.4.2 Quantification on the albite specimen ($NaAlSi_3O_8$)

In order to perform the *f*-ratio quantitative analysis on the albite specimen ($NaAlSi_3O_8$), the calibration factors in the O-Na-Al-Si system were calculated. The Na-related calibration factors are shown in Figure 6.4, including Λ_{Na-Al} (a), Λ_{Na-Si} (b), and Λ_{Na-O}(c). All the standards used to calibrate the O-Al-Si system in the previous section were also used here to calibrate the three elements, and a standard NaF specimen was used for Na. In order to investigate the influence of the standard type, the $NaAlSi_3O_8$ was also considered as a compound standard to calculate the Na-related calibration factors, and the results are shown in Figure 6.4(d).

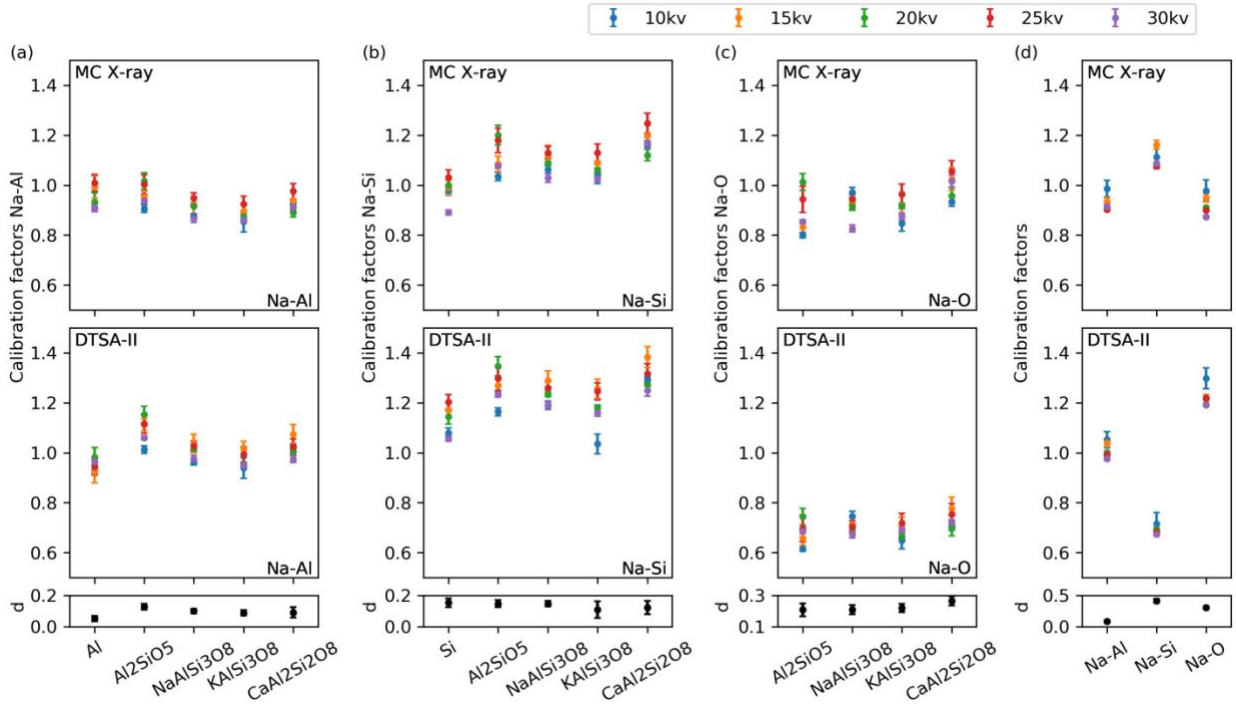

Figure 6.4 Na-related calibration factors in the O-Na-Al-Si system. (a) - (c) Separate standards for Λ_{Na-Al} (a), Λ_{Na-Si} (b), and Λ_{Na-O} (c); and (d) a compound standard for all Na-related factors.

As shown in Figure 6.4, the calibration factors are dependent on the standard composition and the beam energy. Comparing the same factors calculated with the separate standards [Figures

6.4(a) - 6.4(c)] and the compound standard Figure 6.4(d), the compound-standard-based calibration factors have a better stability over the range of the beam energies applied (all the graphs are illustrated with the same y-scale). Regarding the comparisons between the MC X-ray and the DTSA-II programs, the largest differences also occur at the O K-line intensity calibration.

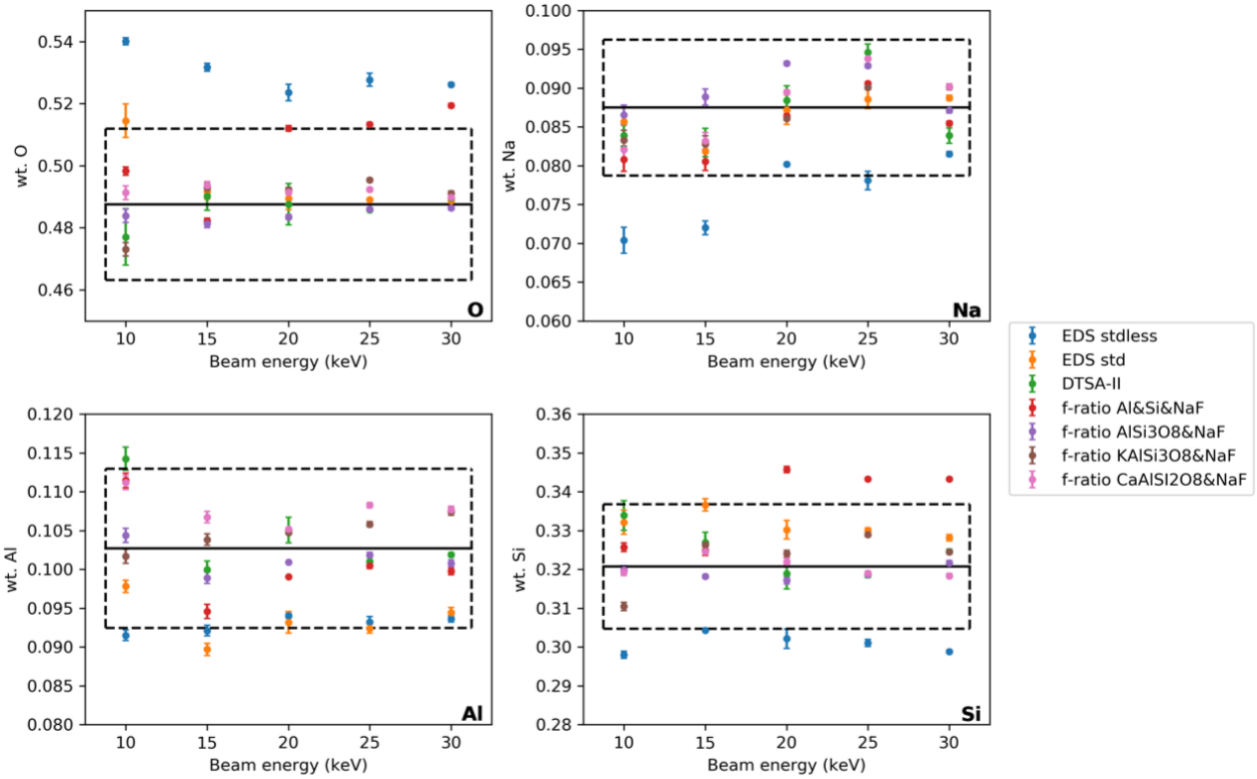

Figure 6.5 Quantification results of the albite specimen with the beam-energy-dependent calibration factors.

With the calibration factors, the intensities simulated in the O-Na-Al-Si system were calibrated, and the *f*-ratio analyses were performed on the albite specimen. Figure 6.5 shows the *f*-ratio results computed with the beam-energy-dependent calibration factors, and Figure 6.6 shows the results computed with a constant calibration factor for each standard. As the reference concentrations of Na and Al are below or around 10 wt.%, their acceptable accuracy is considered

as ± 10 %, but that of O and Si is still ± 5 % (Newbury & Ritchie, 2015). As shown in the two figures, either with the beam-energy-dependent calibration factors (Figure 6.5) or the constant ones (Figure 6.6), most of the *f*-ratio results fall into the acceptable range, except for the cases when no standard was used for O (red dots in the two figures).

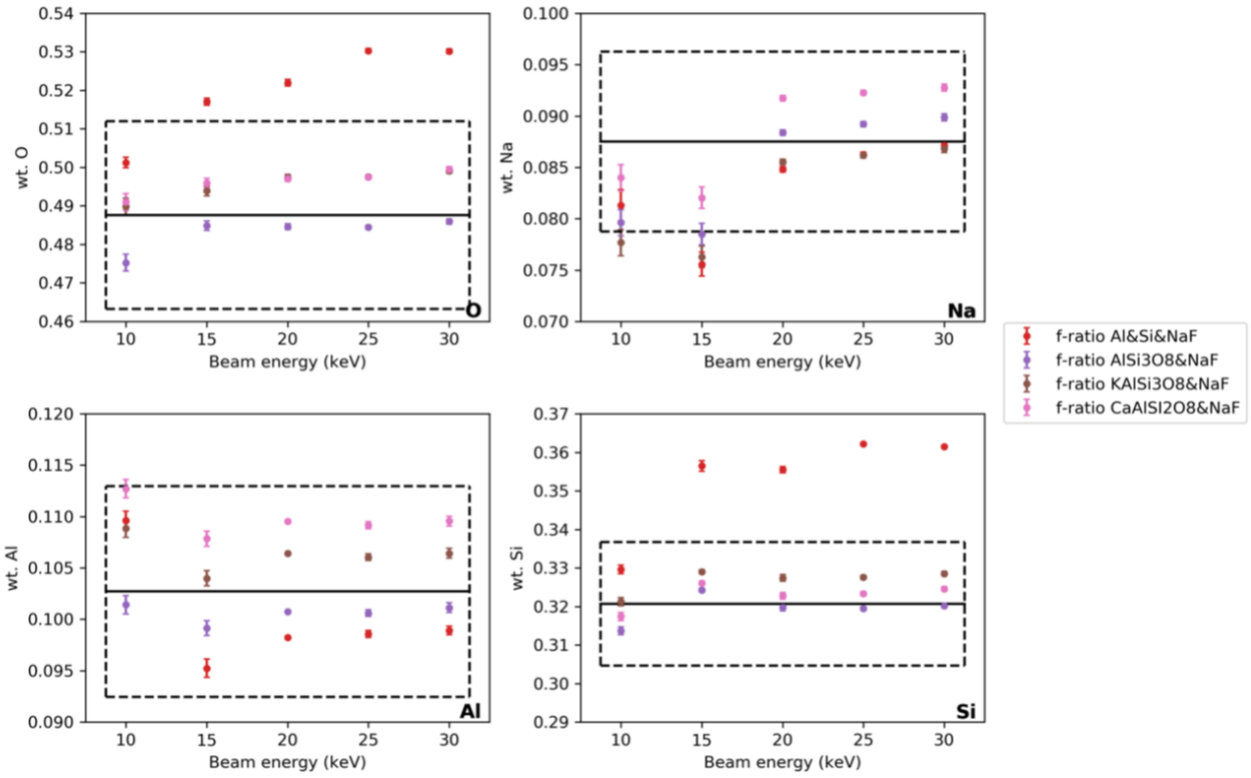

Figure 6.6 Quantification results of the albite specimen with the constant calibration factors.

6.4.3 Quantification on the orthoclase specimen ($KAlSi_3O_8$)

To perform the *f*-ratio quantification method on the orthoclase specimen, the simulated intensities in the O-Na-Al-Si-K system were calibrated with the relevant calibration factors. All the standards used to calibrate the O-Al-Si system in the previous sections were also used here to

calibrate the three elements, NaF and $NaAlSi_3O_8$ were used for Na, and a standard KCl specimen was used for K. The calculation results of the K-related calibration factors are shown in Figure 6.7, including Λ_{K-Al} (a), Λ_{K-Si} (b), Λ_{K-O} (c), and Λ_{Na-K} (d), which again confirm that the calibration factors are influenced by the standard composition and the beam energy. Additionally, the MC X-ray and the DTSA-II programs have different performances on calibrating O K-line intensity.

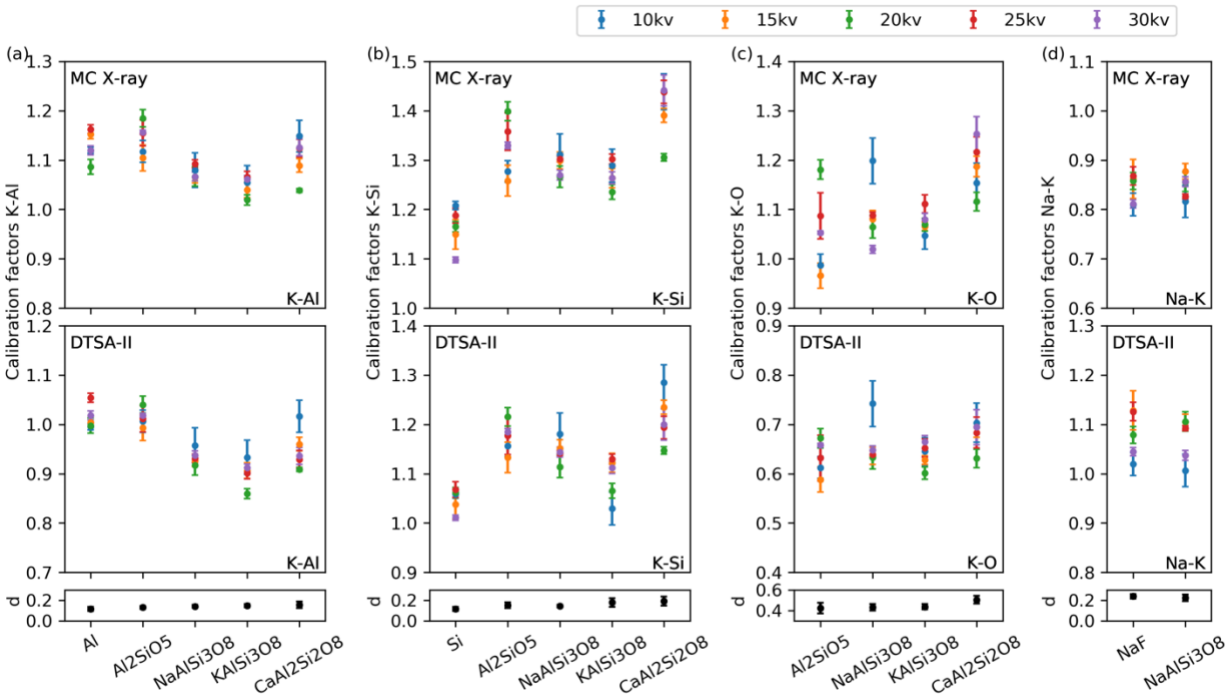

Figure 6.7 K-related calibration factors in the O-Na-Al-Si-K system. (a) Λ_{K-Al}; (b) Λ_{K-Si}; (c) Λ_{K-O}; and (d) Λ_{Na-K}.

With different combinations of the standards, the *f*-ratio quantification results of the orthoclase specimen are shown in Figure 6.8 (with the beam-energy-dependent calibration factors) and Figure 6.9 (with the constant calibration factors). Even though the $NaAlSi_3O_8$ and the NaF generated similar results of Λ_{Na-K} [Figure 6.7(d)], the NaF was used as the main standard due to its simpler chemical composition. As the reference concentrations of Na, Al, and K are below or

around 10 wt.%, their acceptable accuracy is considered as ± 10 %, but those of O and Si are still ± 5 %.

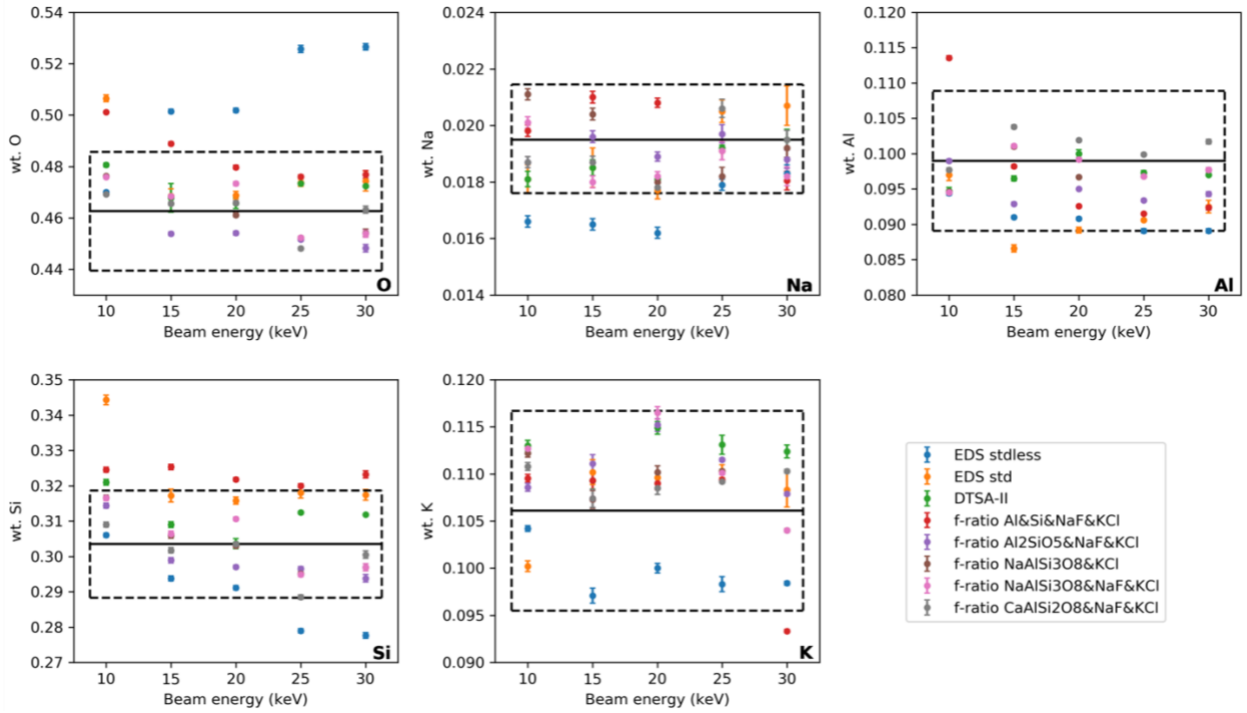

Figure 6.8 Quantification results of the orthoclase specimen with the beam-energy-dependent calibration factors.

As shown in Figure 6.8, all the standard-based quantitative analyses have a higher accuracy vs. the standardless analysis. Regarding the *f*-ratio results computed with the beam-energy-dependent calibration factors, most of them have the acceptable accuracy, except for the cases where no standard was used for O (red dots). The *f*-ratio analyses of the albite specimen also have the similar issue, but such an issue does not occur in the analyses of the kyanite, which triggers the speculation that the complexity of the target system will influence the quantification accuracy. Additionally, regarding the *f*-ratio analyses with the constant calibration factors (Figure 6.9), the beam energy effect is more significant than that on the other two simpler specimens. The overall

deviations from the accurate ranges of Na at 15 kV and 20 kV, Al at 10 kV, and K at 10 kV are observed.

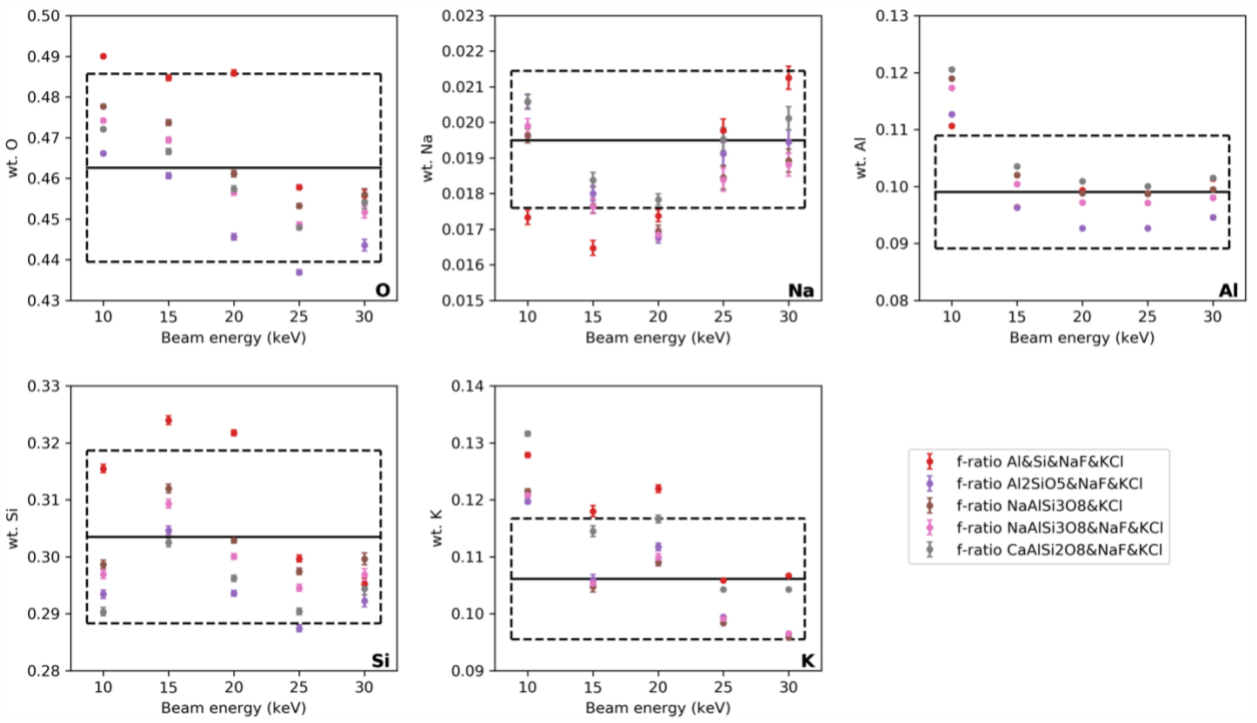

Figure 6.9 Quantification results of the orthoclase specimen with the constant calibration factors.

6.5 Discussion

6.5.1 Calibration factors

The computation of the calibration factors is a crucial step to perform an accurate *f*-ratio quantification. In this work, the effects of the standard type on the calibration factors were studied, and the standard option was extended to any combination of separate standards which contain the

target elements. When a compound standard was used, e.g., in Figure 6.1 where Al_2SiO_5, $NaAlSi_3O_8$, $KAlSi_3O_8$, and $CaAl_2Si_2O_8$ were used to calculate the calibration factors in the O-Al-Si system, and in Figure 6.4(d) where $NaAlSi_3O_8$ was used to calculate the Na-related factors, the beam current effects were eliminated. However, when several separate standards were used, the electron dose was still required to be measured during their experimental acquisitions.

The reasons for the dependence of the calibration factors on the standard composition and the beam energy can be both attributed to the inaccurate calculations of the mass absorption coefficients. Regarding the composition-dependence, it is also an issue in the standard-based *k*-ratio method, which prefers to use the standards having similar chemical constituents with the target specimen to achieve a more accurate quantification (Ritchie et al., 2012). However, in the *f*-ratio method, it is difficult to predict the effects of an individual calibration factor on the final quantification results, as multiple calibration factors are used to calibrate the target system intensities. Regarding the beam-energy-dependence, a compound-standard-based calibration factor has a better stability on the accelerating voltages than a separate-standard-based one, according to the comparisons of Λ_{Al-Si} illustrated in Figure 6.1(a), and the Na-related calibration factors shown in Figure 6.4. However, the poor stability of the separated standards may also result from the unstable beam current of the cold field emission, which makes it difficult to keep the electron dose exactly the same for the simulations and experiments.

The calibration factors computed by the MC X-ray and the DTSA-II programs are compared, and their differences can be explained by the applied models for simulating X-ray emission and detection. Regarding the X-ray emission, the MC X-ray and the DTSA-II programs used the Casnati equation (Casnati et al., 1982) and the Bote-Salvat equation (Bote & Salvat, 2008)

to compute the X-ray cross section, respectively. The two models have been thoroughly compared in Gauvin's work (Gauvin, 2012), but determining their relative accuracy is still difficult due to the huge uncertainties in the related experimental measurements. Additionally, the MC X-ray program does not incorporate the secondary fluorescence into the X-ray emission simulation as it is negligible in most analytical cases, but it is calculated in the DTSA-II simulations (Ritchie, 2017). Regarding the X-ray detection, the window type used in the simulations decides the function of the detector efficiency on the photon energy (Goldstein et al., 2017). The window model used in the DTSA-II software was Moxtek AP 3.3, but the detector efficiency in the MC X-ray program was calculated by manually setting the window layers and accumulating the contribution of absorption from each layer. However, some basic parameters (e.g., the thickness of the window) are difficult to be accurately measured. Thus, the calibration factor is strongly dependent on the applied instruments and the simulation settings.

Theoretically, a calibration factor should equal 1 if the simulation and the experiment have a good consistency, but divergences from unity are observed, especially for the O-related factors calculated by the DTSA-II. Inaccurate calculations of the detector efficiency for low energy X-ray lines and the poor knowledge of fluorescence yield both influence the computations of the theoretical O K-line intensity (Newbury, 2002; Ritchie, 2009). Table 6.4 lists the proportions of O radiations generated by the fluorescence effect (the characteristic fluorescence and bremsstrahlung fluorescence) in all the O-contained specimens at different accelerating voltages, which were calculated with the DTSA-II software. As shown in this table, the fluorescence effect becomes stronger with increasing the beam energy, but the maximum amount of O K-line intensity excited by it is still below 0.3 %. Thus, the fluorescence effect on the calibration factors is very small, and the detector efficiency plays a more important role on simulating O radiations.

Table 6.4 The proportions of O K-line radiations generated by secondary fluorescence.

	Characteristic Fluorescence					Bremsstrahlung Fluorescence				
	10 kV	15 kV	20 kV	25 kV	30 kV	10 kV	15 kV	20 kV	25 kV	30 kV
Al_2SiO_5	0.06%	0.10%	0.14%	0.18%	0.21%	0.04%	0.04%	0.04%	0.05%	0.05%
$NaAlSi_3O_8$	0.07%	0.11%	0.15%	0.18%	0.19%	0.04%	0.04%	0.04%	0.05%	0.05%
$KAlSi_3O_8$	0.04%	0.08%	0.11%	0.14%	0.16%	0.04%	0.04%	0.04%	0.05%	0.05%
$CaAl_2Si_2O_8$	0.04%	0.07%	0.10%	0.12%	0.14%	0.04%	0.04%	0.04%	0.05%	0.05%

6.5.2 Quantification results

Regarding the standard influences on the *f*-ratio quantification results, the standard type plays a more significant role compared with the standard composition. The difference between a compound standard and a combination of separate standards is the need to measure the beam current, whose variations may introduce errors into the quantification results. Among the three analyzed specimens, only the analyses of the kyanite employed the compound standards, and all the relevant quantification results have the acceptable accuracy, either with the beam-energy-dependent calibration factors (Figure 6.2) or with the constant ones (Figure 6.3).

Among the combinations of separate standards, there is one special case when no standard was used for calibrating O intensity, such as when the pure Al, the pure Si were used for the kyanite (red dots in Figures 6.2 and 6.3), when the pure Al, the pure Si, and the NaF were used for the albite (red dots in Figures 6.5 and 6.6), and when the pure Al, the pure Si, the NaF and the KCl were used for the orthoclase (red dots in Figures 6.8 and 6.9). It is common not to use a standard for O in the standard-based *k*-ratio method as the experimental measurement of O K-line intensity is still problematic, but most of the *f*-ratio results without an O standard cannot produce a desirable accuracy. That is because the *f*-ratio method requires the simulations to be performed on the entire

system and the system intensities to be fully calibrated. Thus, a missing of any standard can cause an overall miscalibration.

Additionally, with the increase of the number of the constituent elements, it is becoming more difficult to obtain consistent quantification results when the standards and the beam energy are changed, e.g., more variations are observed on the quantification results of the orthoclase compared to the other two simpler specimens. The rising possibilities of the unreliable simulations of the elemental interaction and the inaccurate experimental measurements of a complex system can introduce more uncertainties into the quantification results. This point is further confirmed by the *f*-ratio quantification results using the constant calibration factors: the results of the kyanite (Figure 6.3) and the albite (Figure 6.6) with the fully calibrated systems have a satisfactory accuracy, but those of the orthoclase (Figure 6.9) show a strong dependence on the beam energy.

One important superiority of the standard-based *k*-ratio method over the standardless analysis is the unnormalized result, which can reveal any misidentification of constituents or deviation in experimental conditions (e.g., surface roughness, specimen geometry) (Newbury & Ritchie, 2015). However, the result normalization is also inevitable in the *f*-ratio method at this stage due to the normalized input composition into the simulation. In this study, the O concentration was further calculated by stoichiometry after the interpolations, and the analytical total of all the constituents covers 99 % - 101 % for the kyanite, 99 % - 102 % for the albite, and 98 % - 103 % for the orthoclase. The tiny ranges around unity indicate the original interpolation results also have a good accuracy. Since the *f*-ratio method requires an overall system simulation before the analysis of the unknown specimen, the correct identification of constituents is a significant premise of an accurate quantification. Furthermore, the unknown specimen should have

a similar surface topography with the standards, otherwise the calibration factors cannot accurately calibrate the X-ray detections. Thus, the accurate element identification and the careful specimen preparation are the prerequisites to the *f*-ratio quantification method.

One original motivation to develop the *f*-ratio method is to eliminate the beam current influences on the quantification process, especially for the analyses performed with a cold field emission SEM, which has an unstable beam current and is not suitable for the *k*-ratio method. The use of a compound standard can easily achieve this, but when separate standards are used, the measurements of the beam current are still required during their experimental acquisitions. However, once the calibration factor is determined, the following quantification process is independent of the beam current, and the experimental procedures are the same as the standardless analysis. In addition, the calibration factors are reusable for one set of instruments, as long as the devices for collecting X-ray counts (e.g., EDS detector) and the software for counting X-ray intensities remain unchanged.

6.6 Conclusion

In this work, the *f*-ratio quantification method was applied to the kyanite (Al_2SiO_5), the albite ($NaAlSi_3O_8$) and the orthoclase ($KAlSi_3O_8$) specimens with various standards and at different accelerating voltages. A compound standard or several separate standards were both used to calculate the calibration factors, which are dependent on the standard composition and the beam energy. Through the comparisons between the calibration factors calculated with the MC X-ray

and DTSA-II programs, it is concluded that the calibration factors are strongly dependent on the instrument parameters and the simulation settings.

With a fully calibrated system, the *f*-ratio quantification method can own a satisfactory accuracy with either a compound standard or several separate standards. It is difficult to predict the quantification results based on an individual calibration factor, and a missing of any standard can cause an overall system miscalibration. Furthermore, with the increase of the number of the constituent elements, it is becoming more difficult to obtain consistent quantification results with changing the standards and the beam energy. For a simpler system, such as the kyanite or the albite, the results calibrated with either the beam-energy-dependent calibration factors or the constant factors have a satisfactory accuracy; but for a more complex system, such as the orthoclase, the results show a strong dependence on the beam energy when the constant calibration factors were used.

Finally, even though the *f*-ratio method requires the accurate element identification and careful specimen preparation, it can own the similar accuracy and simpler experimental procedures compared with the standard-based *k*-ratio method.

Chapter 7

Concluding Remarks

Based on the results reported in Chapters 3-6, the conclusions, contributions to original knowledge and suggestions for future work are presented in this chapter.

7.1 Conclusions

The Chapters 3 & 4 describe the phase map analyses based on the traditional elemental X-ray mapping, and Chapters 5 & 6 focus on quantitative X-ray microanalyses performed with the recently developed *f*-ratio method in multi-element systems. The following conclusions are drawn:

1. The phase map analysis is a practical solution for characterizing samples having various phases and complicated elemental constituents. It can avoid the issues of excessive noise and clearly visualize the phase distribution.

2. The large solid angle of the aSDD contributes to efficient X-ray mapping at a low beam energy, where the improved spatial resolution enables an accurate phase identification down to one micron.

3. The processing time for acquiring X-ray counts has significant impacts on the collecting efficiency and the spectrum energy resolution, which should be chosen depending on a specific objective. A short processing time can achieve an efficient map acquisition but also cause limited energy resolution, so it is suitable for acquiring general phase information. On the other hand, a long processing time enables a remarkable energy resolution, which is required for an accurate peak identification in a spectrum having serious overlaps.

4. The performance of MSA on a phase map can significantly shorten the required acquisition time for the X-ray mapping. The PCA can be used to denoise a phase map, and the BSS is more helpful for phase separation and identification. Through the comparisons between the two popular BSS algorithms: ICA and NMF, the NMF is confirmed to be more suitable for an EDS map dataset.

5. The *f*-ratio quantification method was performed on several multi-element systems, including two Mg-Al-Zn alloys and three certified minerals [kyanite (Al_2SiO_5), albite ($NaAlSi_3O_8$) and orthoclase ($KAlSi_3O_8$)]. The quantification results with the beam-energy-dependent calibration factors have a satisfactory accuracy for both major and minor elements.

6. The use of PE standards was validated in the Mg-Al-Zn systems, and the use of a combination of separate standards was validated with the certified minerals. The beam current and the standard compositions do not show an obvious influence on the quantification results.

7. Since the *f*-ratio method is not sensitive to the beam current, it is suitable for quantitative X-ray mapping with long time acquisition and even with an unstable beam current.

8. Comparing with the widely applied standardless analysis and the traditional standard-based *k*-ratio method, the *f*-ratio method is capable to achieve both the merits of a satisfactory accuracy and simple experimental procedures.

7.2 Contributions to Original Knowledge

The contributions to original knowledge made during this study are summarized as follow:

1. This is the first study to calculate the elemental *f*-ratios to perform the phase map analysis, and this simplifies the phase identification with high flexibility.

2. This is the first study to couple the MSA with the phase map analysis to improve the analytical efficiency without sacrificing the accuracy of phase identification.

3. The previous studies on the *f*-ratio quantification method were limited in binary systems, so this study is the first time to perform the *f*-ratio method on multi-element systems.

4. This is the first study to use the interpolation method to obtain the *f*-ratio quantification results.

5. In the previous studies, the standard used in the *f*-ratio method was limited to a compound which contains all the target elements. This is the first study to extend the standard option to any standard having one or more target elements.

6. This is the first study to perform the quantitative X-ray mapping with the *f*-ratio method.

7.3 Suggestions for Future Work

Based on the studies presented in this thesis, suggestions for future work are given in the following:

1. An experimental database of the calibration factors could be built to simplify the future quantification procedures.

2. The recent *f*-ratio quantification procedure strongly relies on the simulations of the whole system, and this increases the preparation works before the analysis of the unknown specimen. Thus, the theoretical relation between the elemental *f*-ratio versus the target system

composition should be investigated. The *f*-ratio ought to be formularized with the elemental concentration and corresponding coefficients, with the expectation to reduce the necessary simulations and enhance the quantification efficiency.

3. The simulations of K-lines intensity exhibit a satisfactory consistency with the experiments, but those of L-lines and M-lines still need improvements. The databases involved in the computations of L-lines or M-lines X-ray emission, e.g., the mass absorption coefficient and the fluorescence correction, need further study.

4. The accuracy and precision of the *f*-ratio quantitative mapping performed on heterogeneous specimens need to be evaluated.

References

Alvisi, M., Blome, M., Griepentrog, M., Hodoroaba, V.-D., Karduck, P., Mostert, M., . . . Scholze, F. (2006). The determination of the efficiency of energy dispersive X-ray spectrometers by a new reference material. *Microscopy and Microanalysis* **12**(5), 406-415.

Anderson, C. & Hasler, M. (1966). Extension of electron microprobe techniques to biochemistry by the use of long wavelength X-rays. Paper presented at the Proceedings of *the Fourth International Conference on X-ray Optics and Microanalysis*, Castaing, R., Deschamps, P. & Philibert, J. (Eds.), pp. 310-327. Paris: Hermann.

Anderson, I., Bentley, J. & Carter, C. (1995). The secondary fluorescence correction for X-ray microanalysis in the analytical electron microscope. *Journal of Microscopy* **178(**3), 226-239.

Armstrong, J. & Crispin, K. (2012). Current limitations in the use of L-lines of first-row transition elements for quantitative EDS and WDS analysis of complex materials. *Microscopy and Microanalysis* **18**(S2), 1726-1727.

Barkshire, I., Karduck, P., Rehbach, W. P. & Richter, S. (2000). High-spatial-resolution low-energy electron beam X-ray microanalysis. *Microchimica Acta* **132**(2-4), 113-128.

Bastin, G., Dijkstra, J. & Heijligers, H. (1998). PROZA96: an improved matrix correction program for electron probe microanalysis, based on a double Gaussian φ (ρz) approach. *X-Ray Spectrometry* **27**(1), 3-10.

Bell, D. C. & Erdman, N. (2012). *Low voltage electron microscopy: principles and applications*: John Wiley & Sons.

Bergman, G., Waugh, J.L. & Pauling, L. (1957). The crystal structure of the metallic phase $Mg_{32}(Al, Zn)_{49}$. *Acta Crystallographica* **10**(4), 254-259.

Bethe, H., Rose, M. & Smith, L. (1938). The multiple scattering of electrons. In *the American Philosophical Society* **78**(4), 573-585.

Bosman, M., Watanabe, M., Alexander, D. & Keast, V. (2006). Mapping chemical and bonding information using multivariate analysis of electron energy-loss spectrum images. *Ultramicroscopy* **106**(11), 1024-1032.

Bote, D. & Salvat, F. (2008). Calculations of inner-shell ionization by electron impact with the distorted-wave and plane-wave Born approximations. *Physical Review A* **77**(4), 042701.

Bote, D., Salvat, F., Jablonski, A. & Powell, C. J. (2009). Cross sections for ionization of K, L and M shells of atoms by impact of electrons and positrons with energies up to 1 GeV: Analytical formulas. *Atomic data and nuclear data tables* **95**(6), 871-909.

Bourgeois, L., Muddle, B.C. & Nie, J.F. (2001). The crystal structure of the equilibrium Φ phase in Mg-Zn-Al casting alloys. *Acta Materialia* **49**(14), 2701-2711.

Bright, D. & Newbury, D. (1991). Concentration histogram imaging: A scatter diagram technique for viewing two or three related images. *Analytical chemistry* **63**(4), 243A-250A.

Browning, R., Li, T., Chui, B., Ye, J., Pease, R., Czyżewski, Z. & Joy, D.C. (1994). Empirical forms for the electron/atom elastic scattering cross sections from 0.1 to 30 keV. *Journal of Applied Physics* **76**(4), 2016-2022.

Brodusch, N., Demers, H. & Gauvin, R. (2017). *Field Emission Scanning Electron Microscopy: New Perspectives for Materials Characterization*. Springer.

Burgess, S., Li, X. & Holland, J. (2013). High spatial resolution energy dispersive X-ray spectrometry in the SEM and the detection of light elements including lithium. *Microscopy and Analysis* **6**, S8-S13.

Burgess, S., Holland, J., Statham, P. & McCarthy, C. (2016). Windowless EDS Detection of N Lines and their Practical use in sub 2 kV X-ray mapping to Optimize Spatial Resolution. *Microscopy and Microanalysis* **22***(S3)*, 112-113.

Burke, M., Watanabe, M., Williams, D. & Hyde, J. (2006). Quantitative characterization of nanoprecipitates in irradiated low-alloy steels: advances in the application of FEG-STEM quantitative microanalysis to real materials. *Journal of materials science* **41**(14), 4512-4522.

Campbell, J. (2003). Fluorescence yields and Coster-Kronig probabilities for the atomic L subshells. *Atomic data and nuclear data tables* **85**(2), 291-315.

Cardoso, J. F. (1998). Blind signal separation: statistical principles. *Proceedings of the IEEE* **86**(10), 2009-2025.

Casnati, E., Tartari, A. & Baraldi, C. (1982). An empirical approach to K-shell ionisation cross section by electrons. *Journal of Physics B: Atomic and Molecular Physics* **15**(1), 155-167.

Castaing, R. (1951). Application of Electron Probes to Local Chemical and Crystallographic Analysis. (Ph.D), University of Paris, California Institute of Technology, Pasadena, California, USA.

Chantler, C.T. (1995). Theoretical form factor, attenuation, and scattering tabulation for Z= 1-92 from E = 1-10 eV to E = 0.4-1.0 MeV. *Journal of Physical and Chemical Reference Data* **24**(1), 71-643.

Chantler, C.T. (2000). Detailed tabulation of atomic form factors, photoelectric absorption and scattering cross section, and mass attenuation coefficients in the vicinity of absorption edges in the soft X-ray (Z= 30-36, Z= 60-89, E= 0.1 keV -10 keV), addressing convergence issues of earlier work. *Journal of Physical and Chemical Reference Data* **29**(4), 597-1056.

Chen, M. H., Crasemann, B. & Mark, H. (1981). Widths and fluorescence yields of atomic L-shell vacancy states. *Physical Review A* **24**(1), 177.

Chen, M. H. & Crasemann, B. (1984). M x-ray emission rates in Dirac-Fock approximation. *Physical Review A* **30**(1), 170.

Cliff, G. & Lorimer, G. W. (1975). The quantitative analysis of thin specimens. *Journal of Microscopy* **103**(2), 203-207.

Çubukçu, H. E., Ersoy, O., Aydar, E. & Cakir, U. (2008). WDS versus silicon drift detector EDS: a case report for the comparison of quantitative chemical analyses of natural silicate minerals. *Micron* **39**(2), 88-94.

Czyżewski, Z., MacCallum, D.O.N., Romig, A. & Joy, D.C. (1990). Calculations of Mott scattering cross section. *Journal of Applied Physics* **68**(7), 3066-3072.

de la Peña, F., Berger, M. H., Hochepied, J. F., Dynys, F., Stephan, O., & Walls, M. (2011). Mapping titanium and tin oxide phases using EELS: an application of independent component analysis. *Ultramicroscopy* **111**(2), 169-176.

de la Peña, F., Fauske, V. T., Burdet, P., Jokubauskas, P., Nord, M., Prestat, E., Sarahan, M., MacArthur, K. E., Johnstone, D. N., Taillon, J., Caron, J., Furnival, T., Eljarrat, A., Mazzucco, S., Migunov, V., Aarholt, T., Walls, M., Winkler, F., Martineau, B., Donval, G., Hoglund, E. R., Alxneit, I., Hjorth, I., Zagonel, L. F., Garmannslund, A., Gohlke, C., Iyengar, I. & Chang, H. (2017). hyperspy/hyperspy: HyperSpy 1.3.

Demers, H., Brodusch, N., Joy, D. C., Woo, P. & Gauvin, R. (2013). X-ray quantitative microanalysis with an annular silicon drift detector. *Microscopy and Microanalysis* **19**(S2), 364-365.

Drouin, D., Couture, A. R., Joly, D., Tastet, X., Aimez, V. & Gauvin, R. (2007). CASINO V2. 42—A Fast and Easy-to-use Modeling Tool for Scanning Electron Microscopy and Microanalysis Users. *Scanning* **29**(3), 92-101. The software is available at http://www.gel.usherbrooke.ca/casino/download.html.

Duncumb, P. & Reed, S. J. B. (1968). Quantitative Electron Probe Microanalysis. NBS Spec. Publ, 298, pp.133.

Duncumb, P., Barkshire, I. R., & Statham, P. J. (2001). Improved X-ray spectrum simulation for electron microprobe analysis. *Microscopy and Microanalysis, 7*(4), 341-355.

Feng, A. & Ma, Z. (2007). Enhanced mechanical properties of Mg-Al-Zn cast alloy via friction stir processing. *Scripta materialia* **56**(5), 397-400.

Ferron, C.J., Bulatovic, S.M. & Salter, R.S. (1991). Beneficiation of rare earth oxide minerals. *Materials Science Forum* **70**, 251-270. Trans Tech Publications.

Fiori, C., Myklebust, R., Heinrich, K. & Yakowitz, H. (1976). Prediction of continuum intensity in energy-dispersive X-ray microanalysis. *Analytical chemistry* **48**(1), 172-176.

Fiori, C., Leapman, R., Swyt, C. & Andrews, S. (1988). Quantitative X-ray mapping biological cryosections. *Ultramicroscopy* **24**(2-3), 237-249.

Fiorini, C., Kemmer, J., Lechner, P., Kromer, K., Rohde, M. & Schülein, T. (1997). A new detection system for X-ray microanalysis based on a silicon drift detector with Peltier cooling. *Review of Scientific Instruments* **68**(6), 2461-2465.

Friel, J. J. & Lyman, C. E. (2006). Tutorial review: X-ray mapping in electron-beam instruments. *Microscopy and Microanalysis* **12**(1), 2-25.

Gauvin, R. (2005). X-ray microanalysis of real materials using Monte Carlo simulations. *Surface and interface analysis* **37**(11), 875-886.

Gauvin, R., Lifshin, E., Demers, H., Horny, P. & Campbell, H. (2006). Win X-ray: A new Monte Carlo program that computes X-ray spectra obtained with a scanning electron microscope. *Microscopy and Microanalysis* **12**(1), 49-64.

Gauvin, R. (2007). A universal equation for the emission range of X rays from bulk specimens. *Microscopy and Microanalysis* **13**(5), 354-357.

Gauvin, R. & Michaud, P. (2009). MC X-ray, a new Monte Carlo program for quantitative X-ray microanalysis of real materials. *Microscopy and Microanalysis* **15**(S2), 488-489. The software is available at http://montecarlomodeling.mcgill.ca/software/mcxray/download.html.

Gauvin, R. (2012). What remains to be done to allow quantitative X-ray microanalysis performed with EDS to become a true characterization technique? *Microscopy and Microanalysis* **18**(5), 915-940.

Genga, A., Baglivi, F., Siciliano, M., Siciliano, T., Tepore, M., Micocci, G., . . . Aiello, D. (2012). SEM-EDS investigation on PM10 data collected in Central Italy: Principal component analysis and hierarchical cluster analysis. *Chemistry Central Journal* **6**(S2), S3.

Goldstein, J. I., & Williams, D. B. (1977). X-ray analysis in the TEM/STEM. *Scanning Electron Microsocpy* **1**, 651-662.

Goldstein, J. I., Newbury, D. E., Echlin, P., Joy, D. C., Fiori, C. & Lifshin, E. (1981). Scanning Electron Microscopy and X-Ray Microanalysis. A Text for Biologists, Materials Scientists, and Geologists: Plenum Publishing Corporation.

Goldstein, J. I., Newbury, D. E., Michael, J. R., Ritchie, N. W., Scott, J. H. J. & Joy, D. C. (2017). Scanning electron microscopy and X-ray microanalysis. Springer.

Gschneidner, K. A. (2011). "The rare earth crisis—the supply/demand situation for 2010-2015." *Material Matters* **6**(2).

Gryziński, M. (1965). Classical theory of atomic collisions. I. Theory of inelastic collisions. *Physical Review* **138**(2A), A336.

Henoc, J. & Maurice, F. (1976). Characteristics of a Monte Carlo program for microanalysis study of energy loss. In Use of Monte Carlo Calculations in Electron Probe Microanalysis and Scanning Electron Microscopy, Heinrich, K.F., Newbury, D.E. & Yakowitz, H. (Eds.), pp. 61-95. US Dept. of Commerce, National Bureau of Standards: for sale by the Supt. of Docs., US Govt. Print. Off..

Hodoroaba, V.D., Procop, M. & Rackwitz, V. (2013). Check and specification of the performance of EDS systems attached to the SEM by means of a new test material EDS-TM002 and an updated evaluation software package EDS spectrometer test-version 3.4. *Microscopy and Microanalysis* **19**(S2), 1256-1257.

Horny, P. (2006). Development of a quantification method for x-ray microanalysis with an electron microscope. (Doctor of Philosophy), McGill University.

Horny, P., Lifshin, E., Campbell, H. & Gauvin, R. (2010). Development of a new quantitative X-ray microanalysis method for electron microscopy. *Microscopy and Microanalysis* **16**(6), 821-830.

Hovington, P., Drouin, D. & Gauvin, R. (1997). CASINO: A new Monte Carlo code in C language for electron beam interaction—Part I: Description of the program. *Scanning* **19**(1), 1-14.

Hovington, P., Timoshevskii, V., Burgess, S., Demers, H., Statham, P., Gauvin, R., & Zaghib, K. (2016). Can we detect Li KX-ray in lithium compounds using energy dispersive spectroscopy? *Scanning* **38**(6), 571-578.

Hyvärinen, A. & Oja, E. (2000). Independent component analysis: algorithms and applications. *Neural Networks* **13**(4), 411-430.

Jany, B. R., Janas, A. & Krok, F. (2017). Retrieving the Quantitative Chemical Information at Nanoscale from Scanning Electron Microscope Energy Dispersive X-ray Measurements by Machine Learning. *Nano letters* **17**(11), 6520-6525.

Jordens, A., Cheng, Y.P. & Waters, K.E. (2013). A review of the beneficiation of rare earth element bearing minerals. *Minerals Engineering* **41**(0), 97-114.

Jordens, A., Marion, C., Langlois, R., Grammatikopoulos, T., Rowson, N. A. & Waters, K. E. (2016). Beneficiation of the Nechalacho rare earth deposit. Part 1: Gravity and magnetic separation. *Minerals Engineering* **99**, 111-122.

Jordens, A., Marion, C., Langlois, R., Grammatikopoulos, T., Sheridan, R.S., Teng, C., Demers, H., Gauvin, R., Rowson, N.A. & Waters, K.E. (2016). Beneficiation of the Nechalacho rare earth deposit. Part 2: Characterisation of products from gravity and magnetic separation. *Minerals Engineering* **99**, 96-110.

Joy, D.C. & Luo, S. (1989). An empirical stopping power relationship for low-energy electrons. *Scanning* **11**(4), 176-180.

Joy, D. C. (2001). Fundamental constants for quantitative X-ray microanalysis. *Microscopy and Microanalysis* **7**(2), 159-167.

Kanter, H. (1961). Energy dissipation and secondary electron emission in solids. *Physical Review* **121**(3), 677.

Kirkpatrick, P. & Wiedmann, L. (1945). Theoretical continuous X-ray energy and polarization. *Physical Review* **67**(11-12), 321-339.

Knoll, G. F. (2010). *Radiation detection and measurement*. New York: John Wiley & Sons, Inc. pp. 119-122.

Kohl, H. & Reimer, L. (2008). Transmission electron microscopy: physics of image formation: Springer.

Kotula, P. G., Keenan, M. R. & Michael, J. R. (2003). Automated analysis of SEM X-ray spectral images: A powerful new microanalysis tool. *Microscopy and Microanalysis* **9**(1), 1-17.

Kotula, P. G., Keenan, M. R. & Michael, J. R. (2006). Tomographic spectral imaging with multivariate statistical analysis: comprehensive 3D microanalysis. *Microscopy and Microanalysis* **12**(1), 36-48.

Kotula, P. G., Michael, J. R. & Rohde, M. (2008). Results from two four-channel Si-drift detectors on an SEM: Conventional and annular geometries. *Microscopy and Microanalysis* **14**(S2), 116-117.

Kotula, P. G., Klenov, D. O. & von Harrach, H. S. (2012). Challenges to quantitative multivariate statistical analysis of atomic-resolution X-ray spectral. *Microscopy and Microanalysis* **18**(4), 691-698.

Krause, M.O. (1979). Atomic radiative and radiationless yields for K and L shells. *Journal of physical and chemical reference data* **8**(2), 307-327.

Lee, D. D. & Seung, H. S. (1999). Learning the parts of objects by non-negative matrix factorization. *Nature* **401**(6755), 788-791.

Lifshin, E., Ciccarelli, M. & Bolon, R. (1975). X-Ray spectral measurement and interpretation *Practical Scanning Electron Microscopy*, pp. 263-297: Springer.

Malinowski, E. R. (2002). Factor analysis in chemistry: Wiley.

Merlet, C. (1994). An accurate computer correction program for quantitative electron probe microanalysis. *Microchimica Acta* **114**(1), 363-376.

Montagné, P. & Tillard, M. (2016). On the adaptability of 1/1 cubic approximant structure in the Mg-Al-Zn system with the particular example of $Mg_{32}Al_{12}Zn_{37}$. *Journal of Alloys and Compounds* **656**, 159-165.

Murata, K., Matsukawa, T. & Shimizu, R. (1971). Monte Carlo calculations on electron scattering in a solid target. *Japanese Journal of Applied Physics* **10**(6), 678-686.

Myklebust, R. L., Fiori, C. & Heinrich, K. F. (1979). FRAME C: a compact procedure for quantitative energy-dispersive electron probe X-ray analysis. Final Report National Bureau of Standards, Washington, DC. National Measurement Lab.

Newbury, D. E., Swyt, C. R. & Myklebust, R. L. (1995). " Standardless" quantitative electron probe microanalysis with energy-dispersive X-ray spectrometry: is it worth the risk? *Analytical chemistry* **67**(11), 1866-1871.

Newbury, D.E. (2002). Barriers to quantitative electron probe X-ray microanalysis for low voltage scanning electron microscopy. *Journal of research of the National Institute of Standards and Technology* **107**(6), 605-619.

Newbury, D. E. (2005a). Misidentification of major constituents by automatic qualitative energy dispersive X-ray microanalysis: A problem that threatens the credibility of the analytical community. *Microscopy and Microanalysis* **11**(6), 545-561.

Newbury, D. E. (2005b). X-ray spectrometry and spectrum image mapping at output count rates above 100 kHz with a silicon drift detector on a scanning electron microscope. *Scanning* **27**(5), 227-239.

Newbury, D. E. (2006). Electron-excited energy dispersive X-ray spectrometry at high speed and at high resolution: silicon drift detectors and microcalorimeters. *Microscopy and Microanalysis* **12**(6), 527-537.

Newbury, D. E. (2007). Mistakes Encountered during Automatic Peak Identification in Low Beam Energy X-ray Microanalysis. *Scanning* **29**(4), 137-151.

Newbury, D. E. (2009). Mistakes encountered during automatic peak identification of minor and trace constituents in electron-excited energy dispersive X-ray microanalysis. *Scanning* **31**(3), 91-101.

Newbury, D. E. & Ritchie, N. W. (2013a). Elemental mapping of microstructures by scanning electron microscopy-energy dispersive X-ray spectrometry (SEM-EDS): extraordinary advances with the silicon drift detector (SDD). *Journal of Analytical Atomic Spectrometry* **28**(7), 973-988.

Newbury, D. E. & Ritchie, N. W. (2013b). Is scanning electron microscopy/energy dispersive X-ray spectrometry (SEM/EDS) quantitative? *Scanning* **35**(3), 141-168.

Newbury, D. E. & Ritchie, N. W. (2015). Performing elemental microanalysis with high accuracy and high precision by scanning electron microscopy/silicon drift detector energy-dispersive X-ray spectrometry (SEM/SDD-EDS). *Journal of materials science* **50**(2), 493-518.

Packwood, R. & Brown, J. (1981). A Gaussian expression to describe ϕ (ρz) curves for quantitative electron probe microanalysis. *X-Ray Spectrometry* **10**(3), 138-146.

Parish, C. M., Brennecka, G. L., Tuttle, B. A. & Brewer, L. N. (2008). Quantitative X-Ray Spectrum Imaging of Lead Lanthanum Zirconate Titanate PLZT Thin-Films. *Journal of the American Ceramic Society* **91**(11), 3690-3697.

Parish, C. M. & Brewer, L. N. (2010). Multivariate statistics applications in phase analysis of STEM-EDS spectrum images. *Ultramicroscopy* **110**(2), 134-143.

Parisini, A., Frabboni, S., Gazzadi, G. C., Rosa, R. & Armigliato, A. (2018). Comparison of Cliff-Lorimer-Based Methods of Scanning Transmission Electron Microscopy (STEM) Quantitative X-Ray Microanalysis for Application to Silicon Oxycarbides Thin Films. *Microscopy and Microanalysis* **24**(3), 193-206.

Pia, M. G., Saracco, P. & Sudhakar, M. (2009). Validation of K and L shell radiative transition probability calculations. *IEEE Transactions on Nuclear Science* **56**(6), 3650-3661.

Pirrie, D., Power, M. R., Rollinson, G. K., Wiltshire, P. E., Newberry, J. & Campbell, H. E. (2009). Automated SEM-EDS (QEMSCAN®) Mineral analysis in forensic soil investigations: Testing instrumental reproducibility. In *Criminal and Environmental Soil Forensics*, pp. 411-430, Dordrecht: Springer.

Pouchou, J. L. & Pichoir, F. (1984). A new model for quantitative X-ray microanalysis 1. Application to the analysis of homogeneous samples. *Recherche Aérospatiale* **3**, 167-192.

Powell, C. J. (1976). Cross sections for ionization of inner-shell electrons by electrons. *Reviews of modern physics* **48**(1), 33-47.

Powell, C. J., Jablonski, A., Salvat, F. & Lee, A. Y. (2016). NIST electron elastic-scattering cross-section database, Version 4.0. Natl Std. Ref. Data Series (NIST NSRDS)-64.

Puri, S., Mehta, D., Chand, B., Singh, N., & Trehan, P. N. (1993). L shell fluorescence yields and coster-kronig transition probabilities for the elements with 25⩽ Z⩽ 96. *X-Ray Spectrometry* **22**(5), 358-361.

Rahman, R. M., Ata, S. & Jameson, G.J. (2012). The effect of flotation variables on the recovery of different particle size fractions in the froth and the pulp. *International Journal of Mineral Processing* **106**, 70-77.

Reed, S. (1965). Characteristic fluorescence corrections in electron-probe microanalysis. *British Journal of Applied Physics* **16**(7), 913-926.

Reed, S. & Ware, N. (1973). Quantitative electron microprobe analysis using a lithium drifted silicon detector. *X-Ray Spectrometry* **2**(2), 69-74.

Reed, S. (1997). Electron microprobe analysis. Electron Microprobe Analysis: Cambridge University Press.

Ritchie N. W. (2009). Spectrum simulation in DTSA-II. *Microscopy and Microanalysis* **15**(5), 454-468.

Ritchie, N.W. (2011a). Getting started with NIST DTSA-II. *Microscopy Today* **19**(01), 26-31. The software is available at https://cstl.nist.gov/div837/837.02/epq/dtsa2/index.html.

Ritchie, N. W. (2011b). Standards-based quantification in DTSA-II—Part I. *Microscopy Today* **19**(5), 30-36.

Ritchie, N. W. (2012). Standards-based quantification in DTSA-II—Part II. *Microscopy Today,* **20**(1), 24-28.

Ritchie, N. W., Newbury, D. E. & Davis, J. M. (2012). EDS measurements of X-ray intensity at WDS precision and accuracy using a silicon drift detector. *Microscopy and Microanalysis* **18**(4), 892-904.

Ritchie N. W. (2017). Efficient simulation of secondary fluorescence via NIST DTSA-II Monte Carlo. *Microscopy and Microanalysis* **23**(3), 618-633.

Rossouw, D., Burdet, P., de la Pena, F., Ducati, C., Knappett, B. R., Wheatley, A. E. & Midgley, P. A. (2015a). Overcoming traditional challenges in nano-scale X-ray characterization using independent component analysis. *Microscopy and Microanalysis* **21**(S3), 1227-1228.

Rossouw, D., Burdet, P., de la Peña, F., Ducati, C., Knappett, B. R., Wheatley, A. E. & Midgley, P. A. (2015b). Multicomponent signal unmixing from nanoheterostructures: Overcoming the traditional challenges of nanoscale x-ray analysis via machine learning. *Nano letters* **15**(4), 2716-2720.

Rossouw, D., Knappett, B. R., Wheatley, A. E. & Midgley, P. A. (2016). A New Method for Determining the Composition of Core-Shell Nanoparticles via Dual-EDX+ EELS Spectrum Imaging. *Particle & Particle Systems Characterization* **33**(10), 749-755.

Saghi, Z., Einsle, J., Blukis, R., Strodahs, A., Leary, R., Burdet, P., Harrison, R. & Midgley, P. (2016). Improved data analysis and reconstruction methods for STEM-EDX tomography. *Microscopy and Microanalysis* **22**(S3), 284-285.

Salvat, F., Fernández-Varea, J. M. & Sempau, J. (2006). PENELOPE-2006: A code system for Monte Carlo simulation of electron and photon transport. Paper presented at the Workshop proceedings.

Schreiber, T. P. & Wims, A. M. (1982). Relative intensities of K and L shell X-ray lines. Microbeam Analysis, 161-166.

Scofield, J. H. (1974). Hartree-Fock values of L X-ray emission rates. *Physical Review A* **10**(5), 1507.

Seltzer SM & Berger MJ (1986). Bremsstrahlung energy spectra from electrons with kinetic energy 1 keV-10 GeV incident on screened nuclei and orbital electrons of neutral atoms with Z= 1-100. *Atomic data and nuclear data tables* **35**(3), 345-418.

Sheard, E.R., Williams-Jones, A.E., Heiligmann, M., Pederson, C. & Trueman, D.L. (2012). Controls on the concentration of zirconium, niobium, and the rare earth elements in the Thor Lake rare metal deposit, Northwest Territories, Canada. *Economic Geology* **107**(1), 81-104.

Sheridan, P. J. (1989). Determination of experimental and theoretical k_{ASi} factors for a 200-kV analytical electron microscope. *Journal of electron microscopy technique* **11**(1), 41-61.

Statham, P. J. (1984). Accuracy, reproducibility and scope for X-ray microanalysis with Si (Li) Detectors. *Le Journal de Physique Colloques* **45**(C2), 175-180.

Statham, P. J. (1998). Measuring performance of energy-dispersive X-ray systems. *Microscopy and Microanalysis* **4**(6), 605-615.

Statham, P. J. (2002). Limitations to accuracy in extracting characteristic line intensities from X-ray spectra. *Journal of research of the National Institute of Standards and Technology* **107**(6), 531.

Statham, P. & Holland, J. (2014). Prospects for higher spatial resolution quantitative X-ray analysis using transition element L-lines. In IOP Conference Series: *Materials Science and Engineering* **55**(1), 12-17.

Strüder, L., Fiorini, C., Gatti, E., Hartmann, R., Holl, P., Krause, N., . . . Kemmer, J. (1998). High resolution non dispersive X-ray spectroscopy with state of the art silicon *detectors Modern Developments and Applications in Microbeam Analysis* (pp. 11-19): Springer.

Teng, C., Demers, H., Brodusch, N., Waters, K., Jordens, A. & Gauvin, R. (2015). Characterization of rare earth minerals using X-ray phase map with high spatial resolution field-emission scanning electron microscope. Proceedings of *Conference of Metallurgist*.

Teng, C., Demers, H., Brodusch, N., Waters, K. & Gauvin, R. (2018). Use of an annular silicon drift detector (SDD) versus a conventional SDD makes phase mapping a practical solution for rare earth mineral characterization. *Microscopy and Microanalysis* **24**(3), 238-248.

Teng, C., Demers, H., Chu, X., & Gauvin, R. (2019). The f-ratio quantification method for X-ray microanalysis applied to Mg-Al-Zn alloys. *Microscopy and Microanalysis* **25**(1), 58-69.

Teng, C. & Gauvin, R. (2019a). Multivariate statistical analysis on an SEM/EDS phase map of rare earth minerals. *Scanning* (in press).

Teng, C. & Gauvin, R. (2019b). The f-ratio quantification method applied to standard minerals with a cold field emission SEM/EDS. *Talanta* **204**, 213-223.

Titchmarsh, J. M. (1998). X-Ray Spectrum Processing and Multivariate Analysis. In G. Love, W. A. P. Nicholson, & A. Armigliato (Eds.), Modern Developments and Applications in Microbeam Analysis, pp. 37-47: Springer.

Titchmarsh, J. (1999). EDX spectrum modelling and multivariate analysis of sub-nanometer segregation. *Micron* **30**(2), 159-171.

Trebbia, P. & Bonnet, N. (1990). EELS elemental mapping with unconventional methods I. Theoretical basis: Image analysis with multivariate statistics and entropy concepts. *Ultramicroscopy* **34**(3), 165-178.

Watanabe, M., Horita, Z. & Nemoto, M. (1996). Absorption correction and thickness determination using the ζ factor in quantitative X-ray microanalysis. *Ultramicroscopy* **65**(3-4), 187-198.

Watanabe, M. & Williams, D. (2006). The quantitative analysis of thin specimens: A review of progress from the Cliff-Lorimer to the new ζ-factor methods. *Journal of Microscopy* **221**(2), 89-109.

Wentzell, P. D., Andrews, D. T., Hamilton, D. C., Faber, K. & Kowalski, B. R. (1997). Maximum likelihood principal component analysis. *Journal of Chemometrics* **11**(4), 339-366.

Wielopolski, L. & Gardner, R. P. (1976). Prediction of the pulse-height spectral distortion caused by the peak pile-up effect. *Nuclear Instruments and Methods* **133**(2), 303-309.

Wills, B.A. & Finch, J. (2015). *Wills' mineral processing technology: an introduction to the practical aspects of ore treatment and mineral recovery*. Oxford: Butterworth-Heinemann. pp. 118-145.

Wold, S., Esbensen, K. & Geladi, P. (1987). Principal component analysis. Chemometrics and intelligent laboratory systems **2**(1-3), 37-52.

Wollman, D. A., Irwin, K. D., Hilton, G. C., Dulcie, L., Newbury, D. E. & Martinis, J. M. (1997). High-resolution, energy-dispersive microcalorimeter spectrometer for X-ray microanalysis. *Journal of Microscopy* **188**(3), 196-223.

Wood, J., Williams, D. & Goldstein, J. (1984). Experimental and theoretical determination of k_{AFe} factors for quantitative X-ray microanalysis in the analytical electron microscope. *Journal of Microscopy* **133**(3), 255-274.

Wu, Q., Merchant, F. & Castleman, K. (2010). Microscope image processing: Academic press.

Yakowitz, H. (1968). Evaluation of specimen preparation and the use of standards in electron probe microanalysis Fifty Years of Progress in Metallographic Techniques: ASTM International.

Zaluzec, N. (1984). K and L-shell cross-sections for X-ray microanalysis in an AEM. Paper presented at the Presented at the Microbeam Analysis Soc. Analytical Electron Microscopy Meeting, Bethelem, Pa.

Zaluzec, N. (2014). Analytical formulae for calculation of X-ray detector solid angles in the scanning and scanning/transmission analytical electron microscope. *Microscopy and Microanalysis* **20**(4), 1318-1326.

Zhang, J. & Edwards, C. (2013). Mineral decomposition and leaching processes for treating rare earth ore concentrates. *Canadian Metallurgical Quarterly* **52**(3), 243-248.

Zhang, X. D. (2017). Matrix analysis and applications: Cambridge University Press.